Optical noise and mesoscopic correlations in random media

Optical noise and mesoscopic correlations in random media

ACADEMISCH PROEFSCHRIFT

ter verkrijging van de graad van doctor
aan de Universiteit van Amsterdam
op gezag van de Rector Magnificus
prof. dr. D. C. van den Boom
ten overstaan van een door het college voor promoties
ingestelde commissie,
in het openbaar te verdedigen in de Agnietenkapel
op woensdag 2 November 2011, te 12.00 uur

door

Paolo Sebastiano Scalia

geboren te Rome, Italië

Promotiecommissie:

Promotor	Prof. Dr. A. Lagendijk
Co-promotor	Dr. O.L. Muskens
Overige leden	Prof. Dr. H.J. Bakker
	Prof. Dr. M.S. Golden
	Prof. Dr. W.L. Vos
	Prof. Dr. D.S. Wiersma

Faculteit der Natuurwetenschappen, Wiskunde en Informatica

The work described in this thesis is part of the research program of the "Stichting Fundamenteel Onderzoek der Materie (FOM)", which is financially supported by the "Nederlandse Organisatie voor Wetenschappelijk Onderzoek (NWO)".

This work was carried out at the
FOM Institute for Atomic and Molecular Physics
Science Park 104, 1098 XG, Amsterdam, The Netherlands,
where a limited number of copies of this thesis is available
ISBN: 978-90-77209-55-4

ai miei nonni

Paranimfen: Patrick M. Johnson en Bergin Gjonaj.

un tarí é troppu pocu

Parte di una filastrocca siciliana

Contents

CHAPTER 1

Introduction

In this introduction we outline the main features that characterize the transport of light and the origin and propagation of optical noise in random photonic media. Furthermore some general measurement methods are explained.

1.1 The noise is the signal [1]

Imagine the following situation: you have bought your favorite band's latest CD, you rush home to play it on your hi-tech stereo system, but the moment the music comes on you realize that there is something seriously wrong. Bzzz....Vsss...Frr. That is what comes out of your subwoofers, mixed with your favorite artist's voice. In other words noise is at work, and is disrupting your music.

Noise manifests itself by introducing random fluctuations on an otherwise stable and constant signal and is commonly seen as a problem that limits the capability of our systems, and the accuracy of our measurements. In the example above, noise restricts the performance of our sound system and prevents us from enjoying our music. As a more technical illustration, thermal noise, due to the random movements of atoms and molecules, can often mask a weak effect that we want to isolate and measure.

On the other hand, noise does not possess only detrimental properties. In fact, its features can be exploited to extract important information from the systems that

---

[1] quote attributed to Rolf Landauer [1]

are the object of our study, or even more: noise itself can turn out to be the source of a new physical phenomenon. For instance, thermal noise is at the base of the phenomenon known today as Brownian motion, named after the botanist Robert Brown who discovered it in 1828 [2].

The importance of noise analysis resides in the fact that often fluctuations can offer a wealth of information that is not directly obtainable from measurements that target average quantities. Furthermore these fluctuations are, in some cases, an order of magnitude bigger than the average values. These general properties have determined the success of techniques aimed at isolating and investigating the noise content of a given signal.

Noteworthy examples of the crucial role played by noise span across many fields of science. In biology for example, by exploiting non equilibrium fluctuations it is possible to bias Brownian motion in order to drive the action of micro motors [3, 4]. Noise has recently been recognized as the mechanism underlying the generation of rogue waves. Rogue waves are gigantic waves that can appear all of a sudden in the open sea and are believed to be the cause of many inexplicable accidents [5]. It has been shown, in optical experiments, how from a noisy background high intensity peaks may arise, providing a plausible explanation for the generation of rogue ocean waves and the means to tune and tame them [6–10]. In geophysics, seismic noise has been recognized as a novel and powerful tool. Important examples consist in obtaining precise information about the Earth's crust and helping predict volcanic eruptions [11–13]. In photonics, laser noise has been identified as a very efficient random number generator, important in the production of security codes [14–18]. The properties of noise have been extensively taken advantage of in studying disordered electronic systems [19, 20]. The propagation of noise through electronic systems has also been used to investigate interesting properties of graphene, a new and very promising material both for fundamental studies and applications [21].

Noise mechanisms can be external but also intrinsic to the system being studied. The motion of the micro motors from the example above can be driven by imposing external fluctuations on the system. By contrast, the quantum intensity fluctuations present in a laser beam are inherent to laser light. These fluctuations are evidence of the discrete nature of photons and are the root cause of the the phenomenon known as photon shot noise. Photon shot noise marks the transition from the classical world into the the quantum one and cannot be eliminated. The classical world is ruled by fluctuations whose intensity is higher than the level determined by shot noise. Classical fluctuations above the shot noise limit can be reduced. When we achieve sub-shot noise[2] fluctuations we make the transition into the quantum world, governed by the laws of quantum optics.

Quantum optics, whose theoretical foundations were laid by Roy Glauber [23], has played a pivotal role in developing methods to reduce noise in light beams in order to demonstrate the quantum nature of light. These efforts have culminated in the generation of non classical states like squeezed and Fock states [24–29]. Among

---

[2] Sub-shot noise fluctuations can be achieved by using advanced quantum optics methods. That does not mean that we have eliminated shot noise. By reducing the noise of one observable below the shot noise level, we inevitably increase the noise of another observable of the system [22].

the technological applications, noteworthy is the use of squeezed light to improve the sensitivity of gravitational wave detectors [30–32]. A complete overview of the many facets of optical noise in photonics is given in [33].

The physical systems of interest to us here are multiple scattering media. One of the main characteristics of these systems consists in the fact that light is scattered many ($\sim 10^3$) times before it is allowed to leave the medium. By increasing the scattering strength the light-matter interaction in these media can be maximized. Our goal is to investigate the propagation of optical noise through strongly scattering media to extract information about the modalities of light transport and the properties of our systems. Optical noise is determined by the intensity fluctuations of an optical signal. In experiments, the optical signal is in many cases the light emitted from laser systems, whose noise properties are crucial to correctly interpret the results. In the following sections, we give an overview of a selection of techniques widely used in the investigation of random media with light, and introduce in more detail the concept of noise for laser systems.

1.2 Important concepts in the physics of propagation of light in disordered media

1.2.1 Mesoscopic optics

Our investigations take place in the realm of mesoscopic physics, and in the following we will introduce some general definitions and length scales. The key parameter useful to establish distinctions among transport of light on different length scales is the mean free path ℓ, that is the mean distance between two consecutive scattering events. Macroscopic optics describes propagation of light on length scales much larger than ℓ. Microscopic optics deals with transport of light on length scales much smaller than the mean free path and it is required a detailed knowledge of the position and shapes of the scatterers. The prefix 'meso' in the word mesoscopic means intermediate. Mesoscopics describes physics at a length scale intermediate between the microscopic and the macroscopic length scales. Important mathematical inequalities in mesoscopic optics that relate relevant length scales to each other are the following

$$\ell \gg L \gg \lambda, \tag{1.1}$$

$$\lambda \ll \ell \ll L, \tag{1.2}$$

$$\lambda \sim \ell \ll L, \tag{1.3}$$

where λ denotes the wavelength of light and L the sample size. These three inequalities describe different transport regimes. Eq. (1.1) identifies the situation in which light does not undergo any scattering event and the interaction between light and the system is minimal. Eq. (1.2) defines the diffusion regime, it implies that light undergoes many scattering events before it escapes the medium. The last inequality, eq. (1.3), describes the localization regime, a type of transport whereby due to strong scattering and interference effects light is trapped inside the sample for a long time before it is allowed to exit the system [34, 35].

1.2.2 Random walk for light

Propagation of light in a random medium can be modelled by means of random walk theory. It is found that random walk is at the heart of the diffusion model. In this sense we can think of the transport of light in a random medium as a diffusion process. In optics, an example of a diffusion process corresponds to placing a localized source in a random medium and investigating the transport of its intensity. In one dimension we have that the diffusion equation for the probability density $p(x,t)$ is given by

$$\frac{\partial p(x,t)}{\partial t} = D\frac{\partial^2 p(x,t)}{\partial x^2}, \tag{1.4}$$

with initial condition

$$p(x,t=0) = \delta(x), \tag{1.5}$$

where D is the diffusion coefficient and x is the spatial variable. Eq. (1.4) is the diffusion equation. The diffusion equation is widely used in physics and describes an ample class of phenomena, such as heat transport. In our case we assume that light undergoes a diffusion process in our random material and our initial condition, eq. (1.5), corresponds to requesting a source of light localized at $x = 0$ at $t = 0$. The solution to the one dimensional diffusion equation is given by

$$p(x,t) = \frac{1}{\sqrt{4\pi Dt}} \exp\left(-\frac{x^2}{4Dt}\right), \tag{1.6}$$

whereas the solution in s dimensions is

$$p(\mathbf{x},t) = \frac{1}{(4\pi Dt)^{\frac{s}{2}}} \exp\left(-\frac{r^2}{4Dt}\right), \tag{1.7}$$

where $r = |\mathbf{x}|$. We are interested in calculating the mean square displacement $\overline{r^2}$, where the overbar denotes averaging on the distribution. The calculation yields

$$\overline{r^2} = 2sDt. \tag{1.8}$$

In multiple scattering theory the diffusion coefficient can be identified with $D = \frac{1}{s}v\ell$, where v is the transport speed of light [36]. Furthermore we can also write $v = \frac{N\ell}{t}$ where N is the number of diffusion steps. Substituting in eq. (1.8) we obtain

$$\overline{r^2} = 2N\ell^2. \tag{1.9}$$

The total mean square displacement is related to the distance d between the first and last steps taken by the random walker

$$d \equiv \sqrt{\overline{r^2}} = \sqrt{2N}\ell. \tag{1.10}$$

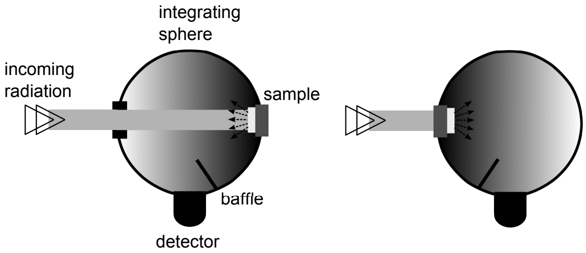

Figure 1.1: The integrating sphere in a reflection (left), and transmission (right) configuration spatially integrates the light transmitted or reflected by the sample prior to detection. The baffle protects the detector from light specularly reflected from the sample.

1.2.3 Total transmission and reflection

One of the classical and most widely used methods to characterize the transport of light in complex optical media consists in performing total transmission and total reflection measurements. The key instrument to these techniques is the integrating sphere. An integrating sphere is used to maximize the collection of light exiting the sample, in transmission or reflection, and measures the intensity of the light integrated over the solid angle. The main sample parameter obtainable is the mean free path ℓ. Optical measurements that make use of integrating spheres correspond in electronics to conductance measurements. The main components of a total reflection or transmission setup are presented in fig. (1.1). In electronics it is only feasible to perform measurements that spatially integrate the electron charge. By contrast, in optics angle resolved measurements are possible and widely used to characterize and investigate the transport of light in the medium. This is possible thanks to the phenomenon of speckle that will be illustrated in the next section.

1.2.4 Speckle and coherence area

The speckle pattern is a granular distribution of light that can be observed on a screen upon shining coherent light on a disordered medium, both in a reflection or transmission configuration. The speckle pattern manifest itself as random series of alternating bright and dark spots that demonstrate the occurrence of constructive and destructive interference phenomena surviving the scattering events, as illustrated in fig. (1.2). The interference takes place among the scattering light paths, once they emerge from the medium. By contrast, shining incoherent light on the disordered medium would wash out the all interference phenomena and the speckle pattern.

Related to the concept of speckle is the one of coherence area. The coherence area is the area over which coherence is retained. In practical terms, given a speckle pattern, its coherence area can be obtained by performing an autocorrelation of the intensity distribution. One of the main points regarding a speckle pattern is its high intensity fluctuations. To show this we calculate the relative fluctuations of a speckle pattern. We write the total field E_{tot} as a superposition of all the fields

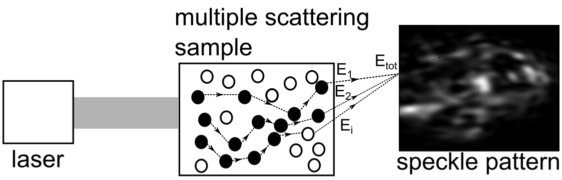

Figure 1.2: A speckle pattern results as coherent light propagating along scattering paths interferes on an observing screen. The fluctuating nature of the speckle pattern, that displays a series of dark and bright spots, is due to the random phase difference accumulated as light proceeds along the paths.

propagating through the medium

$$E_{tot} = \sum_i E_0 \exp(i\phi_i), \tag{1.11}$$

where ϕ_i is the phase of the $i - th$ field accumulated on propagation along the $i - th$ scattering path. For simplicity we assume here that each field has the same amplitude E_0 . The total intensity I_{tot} is given by

$$I_{tot} = E_{tot}E_{tot}^{\star} = |E_0|^2 \sum_{i,j} \exp i(\phi_i - \phi_j). \tag{1.12}$$

Furthermore we have

$$I_{tot}^2 = |E_0|^4 \sum_{i,j,k,l} \exp i(\phi_i - \phi_j + \phi_k - \phi_l). \tag{1.13}$$

Now we can calculate the relative fluctuations of a speckle pattern

$$\frac{\overline{I_{tot}^2} - \overline{I_{tot}}^2}{\overline{I_{tot}}^2} = \frac{\left(2\overline{|E_0|}^4 - \overline{|E_0|}^4\right)N^2}{\overline{|E_0|}^4 N^2} = 1, \tag{1.14}$$

where the overbars denote ensemble averaging and N the total number of fields. We have exploited the fact that the phases are random variables; therefore in eq. (1.13) when calculating the ensemble averages the only values that yields values different from zero are the ones in correspondence of which $\phi_i = \phi_j$ and $\phi_k = \phi_l$ or $\phi_i = \phi_l$ and $\phi_j = \phi_k$. It is shown that the fluctuations of a speckle intensity pattern are of order one.

1.2.5 Scattering theory in a waveguide

The use of the scattering theory applied to a waveguide geometry is widely used in mesoscopic physics, and it will be employed mainly in chapter 2 and chapter 4 of this thesis. One of the main reasons of its success is the fact that, due to the boundary conditions, the number of propagating modes is quantized and well defined. These modes are also called channels.

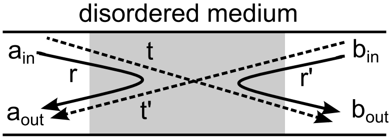

Figure 1.3: Simple schematics of the waveguide model. The scattering matrix M is composed of the sub-matrices r, t, r', t'. The matrix r (t) describes reflection (transmission) from modes a_{in} to a_{out} (b_{out}). The matrix r' (t') reflection (transmission) from modes b_{in} to modes b_{out} (a_{out}).

In this section we will give the general fundamentals. The scattering system is characterized by its scattering matrix M. The waveguide structure allows for the establishment of a basis for the matrix M, so that the fields interacting with the system can be described in terms of their modes. The scattering matrix is a $2N \times 2N$ matrix, where N is the number of modes supported by the system, defined as

$$\left(\begin{array}{c} E_{a_{out}} \\ E_{b_{out}} \end{array} \right) = M \left(\begin{array}{c} E_{a_{in}} \\ E_{b_{in}} \end{array} \right), \tag{1.15}$$

The E's are vector matrices of length N that describe the amplitude of the modes a and b. In a waveguide geometry N is determined by the transversal dimensions and by the wavelength of the incoming beam. The scattering matrix relates the field in the incoming modes to the field in the outgoing modes, and describes the effect of the system. The scattering matrix M can be further specified as

$$M = \left(\begin{array}{cc} r & t' \\ t & r' \end{array} \right), \tag{1.16}$$

with r, t, t', r' $N \times N$ matrices that describe reflection and transmission of the incoming fields. Energy conservation imposes that in passive systems with no gain or absorption M is unitary $\left(M^\dagger M = MM^\dagger = \mathbf{1}\right)$. Furthermore, if the physical system supports time reversal M is also symmetric $\left(M = M^T\right)$. This waveguide model is illustrated in fig. (1.3). More explicitly we can write

$$\begin{array}{rl} E_{a_{out}} = & rE_{a_{in}} + t'E_{b_{in}} \\ E_{b_{out}} = & tE_{a_{in}} + r'E_{b_{in}} \end{array}, \tag{1.17}$$

where the role of the sub-matrices of M becomes more apparent. Eqs. (1.17) can be further simplified depending on the problem at hand. If, for instance the system under investigation is very thick, $\left(\frac{L}{\ell} \gg 1\right)$, then we could neglect contributions from t and t'. Random matrix theory (RMT) deals with the probability distribution of the matrix entries, decided according to a certain set of assumptions, and extracts the values and correlations among the eigenvalues and eigenvectors, from which the properties of the systems are inferred [37].

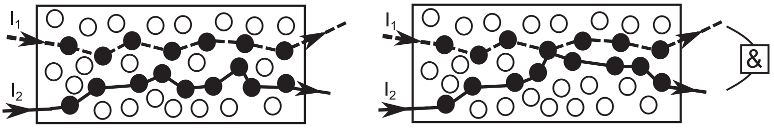

Figure 1.4: Difference between correlated and uncorrelated scattering paths. Two intensities I_1 (dashed line) and I_2(solid line) propagate through a multiple scattering medium. The stricken scatterers are depicted with black circles. (left) Independent scattering paths give rise to uncorrelated transmitted intensities. Negative exponential statistics applies. (right) Intersecting scattering paths give rise to correlated transmitted intensities and to a deviation from negative exponential statistics.

1.2.6 Speckle statistics

Speckles have a well determined and robust statistical representation given by a negative exponential distribution. This is a consequence of the central limit theorem in the sense that the total field, depicted as E_{tot} in fig. (1.2), acquires a Gaussian distribution. This holds true because each field and phase component are independent from one another and from all the other fields and phase elements [38]. It can be shown that from a Gaussian distribution for the field descends a negative exponential distribution for the intensity [39].

The negative exponential distribution to which the intensity speckle pattern obeys can be used to infer the feature of light transport in the medium. In other words negative exponential speckle statistics is a consequence of the independent light paths along which the incoming light propagates. Therefore, if the propagating paths in the medium are not independent from each other but intersect multiple times the central limit theorem does not hold any longer, and deviations from negative exponential statistics are observed. The parameter that is commonly used to quantify this deviation is called the universal conductance, indicated with g, defined as [40]

$$g \equiv \sum_{a,b} \overline{T}_{ab}. \tag{1.18}$$

where T_{ab} is the transmission coefficient from channel a to channel b and the overline denotes ensemble averaging. The relevant parameter used to quantify interference between paths is g^{-1}. A comparison between correlated and uncorrelated intensities is depicted in fig. (1.4). More specifically, it can be shown that to account for the possibility for interference between paths in the medium the exponential probability distribution has to be modified according to the formula by Nieuwenhuizen and Van Rossum [41]

$$P\left(\frac{I}{\overline{I}}\right) = \exp\left(-\frac{I}{\overline{I}}\right)\left\{1 + \frac{1}{3g}\left[\left(\frac{I}{\overline{I}}\right)^2 - 4\left(\frac{I}{\overline{I}}\right) + 2\right]\right\}. \tag{1.19}$$

A similar formula was also derived by Shnerb and Kaveh [42]. The role of the parameter g is of great importance as it is thought to signal the proximity of the

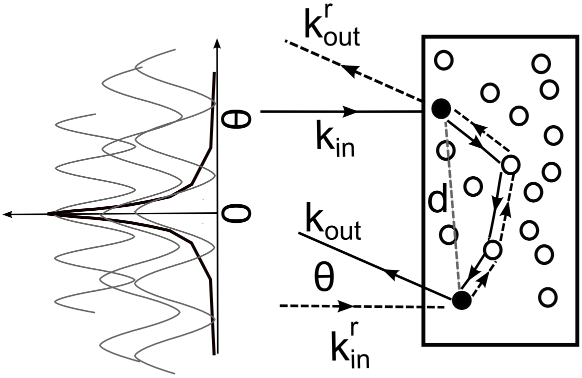

Figure 1.5: Principle of the coherent backscattering cone. The oscillating curves (solid lines in grey) depict interference patterns for a fixed distance d between the first and the last scatterer (full circles). The interference between the light propagating along the direct (solid lines) and reverse paths (dashed lines) is always fully constructive in the backscattering direction ($\theta = 0$). Away from the backscattering direction dephasing occurs and the interference contribution decreases. Summing over all possible interference contributions gives rise to the coherent backscattering cone (solid curve in black). With k_{in} and k_{out} we refer to the incoming and outgoing light. With k^r_{in} and k^r_{out} we refer to the incoming and outgoing light that propagates along the reverse paths.

Anderson (or strong) localization. Localization occurs for $g = 1$. The study of g is also of importance in the transport of light through absorbing and amplifying random media [43], [44].

1.2.7 Coherent backscattering cone

The coherent backscattering cone is a demonstration that interference phenomena can survive averaging over disorder. The basic idea is illustrated in the following. Let us imagine to shine coherent light on to a multiple scattering object, which is not completely opaque, and observe the transmitted output onto a screen: we would see a granular pattern, the speckle pattern. A speckle pattern would appear also in a reflection configuration. We refer here to the light that has diffused through the medium and, after a certain number of scattering events, emerges from the random medium on the side of the incident light.

Let us analyze in more detail what happens in a reflection configuration If we changed the configuration of the scatterers and perform the experiment again we would see a different pattern. Each new configuration for the scatterers would lead to a new speckle pattern. We can speculate over what happens when the speckle pattern is averaged over many different configurations. This type of averaging is called ensemble average or average over disorder. Naively, one may expect all the different interference contributions to be averaged out. Only a flat intensity profile would be left. This is not the case as there is one interference effect that survives the ensemble averaging: that is the interference between the direct and the reverse paths. Along the reverse paths light propagates following exactly the same trajectory as for the direct paths but in the opposite direction. These two paths have exactly the same length inside the medium and interfere fully constructively in the backscattering direction. Summing over all paths gives rise to the coherent backscattering cone. The cone profile shows a maximum enhancement of two along the backscattering direction with respect to the diffuse background. The enhancement then gradually decreases as we move away from the tip of the cone, along its wings. We can think of the interference between the direct and the reverse paths as a Young's double slit experiment with the two slits being represented in this case by the two scatterers positioned at the beginning and at the end of the paths. Let us consider the two scatterers to be placed along the same vertical line, their distance being d, the produced interference pattern is given by

$$I = E_0^2 \left[1 + \cos(kd \sin\theta)\right], \tag{1.20}$$

with k being the module of the wavevector relative to the incoming light field, θ the angle measured from the perpendicular to the sample surface, and E_0 the module of the incoming field. The interference pattern assumes maxima for $kd \sin\theta = 0$ and is always fully constructive in the backscattering direction, where $\theta = 0$. An important feature of the cone is that the wings carry information about the low order scattering events while its tip is the result of high order scattering events. To see this we have to use the results from subsection 1.2.6. As light follows a random walk in the material we can write, by using eq. (1.10), that $d = \sqrt{2N}\ell$. As N gets bigger d gets larger. As d increases the fringe of the interference pattern become increasingly closely spaced and sharp, with the sharpest interference fringes corresponding to the longest paths, and contributing to the cusped shape of the tip of the cone. For each d we always have constructive interference in the backscattering direction. Therefore in the backscattering direction we have contributions from all path lengths. As we move away from the backscattering direction some dephasing occurs, due to the building up of path difference between the direct and reversed paths, decreasing the interference contrast. It is remarkable that interference effects survive ensemble averaging.

Another key feature to the cone is the fact that its FWHM (full width half maximum) is inversely proportional to $k\ell^{-1}$. The coherent backscattering cone has been measured for the first time in 1984, the obtained enhancement then was very low and the explanation given for the measurements was not correct [45]. In 1985 in two seminal papers two groups showed clear cones with high enhancement and gave the correct interpretation for the phenomenon [46, 47]. The theory for the coherent backscattering cone was mainly developed in [48, 49].

We now proceed highlighting the impact of constructive interference in the coherent backscattering cone theory, following [50]. Let us consider the situation shown in figure (1.5). A wave impinges on a semi-infinite slab with wave vector $\mathbf{k}_{in}$ and exits the medium with wavevector $\mathbf{k}_{out}$. The light undergoes multiple scattering inside the medium. The first scattering event takes place at $\mathbf{r}_{fs}$ while the last one at $\mathbf{r}_{ls}$. The outgoing field amplitude $A\left(\mathbf{k}_{in},\mathbf{k}_{out}\right)$ is given by

$$A\left(\mathbf{k}_{in},\mathbf{k}_{out}\right)=\sum_{r_{fs}r_{ls}} f\left(\mathbf{r}_{f},\mathbf{r}_{l}\right)\exp\left[i\left(\mathbf{k}_{in}\cdot\mathbf{r}_{f}-\mathbf{k}_{out}\cdot\mathbf{r}_{l}\right)\right], \tag{1.21}$$

with $f\left(\mathbf{r}_{f},\mathbf{r}_{l}\right)$ being the amplitude of the wave propagating from $\mathbf{r}_{fs}$ to $\mathbf{r}_{ls}$. The intensity is the interesting observable and to calculate it we have to compute $\left|A\left(\mathbf{k}_{in},\mathbf{k}_{out}\right)\right|^{2}=A\left(\mathbf{k}_{in},\mathbf{k}_{out}\right)^{\star}A\left(\mathbf{k}_{in},\mathbf{k}_{out}\right)$. We obtain

$$\left|A\left(\mathbf{k}_{in},\mathbf{k}_{out}\right)\right|^{2}=\sum_{r_{f},r_{l}}\sum_{r_{f1},r_{l_1}} H\exp i\left[\mathbf{k}_{in}\cdot\left(\mathbf{r}_{f}-\mathbf{r}_{f_1}\right)+\mathbf{k}_{out}\left(\mathbf{r}_{l}-\mathbf{r}_{l_1}\right)\right], \tag{1.22}$$

with $H=f\left(\mathbf{r}_{f},\mathbf{r}_{l}\right)f\left(\mathbf{r}_{f_1},\mathbf{r}_{l_1}\right)^{\star}$. Let us focus our attention on the product $f\left(\mathbf{r}_{f},\mathbf{r}_{l}\right)f\left(\mathbf{r}_{f_1},\mathbf{r}_{l_1}\right)^{\star}$. We can write

$$f\left(\mathbf{r}_{f},\mathbf{r}_{l}\right)=\sum_{m}a_{m}(\mathbf{r}_{f},\mathbf{r}_{l})=\sum_{m}\left|a_{m}\right|\exp\left(i\delta_{m}\right), \tag{1.23}$$

with δ_m being the phase accumulated along the path m. We can then write

$$f\left(\mathbf{r}_{f},\mathbf{r}_{l}\right)f\left(\mathbf{r}_{f_1},\mathbf{r}_{l_1}\right)^{\star}=\sum_{m,n}\left|a_{m}\left(\mathbf{r}_{f},\mathbf{r}_{l}\right)\right|\left|a_{n}\left(\mathbf{r}_{f_1},\mathbf{r}_{l_1}\right)\right|\exp i\left(\delta_{m}-\delta_{n}\right), \tag{1.24}$$

and therefore eq. (1.22) becomes

$$\left|A\left(\mathbf{k}_{in},\mathbf{k}_{out}\right)\right|^{2}=\sum_{r_{f}r_{l}}\sum_{r_{f_1}r_{l_1}}\sum_{m,n}O\exp i\left[\mathbf{k}_{in}\cdot\left(\mathbf{r}_{f}-\mathbf{r}_{f_1}\right)+\mathbf{k}_{out}\left(\mathbf{r}_{l_1}-\mathbf{r}_{l}\right)\right], \tag{1.25}$$

with

$$O=\left|a_{m}\left(\mathbf{r}_{f},\mathbf{r}_{l}\right)\right|\left|a_{n}\left(\mathbf{r}_{f_1},\mathbf{r}_{l_1}\right)\right|\exp i\left(\delta_{m}-\delta_{n}\right). \tag{1.26}$$

The next step we take is calculating $\overline{\left|A\left(\mathbf{k}_{in},\mathbf{k}_{out}\right)\right|^{2}}$, that is the average of the intensity on the disorder; this type of averaging is called ensemble averaging. The quantity $\left(\delta_m-\delta_n\right)$ is the difference between two multiple scattering paths and is a fluctuating random variable, therefore in general $\overline{\exp i\left(\delta_m-\delta_n\right)}=0$. The only exception occurs when $\delta_m-\delta_n=0$. This situation manifests itself in two cases

1. The two amplitudes step through the very same path and also the direction of propagation is the same
2. The two amplitudes step through the very same path but the direction of propagation is not the same: they propagate along opposite directions.

In case (1) $\mathbf{r}_f=\mathbf{r}_{f_1}$ and $\mathbf{r}_l=\mathbf{r}_{l_1}$ while in case (2) $\mathbf{r}_f=\mathbf{r}_{l_1}$ and $\mathbf{r}_{f_1}=\mathbf{r}_l$. Therefore for case (1) we have

$$\overline{\left|A\left(\mathbf{k}_{in},\mathbf{k}_{out}\right)\right|_{1}^{2}}=\sum_{r_{f},r_{l}}\overline{\sum_{m}\left|a_{m}\left(\mathbf{r}_{f},\mathbf{r}_{l}\right)\right|^{2}}, \tag{1.27}$$

and in case (2)

$$\overline{|A(\mathbf{k}_{in}, \mathbf{k}_{out})|_2^2} = \sum_{r_f, r_l} \sum_m \overline{|a_m(\mathbf{r}_f, \mathbf{r}_l)|^2} \exp\left[(\mathbf{k}_{in} + \mathbf{k}_{out})(\mathbf{r}_f - \mathbf{r}_l)\right]. \qquad (1.28)$$

Adding up the two contributions we have

$$\overline{|A(\mathbf{k}_{in}, \mathbf{k}_{out})|^2} = \sum_{r_f r_l} \overline{f(\mathbf{r}_f, \mathbf{r}_l)^2} \left(1 + \exp\left[(\mathbf{k}_{in} + \mathbf{k}_{out})(\mathbf{r}_f - \mathbf{r}_l)\right]\right). \qquad (1.29)$$

Eq. (1.27) does not depend on the backscattering angle and is called incoherent contribution or diffuson. Eq. (1.28) is angle dependent and is called coherent contribution or cooperon. Eq. (1.28) represents the most interesting case as it highlights the interference between direct and reverse paths and assumes its maximum value of 1 in the backscattering direction when $\mathbf{k}_{in} + \mathbf{k}_{out} =$ The coherent contribution is also known as the coherent backscattering effect.

After this overview of the main ingredients used in mesoscopic optics, in the next sections we will introduce some concepts crucial to understand noise analysis.

1.3 Noise spectral density

Let us consider a signal $i(t)$. The Fourier transform of $i(t)$ is given by

$$i(\Omega) = \frac{1}{T} \int_{-\frac{T}{2}}^{\frac{T}{2}} i(t) \exp(i2\pi\Omega t)\, dt. \qquad (1.30)$$

where T is the measurement time. The average power is given by

$$\overline{i^2} = \frac{1}{T} \int_{-\frac{T}{2}}^{\frac{T}{2}} i^2(t) dt. \qquad (1.31)$$

It can be shown [51] that

$$\overline{i^2} = \int_0^\infty S(\Omega)\, d\Omega, \qquad (1.32)$$

with $S(\Omega)$ known as the noise spectral density, defined as

$$S(\Omega) \equiv \frac{2}{T} |i(\Omega)|^2. \qquad (1.33)$$

An important theorem, the Wiener-Khinchin theorem, relates the correlation function $\overline{i(t)\, i(t+\tau)}$ to $S(\Omega)$ in the following way

$$S(\Omega) = \int_0^\infty \overline{i(t)\, i(t+\tau)} \exp(i2\pi\Omega\tau)\, d\tau. \qquad (1.34)$$

1.4 The shot noise formula

In this section we give a brief outline of the basic steps necessary to recover the shot noise formula. The shot noise formula is crucial in the field of photon detection because it corresponds to the signature that the detected photons are in a coherent state, which is the usual state for the photons emitted by a laser operating above threshold. Let us consider a stream of photons that impinge on a photon detector at random times, with the detection events being independent from one another. These two properties correspond to requiring that the distribution of the photons is Poissonian. Our goal is to calculate the power spectrum $S\left(\Omega\right)$ of this train of pulses. The total current $i(t)$ is given by

$$i(t) = \sum_{k=1}^{N} g(t - t_k), \tag{1.35}$$

where $g(t)$ indicates the shape of the pulses and t_k indicates the instant at which the pulses are acquired. Let $G\left(\Omega\right)$ be the Fourier transform of $g(t)$

$$G\left(\Omega\right) = \int_{-\infty}^{+\infty} g\left(t\right) \exp\left(i2\pi\Omega t\right) dt. \tag{1.36}$$

By making use of the fact that the pulses occur at random times and are independent from one another we obtain, by using eq. (1.33),

$$\overline{S\left(\Omega\right)} = \frac{2\overline{N}\left|G\left(\Omega\right)\right|^2}{T}, \tag{1.37}$$

where $\overline{S\left(\Omega\right)}$ indicates the average power spectrum. In case we have an electric current with electrons of charge e, whose charge is localized in a needle-like pulse, we can pose $g(t) = e\delta(t)$. That leads us to

$$\overline{S\left(\Omega\right)} = 2e\overline{i}, \tag{1.38}$$

with $\overline{i} = \frac{e\overline{N}}{T}$. Eq. (1.38) is the shot noise formula that makes clear that the spectrum of a train of random pulses is frequency independent and depends on the average current intensity and the electron charge.

1.5 Photon statistics and the Fano factor

Photon statistics allows to investigate the fluctuations of light. The Poisson distribution plays a central role as the photons emitted by a laser above threshold obey Poisson statistics. Poisson statistics emerges by considering emission of independent photons and is characterized by the fact that the variance of the distribution equals the mean number of photons. Commonly, all fluctuations are referenced to the variance of a Poisson distribution according to the following scheme

$$(\Delta n)^2 > \overline{n}, \tag{1.39}$$

$$(\Delta n)^2 = \overline{n}, \tag{1.40}$$

$$(\Delta n)^2 < \overline{n}, \tag{1.41}$$

where with $(\Delta n)^2$ we indicate the variance $(\Delta n)^2 \equiv \overline{n^2} - \overline{n}^2$ of the photon distribution and with $\overline{n}$ the average number of photons. Eq. (1.39) identifies the super-Poissonian regime, eq. (1.40) the Poissonian regime and eq. (1.41) the sub-Poissonian regime. A useful figure of merit, widely used in the quantum optics community, is the Fano factor that quantifies the light fluctuations. The Fano factor F is defined as

$$F \equiv \frac{(\Delta n)^2}{\overline{n}}. \tag{1.42}$$

This figure of merit compares the fluctuations of a distribution to the ones of a Poisson distribution, that displays $F = 1$. The Fano factor is used to quantify light fluctuations as well as electron fluctuations in electronic systems, but the fluctuations exhibited by photons and electrons are profoundly different from one other, as we are going to explain in the following section.

1.6 Photon and electron intensity correlations

In this section we will introduce some of the main differences between light and electrons and analyze them in terms of their statistical consequences. It is in fact these statistical properties that are probed and extracted in experiments where noise is the main observable.

A crucial difference between photons and electrons is that they obey two different types of statistics. Electrons obey Fermi statistics and are fermions while photons are bosons and obey Bose-Einstein statistics. More specifically, fermions are bound by the Pauli principle that states that no more than a single electron can occupy a quantum state. On the contrary, photons are not subjected to this restriction, so there is no limit to the number of photons that can occupy a state. This important difference between photons and electrons, and the fact the electrons are charged particles and photons have no charge, implies that the mechanism for which correlations are developed are different.

Correlations are best individuated by resorting to Hanbury-Brown and Twiss type experiments [52], illustrated in fig. (1.6), where intensity-intensity correlations between two streams of particles are measured. The measured quantity is defined as

$$g^{(2)} = \frac{\overline{I_1(t) I_2(t+\tau)}}{\overline{I_1(t) I_2(t)}}, \tag{1.43}$$

where I_1 and I_2 refer to the intensity measured by the two detectors involved in the experiment and τ is the time delay between the events registered by the two

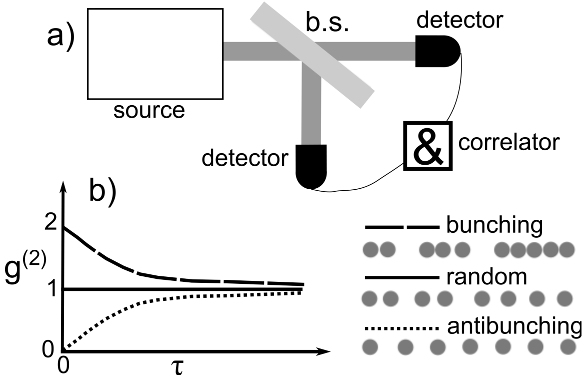

Figure 1.6: Schematic description of a typical Hanbury-Brown and Twiss experiment. b.s. stands for beam splitter. a) Intensity correlations between two streams of photons are measured by collecting the intensities at two detectors. As soon as one of the two detectors records an event the measurement starts at time $\tau = 0$ and it is stopped when photons are collected by the other detector (start-stop measurements). The main aim of the experiment is to measure $g^{(2)}$. b) Typical outcomes of the experiment. In case of photons emitted in a random fashion (solid line) there will be no correlation displayed at any time and $g^{(2)} = 1$. In case of bunched events (dashed line) there will be high probability to register clicks at $\tau = 0$ because photons belonging to the same bunch will be distributed by the beam splitter on the two detectors. Correlations are therefore present. Consequently, in the short time regime ($\tau < \tau_c$, with τ_c the coherence time of the source) $g^{(2)} > 1$. As time goes by photons will be collected that belong to different bunches and the intensity correlation will decay to the value assumed in the no correlation case, when the photons are emitted in a random fashion. Antibunching (dotted line) is displayed for example by single photon sources. In this case the emitted photons are equally spaced in time and at $\tau = 0$ we will have an anticorrelation because if a single photon illuminates one of the two detectors it cannot simultaneously trigger the other. Consequently, in the short time regime $g^{(2)} < 1$. Also in this case if the measurements are performed over a time exceeding the coherence time of the source all correlations vanish.

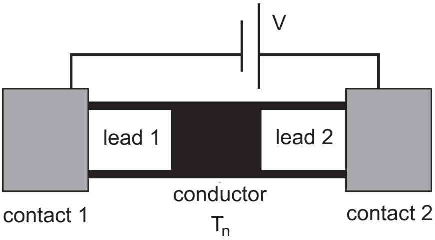

Figure 1.7: Schematics of a setup to investigate transmission of electrons through mesoscopic conductors. A bias voltage V is applied between the two contacts and electrons flow through the conductor. The values T_n are the transmission probabilities that the electrons have to traverse the system.

detectors. The initial experiments aimed successfully at using correlations to measure the diameter of distant stars. Subsequently this type of experiments were intensively used to confirm or disproof statements about the nature of light and its particle-wave duality. While measuring intensity-intensity correlations for photons is routine nowadays, the demonstration of the fermionic Hanbury-Brown and Twiss experiment, whereby electrons show anti bunching, has been performed only recently, given to many experimental challenges that had to be overcome [53, 54].

1.7 Fluctuations of photons and electrons in mesoscopic systems

Correlations allow for a different behaviour of noise for photons and electrons. In a mesoscopic conductor these correlations are responsible for a decrease of the electron noise power from the classical value given by Poisson statistics.

Let us consider a mesoscopic conductor. As shown in eq. (1.38) the noise power is given by

$$S_P = 2e\bar{i}, \tag{1.44}$$

where the subscript P refers to the Poisson distribution obeyed to by electrons. In this case the intensity is [55, 56]

$$\bar{i} = \frac{2e^2}{h} V \sum_{n=1} T_n, \tag{1.45}$$

where T_n indicates the transmission probabilities in the conductor, h Planck's constant and V a given applied voltage. Eq. (1.45) is reminiscent of the classical Ohm relationship $I = \sigma V$ where σ is the conductance. In this case $\sigma = \frac{2e^2}{h}$ is the conductance quantum. A schematic setup that illustrates the main components of an experiment in mesoscopic electronics is presented in fig. (1.7). The noise formula at zero temperature yields [57, 58]

$$S = 2e\frac{2e^2}{h}V\sum_{n=1}^{N}[T_n(1-T_n)]. \tag{1.46}$$

The $(1-T_n)$ factor states the decrease of the noise induced by the Pauli principle. Notice that $T_n \ll 1$ implies Poisson statistics because $F = 1$, having defined $F \equiv \frac{S}{S_p}$. This property can be seen by using eqs. (1.45) and (1.44). If $T_n = 1$ or $T_n = 0$ there is no contribution to the shot noise, in other words fully open or closed channels do not contribute to the shot noise and induce a suppression of the shot noise with respect to the Poisson value. In particular the case $T_n = 1$ shows the action of the Pauli principle: a completely open channel means that the stream of electrons passes undisturbed and there are no fluctuations, $S = 0$, because the exclusion principle dictates the number of electrons that each state is allowed to have. Therefore the values that contribute to the depletion of the shot noise are the highly transmitting channels and the almost closed ones. A clear example of this depletion mechanism manifest itself in disordered conductors where the probability distribution of the transmission eigenvalues is bimodal [59, 60], that means that almost fully open and closed channels are a majority in disordered conductors. In this case eq. (1.46) leads to [61]

$$F_{out} = \frac{1}{3}. \tag{1.47}$$

We notice immediately a reduction of $\frac{2}{3}$ in the noise power with respect to the Poisson value. Eq. (1.47) holds true when $L \gg \ell$, where ℓ is the mean free path. The other intriguing property of formula (1.47) is that F goes back to one when L reaches and becomes greater than the localization length, ξ_{loc} because in this case the transmission probabilities becomes very small. Formula (1.47) is a signature that the transport in the medium is of diffusive nature. It is very interesting that this noise suppression takes specific values for different systems, for example $\frac{1}{2}$ for a symmetric double-barrier junction [62, 63], and $\frac{1}{4}$ for a chaotic cavity, [64, 65]. Thus, by investigating the noise it is possible to identify different states of electron transport in the medium.

In optics, theory and experiments about the propagation of optical noise have made their appearance at a later stage, that means that still much effort has to be channelled in this field. Beenakker et al. [66] showed that the propagation of coherent radiation in disordered media is given by

$$F_{out} = 1 + (t^\dagger t)_{mm}(F_{in} - 1) + 2f(\omega_0, T)\frac{[t^\dagger(1 - rr^\dagger - tt^\dagger)t]_{mm}}{(t^\dagger t)_{mm}}, \tag{1.48}$$

where F_{in} is the Fano factor of the incoming radiation, F_{out} the Fano factor of the outgoing radiation, t and r represent the transmission and reflection matrices, f the Bose-Einstein function, and m the mode of the incoming radiation. For $F_{in} = 1$ we revert to an incoming radiation in a coherent state. The function f is negligible at optical wavelengths and room temperatures, therefore normally so is the third term

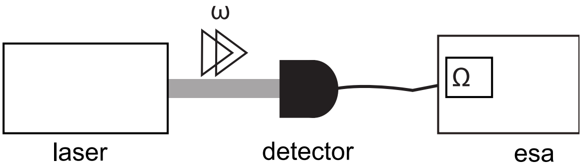

Figure 1.8: An electronic spectrum analyzer (esa) is employed to investigate the noise content of the optical signal. The frequency of the optical carrier ω is in the Terahertz range while the spectrum analyzer processes frequencies Ω up to the Gigahertz range. The analyzer downshifts the frequency content of the signal and allows thus for its investigation over a frequency range which is easier to detect.

in eq. (1.48). It is seen that in an passive system with no absorption conservation of energy implies $rr^\dagger + tt^\dagger = 1$. Therefore in this case $F_{out} = 1$ for an incoming radiation in the coherent state with $F_{in} = 1$. Absorption and gain in the system imply that its scattering matrix is no longer unitary and $rr^\dagger + tt^\dagger \neq 1$. Furthermore for gain $f < 0$ while for absorption $f > 0$. These considerations lead for both gain and absorption to $F_{out} > 1$,with $F_{in} = 1$. The case of absorption is particularly interesting as it can be compared to the suppression observed in the case of disordered conductors. In an absorbing random photonic material, illuminated with light in the coherent state in a transmission configuration we have

$$F = 1 + \frac{3}{2} f, \tag{1.49}$$

when $L \gg \xi_a$, where ξ_a is the absorption length [67]. This interesting photonic analogue to the electronic case has has not been observed yet, mainly because the function f at room temperatures is minuscule. In contrast to the electronic case, where localization restores Poisson statistics, in this case localization has no effect on the outgoing Fano factor.

1.8 Laser light fluctuations

It is crucial to understand the origin of the light fluctuations displayed by laser light, as the the laser is the main light source used in our experiments.

One source of the fluctuations of the emitted radiation is given by spontaneous emission. Spontaneous emission noise is of quantum origin and is due to the inevitable presence of radiation that is randomly emitted from the amplifying laser medium and interferes with the light generated by stimulated emission. Light emitted by spontaneous emission has no phase relationship with light emitted by stimulated emission and that creates phase and intensity fluctuations. Phase fluctuations lead to a broadening of the spectral feature of the emitted radiation. In the following we will be interested in intensity noise.

The full quantum model of laser noise takes into account the pump noise, the vacuum noise due intracavity losses and introduced at the output coupler, spontaneous emission noise and dipole fluctuation noise [68–71].

The intensity laser spectrum can be broadly divided into a low frequency spectrum and a high frequency spectrum. The low frequency part of the spectrum contains most of the features specific to our laser system, like for example the relaxation oscillation, related to fluctuations of the pump power, whose frequency depends on many parameters (among others intracavity power, resonator losses, gain medium, round trip time of the resonator).

Broadly speaking there are two types of laser optical noise: classical noise and quantum noise. Classical noise encapsulates all types of optical noise that can be reduced by resorting to better optical components, stabilizing the laser cavity, reducing the vibrations of the system, etc. The amount of the reduction depends on the ability of the experimentalist and the quality of the optical and electronic components. To highlight these technical causes, this type of noise is also termed technical noise.

The minimum noise level is intrinsic to the fundamental nature of light. This noise level is called shot noise, also known as quantum noise to stress the particle nature of light of being composed of photons. The main experimental difference between these two types of noise is their scaling with optical power. Classical noise scales quadratically as function of power while quantum noise scales linearly. These two important signatures are commonly used to tell one type of noise from the other. Classical noise is very often called excess noise to stress the fact that the intensity of its fluctuations stays above the shot noise level, which is then regarded as a reference level. The shot noise divides the classical world from the quantum world. Using methods employed in quantum optics it is possible to reach below the quantum noise level. The most common technique to reduce the noise below the shot noise level is squeezing [25].

There is a distinction that needs to be made. In literature, the word quantum noise is used invariably in relation with more than one cause. For example, it is spoken of shot noise as quantum noise but also spontaneous emission noise is labelled as quantum noise. It is also often spoken of the quantum noise limit (QNL) but it is not clear at a first glance which quantum noise it is referred to. The word quantum noise refers to all light fluctuations that are quantum in essence and require quantum mechanics to be fully accounted for. In this fashion spontaneous emission noise is quantum noise as well as shot noise. However these two types of noise refer to different quantum mechanisms: spontaneous emission occurs when an atom, in an excited state, for example in a laser medium, relaxes down onto a lower excited state and emits a photon. Shot noise refers to the intensity fluctuations of light in the coherent state and it is evidence of the corpuscular nature of light. It is then more precise and accurate to say that a laser is shot noise limited rather than quantum noise limited, meaning that its intensity noise spectrum is at the shot noise level.

In our experiments we use an electronic spectrum analyzer to investigate the noise content of our signal as it is schematized in fig. (1.8). Two main frequency scales are important for our experiments. The laser frequency, that for light emitted at 800 nm is in the Terahertz regime, and a slower varying frequency, often in the MHz regime, that is the detection frequency of the spectrum analyzer. Investigating the low frequency spectrum of the laser corresponds to observing the system for a long time. Over such a long time many disturbances have the chance to disrupt the signal and being detected. On the contrary, studying the high frequency noise spectrum is equivalent to looking at the system's short time behaviour. Over such a short time span most of the noise sources can not manifest themselves. In this situation the only noise present is the photon shot noise. At high radio frequencies (RF) vacuum noise due to intracavity losses becomes negligible and what is left is the vacuum noise introduced by the outcoupling beamsplitter which gives rise to the shot noise. All classical noise sources become negligible.

1.9 This thesis

Only recently techniques and ideas borrowed from the investigation of disordered electronic systems and the field of quantum optics have been combined and employed to investigate transport of light in complex optical systems theoretically [72–75] as well as experimentally [76, 77]. In this thesis we focus our attention on optical noise in disordered optical systems. In more detail, we will investigate the propagation of radiation with Fano factor higher or equal to 1 in photonic random media.

In chapter 2, we investigate the total reflection of excess and shot noise off TiO_2 samples, showing different scaling for classical and shot noise in reflection. Furthermore, we predict and observe a liner dependence of the total reflection on the incoming Fano factor and confirm that optical noise is an alternative method to extract the sample's mean free path. In chapter 3, we make use of coherent backscattering noise measurements to investigate the transport of optical noise as function of the order of scattering and compare noise measurements to the ones of classical intensity coherent backscattering . We demonstrate experimentally an enhancement higher than the classical value of two for the excess noise measurements. In this chapter we also theoretically show that the enhancement of the noise cone contains information about the mesoscopic properties of the system, allowing to extract the g value of the system. Finally, in chapter 4 we present a setup and measurements aimed at directly inducing and detecting mesoscopic correlations in strongly scattering nanowires systems.

CHAPTER 2

Total reflection of quantum and classical noise

In this chapter we provide a full quantum theory based on a random matrix approach to describe the total reflection of photon noise from random media and present experimental results that match the theoretical prediction.

2.1 Introduction

Transport of photon noise in transmission trough multiple scattering samples was experimentally investigated by P. Lodahl et al. [78]. A characteristic scaling for the transport of classical and shot noise was found. The size scaling parameter is the ratio $\rho \equiv \frac{\ell}{L}$ where ℓ is the mean free path and L is the sample thickness. It was found that shot noise scales linearly with ρ while classical noise quadratically.

In this chapter we want to investigate the total reflection of photon noise from random multiple scattering samples and check the outcome of the experiments against the theory presented in [79].

One of the differences between total transmission and total reflection measurements is that total reflection includes shorter paths than total transmission measurements. Furthermore, joint total transmission and total reflection intensity measurements can provide important information about the degree of absorption that takes place in the material under investigation. In the ideal case of no absorption $T + R = 1$ always, where T denotes total transmission and R total reflection. If absorption is present $R+T < 1$. In the remainder of this chapter we will show that, even in absence of absorption, the sum of total noise reflection and transmission

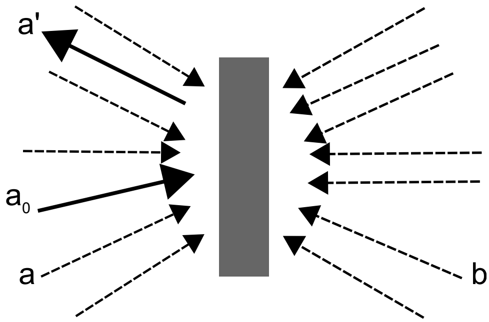

Figure 2.1: Modes impinging on a multiple scattering medium. The illuminated modes, a_0 and a' respectively, are depicted with a solid line. The vacuum modes a and b are depicted with dashed lines.

is in general different from one. Furthermore, we will investigate how the transport of the reflected noise evolves, as function of frequency, sample parameters and incoming fluctuations.

The chapter is structured as follows: we begin in section 2.2 by illustrating the theory needed to describe the total reflection of noise in multiple scattering media. In section 2.3 a parallel between noise and intensity measurements is drawn. Section 2.4 is dedicated to the description of the experimental setup and its characterization. Section 2.5 describes total intensity transmission and reflection experiments. Section 2.6 revolves around the experiments performed to measure the total reflection of noise from random media. Finally, in section 2.7 we compare the theory to the experimental results.

2.2 Theory

To model our experiment we make use of the theory of Lodahl et al. [79] that was employed to explain the total transmission of photon noise. We begin by writing down the expression for the reflection of a single mode from channel a_0 into channel a'

$$\hat{a}_{a'} = \sum_a r_{aa'}\hat{a}_a + \sum_b t_{ba'}\hat{a}_b = r_{a_0a'}\hat{a}_{a_0} + \sum_{a\neq a_0} r_{aa'}\hat{a}_a + \sum_b t_{ba'}\hat{a}_b, \tag{2.1}$$

where $\hat{a}$ indicates the destruction operator, the indexes a and b denote the incoming and reflected vacuum modes respectively, a' indicates the observed reflected mode, and a_0 the incoming illuminated mode. Finally, r and t are the classical reflection and transmission coefficient, respectively. The considered configuration is sketched in fig. (2.1). This model describes the following situation: an incoming state impinges on the scattering medium in channel a_0 and is reflected into channel a'. This is described by the term $r_{a_0a'}\hat{a}_{a_0}$, with $r_{a_0a'}$ being the reflection coefficient from channel a_0 into channel a'. The two sums describe the presence of vacuum channels entering the medium in transmission, from channel b to channel a' and in reflection from channel $a \neq a_0$ to channel a'. In the reflected channel a' we have contributions from the vacuum and the incoming illuminated mode.

The total reflection is defined as

$$\hat{R} \equiv \sum_{a'} \hat{a}^{\dagger}_{a'} \hat{a}_{a'}, \tag{2.2}$$

where the sum is carried over all outgoing channels. The fluctuations of the total reflection are

$$\left\langle \delta\hat{R}^2 \right\rangle = \left\langle \hat{R}^2 \right\rangle - \left\langle R \right\rangle^2 = \left\langle \left(\sum_{a'} \hat{a}^{\dagger}_{a'} \hat{a}_{a'} \right)^2 \right\rangle - \left\langle \sum_{a'} \hat{a}^{\dagger}_{a'} \hat{a}_{a'} \right\rangle^2 , \tag{2.3}$$

where with $\langle\rangle$ we indicate the quantum expectation value. Developing the squares in eq. (2.3) and using the fact that, due to the independence of the channels, $\left\langle \hat{a}^{\dagger}_{a'} \hat{a}_{a'} \hat{a}^{\dagger}_{a'_1} \hat{a}_{a'_1} \right\rangle = \left\langle a^{\dagger}_{a'} \hat{a}_{a'} \right\rangle \left\langle \hat{a}^{\dagger}_{a'_1} \hat{a}_{a'_1} \right\rangle$ we get

$$\begin{aligned} \left\langle \delta\hat{R}^2 \right\rangle &= \sum_{a'} \left[\left\langle \hat{a}^{\dagger}_{a'} \hat{a}_{a'} \hat{a}^{\dagger}_{a'} \hat{a}_{a'} \right\rangle - \left\langle \hat{a}^{\dagger}_{a'} \hat{a}_{a'} \right\rangle^2 \right] + \\ &- \sum_{a'_1 \neq a'_2} \left[\left\langle \hat{a}^{\dagger}_{a'_1} \hat{a}_{a'_1} \hat{a}^{\dagger}_{a'_2} \hat{a}_{a'_2} \right\rangle - \left\langle \hat{a}^{\dagger}_{a'_1} \hat{a}_{a'_1} \right\rangle \left\langle \hat{a}^{\dagger}_{a'_2} \hat{a}_{a'_2} \right\rangle \right] \\ &= \sum_{a'} \left[\left\langle \hat{I}^2_{a'} \right\rangle - \left\langle \hat{I}_{a'} \right\rangle^2 \right] - \sum_{a'_1 \neq a'_2} \left[\left\langle \hat{I}_{a'_1} \hat{I}_{a'_2} \right\rangle - \left\langle \hat{I}_{a'_1} \right\rangle \left\langle \hat{I}_{a'_2} \right\rangle \right], \end{aligned} \tag{2.4}$$

where with $\hat{a}^{\dagger}$ and $\hat{I}_{a'} \equiv \hat{a}^{\dagger}_{a'} \hat{a}_{a'}$ we indicate the creation operator and the intensity operator relative to channel a' respectively. It is clear that the fluctuations of total reflection depends not only on the fluctuations in each channel, given by the first sum in eq. (2.4). Correlations between different channels play also a role and are given by the second sum in eq. (2.4). In order to evaluate eq. (2.4) we make use of eq. (2.1) and calculate the intensity $\left\langle \hat{I}_{a'} \right\rangle$ in channel a'. First we compute $\hat{I}_{a'}$, and obtain

$$\begin{aligned} \hat{I}_{a'} &= \left| r_{a_0 a'} \right|^2 \hat{a}^{\dagger}_{a_0} \hat{a}_{a_0} + r^*_{a_0 a'} \hat{a}^{\dagger}_{a_0} \left(\sum_{a \neq a_0} r_{aa'} \hat{a}_a + \sum_b t_{ba'} \hat{a}_b \right) \\ &+ \sum_{a \neq a_0} r^*_{aa'} \hat{a}^{\dagger}_a \left(r_{a_0 a'} \hat{a}_{a_0} + \sum_{a \neq a_0} r_{aa'} \hat{a}^{in}_a + \sum_b t_{ba'} \hat{a}_b \right) \\ &+ \sum_b t^*_{ba'} \hat{a}^{\dagger}_b \left(r_{a_0 a'} \hat{a}_{a_0} + \sum_{a \neq a_0} r_{aa'} \hat{a}_a + \sum_b t_{ba'} \hat{a}_b \right). \end{aligned} \tag{2.5}$$

When calculating $\left\langle \hat{I}_{a'} \right\rangle$ we have

$$\left\langle \hat{I_{a'}} \right\rangle = \left| r_{a_0 a'} \right|^2 \left\langle \hat{a}^{\dagger}_{a_0} \hat{a}_{a_0} \right\rangle . \tag{2.6}$$

We now evaluate $\left\langle \hat{I}^2_{a'} \right\rangle$ and that yields

$$\left\langle \hat{I}^2_{a'} \right\rangle = |r_{a_0 a'}|^4 \left\langle \hat{a}^{\dagger}_{a_0} \hat{a}_{a_0} \hat{a}^{\dagger}_{a_0} \hat{a}_{a_0} \right\rangle + |r_{aa'}|^2 \left\langle \hat{a}^{\dagger}_{a_0} \hat{a}_{a_0} \right\rangle \left[\sum_{a \neq a_0} |r_{aa'}|^2 + \sum_{b} |t_{ba'}|^2 \right]. \quad (2.7)$$

For the intensity fluctuations in channel a' we find

$$\begin{aligned} \left\langle \hat{I}^2_{a'} \right\rangle - \left\langle \hat{I}_{a'} \right\rangle^2 &= |r_{a_0 a'}|^4 \left\langle \hat{a}^{\dagger}_{a_0} \hat{a}_{a_0} \hat{a}^{\dagger}_{a_0} \hat{a}_{a_0} \right\rangle \\ &+ |r_{aa'}|^2 \left\langle \hat{a}^{\dagger in}_{a_0} \hat{a}^{in}_{a_0} \right\rangle \left[\sum_{a \neq a_0} |r_{aa'}|^2 + \sum_{b} |t_{ba'}|^2 \right] + \\ &- |r_{a_0 a'}|^4 \left\langle \hat{a}^{\dagger}_{a_0} \hat{a}_{a_0} \right\rangle^2 . \end{aligned} \quad (2.8)$$

Furthermore, we obtain

$$\begin{aligned} \left\langle \hat{I}_{a'_1} \hat{I}_{a'_2} \right\rangle - \left\langle \hat{I}_{a'_1} \right\rangle \left\langle \hat{I}_{a'_2} \right\rangle &= \left| r_{a_0 a'_1} \right| \left| r_{a_0 a'_2} \right| \left\langle \hat{a}^{\dagger}_{a_0} \hat{a}_{a_0} \hat{a}^{\dagger}_{a_0} \hat{a}_{a_0} \right\rangle + \\ &- \left| r_{a_0 a'_1} \right| \left| r_{a_0 a'_2} \right| \left[\left\langle \hat{a}^{\dagger}_{a_0} \hat{a}_{a_0} \right\rangle + \left\langle \hat{a}^{\dagger}_{a_0} \hat{a}_{a_0} \right\rangle^2 \right]. \end{aligned} \quad (2.9)$$

It is convenient to introduce the Fano factor of the incoming radiation to characterize the incoming light state [22]

$$F_{a_0} \equiv \frac{\left\langle \hat{a}^{\dagger}_{a_0} \hat{a}_{a_0} \hat{a}^{\dagger}_{a_0} \hat{a}_{a_0} \right\rangle - \left\langle \hat{a}^{\dagger}_{a_0} \hat{a}_{a_0} \right\rangle^2}{\left\langle \hat{a}^{\dagger}_{a_0} \hat{a}_{a_0} \right\rangle}. \quad (2.10)$$

By using the Fano factor F_{a_0} and eqs. (2.8) and (2.9) we can rewrite $\left\langle \left(\delta \hat{R} \right)^2 \right\rangle$ as following

$$\begin{aligned} \left\langle \left(\delta \hat{R} \right)^2 \right\rangle &= \sum_{b} R^2_{a_0 a'} F_{a_0} \left\langle \hat{n}_{a_0} \right\rangle + R_{aa'} \left\langle \hat{n}_{a_0} \right\rangle - R^2_{a_0 a'} \left\langle \hat{n}_{a_0} \right\rangle \\ &+ \sum_{a'_1, a'_2 \neq a'_1} \left\langle \hat{n}_{a_0} \right\rangle R_{a_0 a'_1} R_{a_0 a'_1} \left[F_{a_0} - 1 \right], \end{aligned} \quad (2.11)$$

where we have used $\hat{n}_{a_0} = \hat{a}^{\dagger}_{a_0} \hat{a}_{a_0}$ and $R_{aa'} = |r_{aa'}|^2$. We now perform ensemble averaging, indicated by $\overline{\bullet}$, and obtain

$$\begin{aligned} \overline{\left\langle \left(\delta \hat{R} \right)^2 \right\rangle} &= N \left[\overline{R^2_{a_0 a'}} \left\langle \hat{n}_{a_0} \right\rangle \left(F_{a_0} - 1 \right) + \overline{R}_{a_0 a'_1} \left\langle \hat{n}_{a_0} \right\rangle \right] \\ &+ \left(N^2 - N \right) \left\langle \hat{n}_{a_0} \right\rangle \overline{R_{a_0 a'_1} R_{a_0 a'_2}} \left[F_{a_0} - 1 \right] \end{aligned} \quad (2.12)$$

where N is the total number of modes. To estimate $\overline{R_{a_0 a_1'}}$ and $\overline{R_{a_0 a_1'} R_{a_0 a_2'}}$ we make use of the following two relationships [80]

$$\overline{R}_{a_0 a_1'} = \left(1 - \frac{\ell}{L}\right) \frac{1}{N}, \tag{2.13}$$

$$\begin{aligned} \overline{R_{a_0 a_1'} R_{a_0 a_2'}} &= \overline{R}_{a_0 a_1'} \overline{R}_{a_0 a_2'} \left(1 + \delta_{a_1' a_2'} - \frac{1 + \delta_{a_1' a_2'}}{N\left(1 - \frac{\ell}{L}\right)}\right) \\ &= \left[\left(1 - \frac{\ell}{L}\right) \frac{1}{N}\right]^2 \left(1 + \delta_{a_1' a_2'} - \frac{1 + \delta_{a_1' a_2'}}{N\left(1 - \frac{\ell}{L}\right)}\right), \end{aligned} \tag{2.14}$$

with ℓ being the mean free path and L the sample thickness. Eq. (2.14) is valid in the limit $\rho \ll 1$.

As already mentioned in chapter 1, g is a crucial parameter in mesoscopic physics, as it quantifies the correlations between multiple scattering paths that occur in the sample. The parameter g is given by [81]

$$g = \frac{N\ell}{L}. \tag{2.15}$$

In reflection, following the same procedure as the one adopted for a transmission configuration, we define

$$g_r \equiv N\left(1 - \frac{\ell}{L}\right). \tag{2.16}$$

In most experimental situations $g_r \gg 1$. To estimate g_r we resort to the formula $N = \frac{2\pi^2 A}{\lambda^2}$ [81], where A is the cross section of the laser beam and λ its wavelength. Using our experimental parameters ($A \sim 5 \cdot 10^{-3}\mathrm{m}^2$, $\lambda = 800$ nm, $\min\{\frac{\ell}{L}\} \sim 0.04$) we obtain $g_r \sim 10^{11}$. Employing definition (2.16) we obtain

$$\overline{\left\langle \left(\delta\hat{R}\right)^2 \right\rangle} = \langle \hat{n}_{a_0} \rangle \left(1 - \frac{\ell}{L}\right) + \langle \hat{n}_{a_0} \rangle \left(F_{a_0} - 1\right) \left(1 - \frac{\ell}{L}\right)^2 \left(1 - \frac{1}{g_r}\frac{\ell}{L}\right). \tag{2.17}$$

The incoming fluctuations can be modelled in the following way

$$\left(\delta\hat{I}^{in}_{a_0}\right)^2 = \langle \hat{n}_{a_0} \rangle + \left(F_{a_0} - 1\right) \langle \hat{n}_{a_0} \rangle. \tag{2.18}$$

Therefore we have that the fluctuations of the total reflection, normalized to the incoming fluctuations, are given by

$$\Gamma_R = \overline{\left\langle \frac{\left(\delta\hat{R}\right)^2}{\left(\delta\hat{I}^{in}_{a_0}\right)^2} \right\rangle} = \left(1 - \frac{\ell}{L}\right) \frac{1}{F_{a_0}} + \left(1 - \frac{1}{F_{a_0}}\right) \left(1 - \frac{\ell}{L}\right)^2 \left[1 - \frac{1}{g_r}\frac{\ell}{L}\right], \tag{2.19}$$

where F_{a_0} characterizes the fluctuations of the incoming radiation. In our case the fluctuations are a function of the noise frequency Ω, that is $F_{a_0} = F_{a_0}(\Omega)$. For shot noise ($sn$) $F_{a_0} = 1$ while for classical noise (cn) $F_{a_0} > 1$. In the two cases of $F_{a_0} = 1$ and $F_{a_0} \gg 1$ we have respectively

$$\begin{aligned} \Gamma_R^{sn} &= \left(1 - \frac{\ell}{L}\right) & (2.20) \\ \Gamma_R^{cn} &= \left(1 - \frac{\ell}{L}\right)^2 \left[1 - \frac{1}{g_r}\frac{\ell}{L}\right] & (2.21) \end{aligned}$$

If we calculate the ratio $\chi \equiv \Gamma_R^{sn} \left(\Gamma_R^{cn}\right)^{-1}$ we obtain

$$\chi = \left[\left(1 - \frac{\ell}{L}\right)\left(1 - \frac{1}{g_r}\frac{\ell}{L}\right)\right]^{-1}. \tag{2.22}$$

For all typical experimental situations ($\overline{g}_r \geq 1$, $\frac{\ell}{L} < 1$), eq. (2.22) predicts

$$\chi \backsimeq \frac{1}{R} > 1, \tag{2.23}$$

with R being the total reflection coefficient. For completeness we also report the result for total transmission obtainable by performing similar calculations

$$\Gamma_T = \left(\frac{\ell}{L}\right)^2 \left(1 - \frac{1}{F_{a_0}}\right) + \frac{\ell}{L}\left(\frac{1}{F_{a_0}}\right), \tag{2.24}$$

where with Γ_T we indicate noise in total transmission and we have neglected g_r^{-1} contributions. Analogously to the reflection case, if we define the ratio $\xi \equiv \Gamma_T^{sn} \left(\Gamma_T^{cn}\right)^{-1}$, we obtain

$$\xi \simeq \frac{1}{T} > 1, \tag{2.25}$$

with T being the total transmission coefficient. The theory predicts that for both transmission and reflection shot noise gets reflected and transmitted more efficiently than classical noise.

In our experiments we measure the noise in total reflection Γ_R and also the incoming Fano factor $F_{a_0}(\Omega)$. If we plot Γ_R versus $F_{a_0}^{-1}$, neglecting g^{-1} contributions, we obtain a linear relationship

$$\Gamma_R = \frac{1}{F_{a_0}}\left(1 - \frac{\ell}{L}\right)\frac{\ell}{L} + \left(1 - \frac{\ell}{L}\right)^2, \tag{2.26}$$

with F_{a_0} gauging the incoming photon noise. Eq. (2.26) predicts a linear behaviour for $\Gamma_R(F_{a_0}^{-1})$. In fig. (2.2, left panel) $\Gamma_R(F_{a_0}^{-1})$ is plotted for a selection of realistic values for $\rho \equiv \frac{\ell}{L}$. In section 2.7 we will use our experimental data to check the validity of the theory presented in this section and in particular of eq. (2.26).

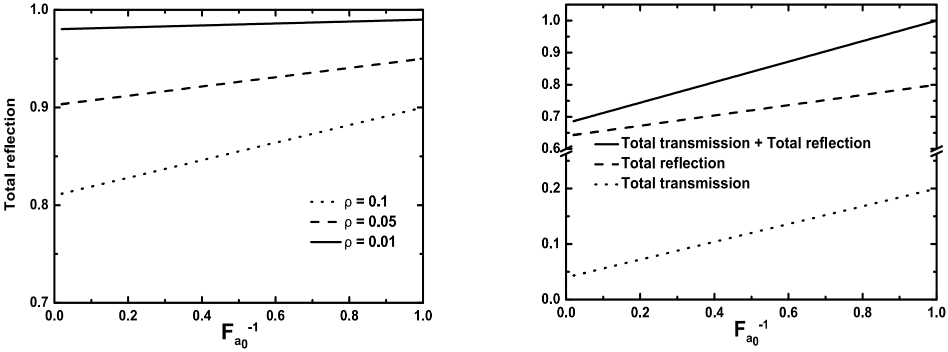

Figure 2.2: (left) Calculated total reflection of noise Γ_R is plotted for three values of $\rho \equiv \frac{\ell}{L}$, as function of $F_{a_0}^{-1}$. (right) Calculated total noise transmission Γ_T, total noise reflection Γ_R, and the sum of the two $\Gamma_T + \Gamma_R$, are plotted as function of $F_{a_0}^{-1}$. We have employed $\rho \equiv \frac{\ell}{L} = 0.2$. While $T + R = 1$ always, noise displays $\Gamma_T + \Gamma_R = 1$ only for $F_{a_0} = 1$.

2.3 Total reflection and transmission of noise and intensity

In this section we draw a parallel between noise and intensity measurements, for the case of non absorbing samples. For total intensity measurements we have

$$\begin{aligned} T &= \frac{\ell}{L}, & (2.27)\\ R &= 1 - T, & (2.28)\\ R + T &= 1. & (2.29) \end{aligned}$$

where T indicates total transmission, R total reflection, ℓ the mean free path and L the sample thickness. For sake of simplicity in eqs. (2.27) and (2.28) we have neglected the extrapolation lengths. The extrapolation lengths are of the same order as ℓ and are introduced to properly take into account the effect of the boundaries when dealing with propagation of light in a random medium [82]. Employing eqs. (2.24) and (2.26) for the total transmission and reflection of photon noise we obtain

$$\Gamma_R + \Gamma_T = 1 + \frac{2\ell}{L}\left(1 - \frac{\ell}{L}\right)\left(\frac{1}{F_{a_0}} - 1\right), \tag{2.30}$$

where Γ_T and Γ_R denote total noise transmission and total noise reflection. It is evident that while the sum of total intensity reflection and transmission is always equal to 1, for photon noise, eq. (2.30), we recover the value of one only at high frequency in the shot noise case, that is when $F_{a_0} = 1$. In all other cases the dependence on F_{a_0} is always present, and in general $\Gamma_R + \Gamma_T \neq 1$. In the extreme case $F_{a_0} \gg 1$ we have $\Gamma_R + \Gamma_T = 1 - \frac{2\ell}{L}\left(1 - \frac{\ell}{L}\right)$. In fig. (2.2, right panel) calculations for total noise transmission, reflection and the sum of transmission and reflection are plotted as function of the reciprocal of the incoming Fano factor $F_{a_0}^{-1}$.

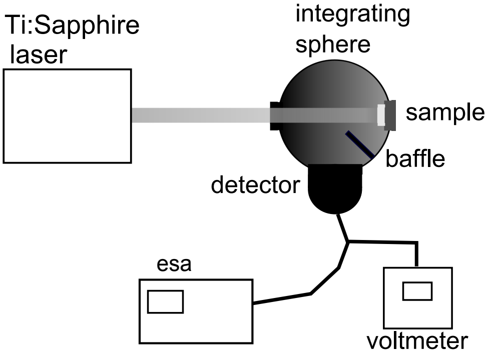

Figure 2.3: Sketch of the experimental setup used to measure total reflection of both classical and quantum noise. A Ti:Sapphire laser and an integrating sphere are used as source and to collect the reflected light, respectively. The baffle is needed to prevent specularly reflected light from hitting the detector. An electronic spectrum analyzer is employed to measure the noise content of the signal and a voltmeter to measure its intensity.

2.4 Experimental setup and characterization

In this section we describe the experimental setup used to measure total reflection of noise from multiple scattering samples. The setup is illustrated in fig. (2.3). We used a Ti:Sapphire laser as light source. This laser can be used both as a shot and classical noise source as its noise spectrum is shot noise limited at high frequencies ($\Omega > 1$ MHz) and dominated by classical noise at low frequencies ($\Omega < 1$ MHz). To collect the totally reflected noise we use an integrating sphere that is connected to a detector (Thorlabs PDA55). The detector is then coupled to an electronic spectrum analyzer to investigate the noise content of the signal.

The DC component at zero frequency was filtered out by means of an electronic filter to protect the spectrum analyzer. First the scaling of quantum and classical noise was investigated with no sample. A commercial voltmeter was used to monitor the intensity output at the exit port of the integrating sphere. The laser power was progressively increased and intensity and noise readings were recorded by means of the voltmeter and the spectrum analyzer, respectively. The classical and shot noise data have been obtained by integrating the spectra over the $[0.2-0.4]$ MHz and $[3-4.55]$ MHz regions, respectively. The measured scaling is showed in fig. (2.4). In the next section we will describe total intensity transmission and reflection experiments performed on strongly scattering random TiO_2 samples.

2.4.1 Samples

The TiO_2 samples [83] used for the intensity as well as noise measurements were made using commercial rutile pigment. The TiO_2 particles have a size distribution $d = 220 \pm 70$ nm, with d being the diameter of the particles. The prepared samples have a thickness that varies from 1.43 μm to 18 μm and the uncertainty on the thickness is ± 0.3 μm. The thickness and the uncertainty on the thickness were

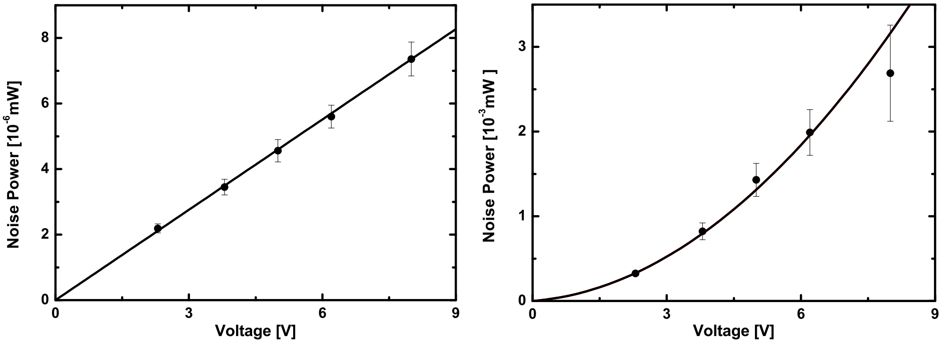

Figure 2.4: (left) Linear scaling of quantum noise versus voltage. The solid line is a linear fit (right). Quadratic scaling of classical noise versus voltage. In both cases no sample was used. The data points were recorded by slowly increasing the laser power and measuring intensity with the voltmeter and the correspondent noise level with the spectrum analyzer. The solid line is a quadratic fit.

extracted with a microscope by measuring the thickness on ten different positions. The samples are mounted on a glass substrate that is ~ 3 mm thick.

2.5 Experiment: total reflection and transmission of intensity

In this section we present total transmission and reflection intensity experiments on TiO_2 samples.

The goal of these experiments is to extract the mean free path ℓ of the samples. The obtained values for the mean free paths will then be compared to the ones extracted from noise measurements.

The total transmission and reflection intensity measurements have been performed by using the setup described in fig. (2.3). The voltmeter has been used to perform the intensity measurements. An important difference between the total reflection and transmission measurements is the reference used. For the measurements in total transmission a glass substrate is used as reference. For the measurements in total reflection, reference measurements are taken with the integrating sphere closed off at one of its ports. The coating of the port and of the interior of the integrating sphere are the same.

The measurements are presented in fig. (2.5). The total transmission data are compared to

$$Y_T = \frac{z_1 + \ell}{L + z_1 + z_2}. \tag{2.31}$$

The total reflection data are compared to

$$Y_R = B_R \left(1 - \frac{z_1 + \ell}{L + z_1 + z_2}\right), \tag{2.32}$$

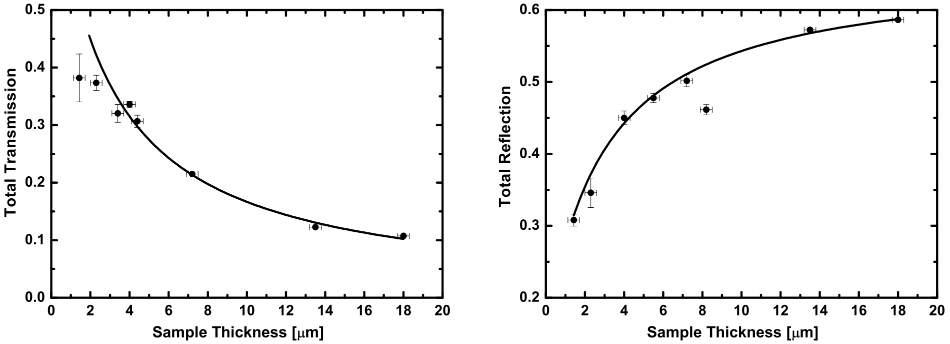

Figure 2.5: (left) Total intensity transmission measurements. The solid line is a fit to the data. (right) Total reflection intensity measurements. The solid line is a fit to the data.

where z_1 and z_2 are the extrapolation lengths that take into account the effects of the sample boundaries. The extrapolation lengths were previously measured for our series of TiO_2 samples [84] and their values are $z_1 = 1.71\ell$ and $z_2 = 1.77\ell$ respectively. The fit parameters are ℓ and B_R. To fit the total transmission data only ℓ was used as fit parameter. To recover a good agreement between the total reflection data set and the theory the additional fit parameter B_R had to be used. From the fit we obtain $B_R = (0.659 \pm 0.006)$. $B_R < 1$ is an indication that our value for our reference measurement is too high. The fact that our reference measurement was too high could be due to the fact that the light hitting the detector was not completely diffused and retained a single scattering component. According to [85] the calculated ratio of total to first order reflection for incidence and reflection along the normal to the sample surface is 8.455, considering an albedo of 1, infinite sample thickness and isotropic scattering. Thus the single scattering component is not negligible. Once the scaling parameter B_R is introduced, fitting eqs. (2.31) and (2.32) to the the total transmission and reflection data sets respectively, produces fully compatible mean free paths. From the total transmission and reflection data sets we obtain $\ell = (0.78 \pm 0.01)$ μm and $\ell = (0.84 \pm 0.07)$ μm, respectively.
In the following section noise measurements in total reflection are presented.

2.6 Experiment: total reflection of photon noise

In this section we report on total reflection of photon noise for a series of eight TiO_2 samples. The measurements are reported in fig. (2.6) along with reference measurements.

The reference measurements were performed by closing off the integrating sphere at one of its ports in the same way as it was done with the total intensity reflection measurements. The reference measurement shows the highest noise reflection, as expected, because the majority of the light is reflected back into the integrating sphere. The electronic background trace is around 10 dB lower than the noise

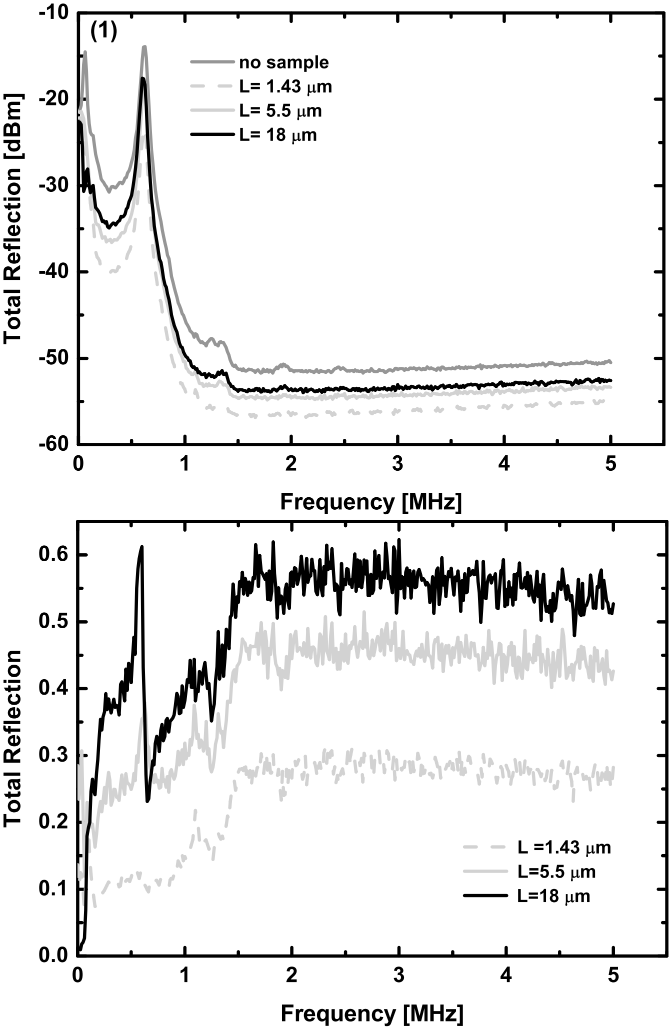

Figure 2.6: (top) Total reflection of photon noise from a series of three samples. The top line is a reference measurement. (bottom) Photon noise in total reflection normalized to the reference measurement trace from (1).

trace for the thinnest sample. To quantify the noise transmission we divide our measurements by the reference noise trace and obtain the data reported in fig. (2.6, lower panel). Two regimes are clearly visible, the low frequency one and the high frequency one. As predicted by the theory of eqs. (2.23) and (2.25) the data show that the quantum noise gets reflected more efficiently than the classical noise. In the next section we will analyze the results obtained in the experiment and compare them to the theory from section 2.2.

	theory	
data set	classical	quantum
classical	$\ell = (0.98 \pm 0.08)\mu\text{m}$	$\ell = (2.4 \pm 5.4)\mu\text{m}$
	$B_{CN} = (0.50 \pm 0.02)$	$B_{SN} = (0.41 \pm 0.28)$
quantum	$\ell = (0.28 \pm 0.01)\mu\text{m}$	$\ell = (0.97 \pm 0.09)\mu\text{m}$
	$B_{CN} = (0.59 \pm 0.01)$	$B_{SN} = (0.63 \pm 0.02)$

Table 2.1: ℓ, B_{CN} and B_{SN} obtained in two ways: (1) Fitting the shot and classical noise theory to the shot and classical noise data sets respectively. (2) Fitting the shot and classical noise theory to the classical and shot noise data sets respectively. Only the combination of quantum noise data with quantum noise theory and the combination of classical noise data with classical noise theory produce consistent and correct results.

2.7 Analysis

In this section we compare the predictions from theory to the experimental results. In order to achieve that we use the noise data, some of which are displayed in fig. (2.6)2. We average each trace over two frequency intervals representative of the two noise contributions. We select the interval $[0.25 - 0.35]$ MHz for the classical noise and $[3 - 4.55]$ MHz for the quantum noise regime, respectively. Subsequently per each of the two regimes the obtained average values are plotted vs. the sample thickness and fitted to the theory of section 2.2. This is shown in fig. (2.7), where the presented data are compared to the following expressions

$$\Gamma_{R_{sn}} = B_{sn} \left(1 - \frac{\ell + z_1}{L + z_1 + z_2} \right), \tag{2.33}$$

$$\Gamma_{R_{cn}} = B_{cn} \left(1 - \frac{\ell + z_1}{L + z_1 + z_2} \right)^2. \tag{2.34}$$

The subscripts sn and cn indicate quantum and classical noise respectively. The fit parameters are ℓ and B; z_1 and z_2 are the extrapolation lengths, that are proportional to ℓ. Eqs. (2.33) and (2.34) are obtained from eqs. (2.20) and (2.21). Results from fitting eqs. (2.33) and (2.34) to the data are summarized in table (2.1).

To further check our approach we show that the classical noise theory fails to explain the quantum noise data, as well as the quantum noise theory does not allow for an extraction of realistic sample parameters from the classical noise data. This is evident by looking at fig. (2.7) and table (2.1).

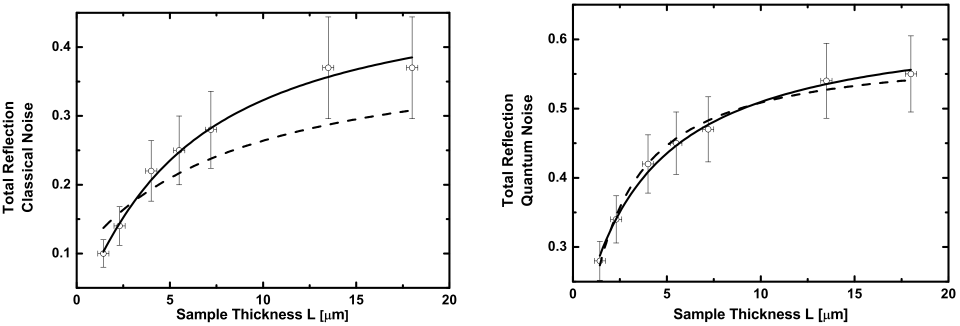

Figure 2.7: (left) Total reflection of classical noise as function of the sample thickness L. Each data point (open circles) has been obtained by averaging the noise spectra over $[0.25-0.35]$ MHz. The solid line is a fit to the classical noise theory $\Gamma_{R_{cn}}$, the dashed line is a fit to the quantum noise theory $\Gamma_{R_{sn}}$. The theory for quantum noise fails to fit classical noise data. (right) Total reflection of quantum noise as function of the sample thickness L. Each data point (open circles) has been obtained by averaging the noise spectra over the range $[3-4.55]$ MHz. The solid line is a fit based on the quantum noise theory, the dashed line is a fit based on the classical noise theory. Although the classical noise theory seems to fit the quantum noise data, the extracted value for the mean free path ℓ is not acceptable because in disagreement both with the value obtained by fitting the quantum noise theory to the data and the one obtained by independent intensity measurements.

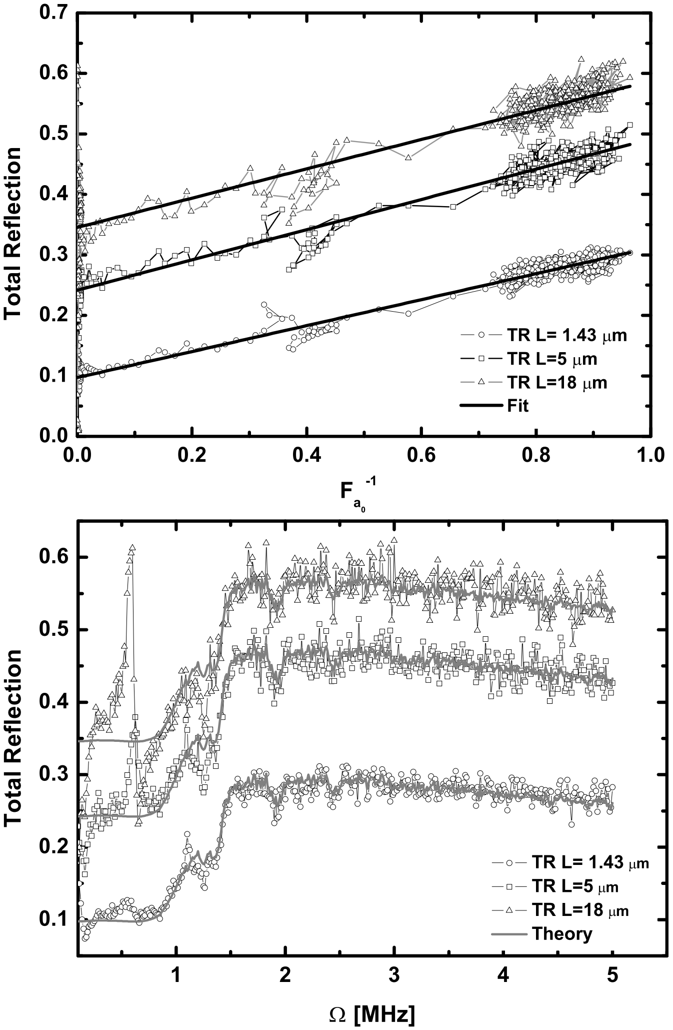

Figure 2.8: (top) The prediction of linear scaling of total reflection of noise $\Gamma_R(F_{a_0}^{-1})$ is tested. For each sample the total reflection noise data are plotted versus the measured $F_{a_0}^{-1}$. $\Gamma_R(F_{a_0}^{-1})$ is fitted to the experimental data (open symbols). (bottom) $\Gamma_R(\Omega)$ is plotted for values of S_n obtained by fitting $\Gamma_R(F_{a_0}^{-1})$ to the experimental data. The theoretical curves (solid lines) are compared to the measured spectra (open symbols).

L $[\mu m]$	S_n	S_i
1.43	0.688 ± 0.007	0.693 ± 0.008
2.3	0.631 ± 0.002	0.65 ± 0.02
4	0.525 ± 0.002	0.55 ± 0.01
5.5	0.51 ± 0.01	0.522 ± 0.006
7.2	0.488 ± 0.001	0.498 ± 0.008
8.2	0.538 ± 0.001	0.5386 ± 0.007
13.5	0.421 ± 0.002	0.428 ± 0.002
18	0.412 ± 0.001	0.414 ± 0.001

Table 2.2: Parameter S obtained from total reflection of intensity (S_i) and noise (S_n).

Furthermore, in order to compare the experimental results to the theory of section 2.2, and specifically eq. (2.26), for each sample the total reflection data are plotted versus $F_{a_0}^{-1}$, which is a measured quantity. The goal is to verify the predicted linear scaling of $\Gamma_R(F_{a_0}^{-1})$. In order to test the theory we modify eq. (2.26) to include the extrapolation lengths by replacing $\rho \equiv \frac{\ell}{L}$ with $S = (\ell + z_1)\,(L + z_1 + z_2)^{-1}$. The only fit parameter is S.

In fig. (2.8, upper panel), $\Gamma_R(F_{a_0}^{-1})$ is plotted for three representative samples along with the linear fits to the data. The difference between the previous approach illustrated in fig. (2.7) and the current one, shown in fig. (2.8), is that in the present case, for each sample the fit produces an estimate for S, and therefore ℓ. By contrast, in fig. (2.7) a single value for ℓ is obtained by fitting the data available for all the samples.

The linear scaling predicted by eq. (2.26) is apparent. Having checked the predicted linear scaling, we make use of the total reflection intensity data analysed in section 2.5 to quantitatively evaluate our results. By using the intensity data and eq. (2.28) we can independently deduce the parameter S for each sample. We indicate with S_i and S_n the parameter S as measured via intensity and noise measurements respectively. The comparison between S_i and S_n is summarized in table (2.2). The agreement is very good. In addition, the mean free path ℓ obtained in section 2.5 from the intensity data gives $\ell = (0.84 \pm 0.07)$ μm, in full agreement with the values for ℓ obtained via classical and quantum noise measurements.
Finally, to further inspect the agreement between the experimentally measured noise spectra and the theoretical results, the values for S_n are plugged in eq. (2.26). A comparison between the experimental total reflection spectra and $\Gamma_R(\Omega)$ is shown for three representative samples in fig. (2.8, lower panel). The agreement is very good.

2.8 Conclusions

We have derived a theory for the reflection of classical and shot noise from random media and tested it experimentally. It was shown a linear and quadratic scaling for the total reflection of shot ($F_{a_0} = 1$) and classical ($F_{a_0} \gg 1$) noise, respectively.

The scaling parameter is $s_p = \left(1 - \frac{\ell}{L}\right)$.
It was found that total reflection of shot and classical noise as function of the frequency Ω exhibits different properties. Shot noise has an higher reflection than classical noise and the transition from one regime to the other is very clear around 1 MHz. Furthermore it was shown that a linear behaviour gauges the transition from classical noise at low frequency ($\Omega < 1$ MHz) to shot noise at high frequency ($\Omega > 1$ MHz). This linear behaviour emerges when the noise data are plotted as function of $F_{a_0}^{-1}$.

CHAPTER 3

Weak localization of photon noise in random media

We present an experimental study of coherent backscattering (CBS) of photon noise from multiple scattering media. Using a pseudothermal light source we study the effect of weak localization on photon noise. In the noise spectrum we observe a continuous transition in the Fano factor enhancement from the shot noise regime to the wave fluctuations regime. These initial experiments on weakly scattering media demonstrate that sensitive noise measurements can be combined with the separation of path lengths present in coherent backscattering, opening up new opportunities for experiments on noise transport in the localization regime.

3.1 Introduction

In chapter 2 we investigated the total reflection of classical and quantum noise from TiO_2 random samples. However, those experiments did not allow to closely monitor the propagation of noise as function of the number of scattering events that light undergoes in the medium, nor did the experiments by Lodahl et al. [78], as they revolved around the total transmission of noise trough random media. Moreover, in both experiments the classical noise source was given by the low frequency noise of the Ti:Sapphire laser, which did not allow for fine tuning of the noise intensity and spectral range of classical and shot noise. The goal of the experiments presented in this chapter is to extend the study of photon noise by devising a method to simultaneously follow the transport of noise as function of the order of scattering and to control the contribution of the classical noise.

A method to separate multiple scattering paths of different length is coherent backscattering (CBS). As explained in the chapter 1, CBS results from an interference effect between reciprocal paths in a random medium, and manifests itself as a twofold enhancement of the light intensity in the backscattering direction with respect to the diffuse background. Measurements of CBS have turned over the years from a striking evidence of weak localization of light to a tool for investigating the scattering properties of many different media [86–88]. The strong Anderson localization transition has received much attention since it was first proposed in 1958 [89], nevertheless it remains an elusive phenomenon [90, 91] and noise measurements could provide alternative means to investigate it. Furthermore, the impact of Anderson localization on non classical properties of light is yet an open question [92].

This chapter is structured as follows: in section 3.2 we describe the main principles that govern the statistics of light sources, in section 3.3 we calculate the fluctuations induced by a diffuser on a coherent beam and explain the analogy between a diffuser and a thermal source. Subsequently, in section 3.4 the intensity spectrum for a pseudothermal source is derived. In section 3.5 the experiments that lead to the weak localization of photon noise are described and finally, in section 3.6, we analyze and discuss the results.

3.2 Statistics of the light radiation

The statistical properties of the light can be assessed by using Mandel's formula. Mandel's formula is very useful to calculate the photocount distribution P_M of the photons emitted by a source and is given by [38, 93]

$$P_M(n,t,T) = \int_0^\infty \frac{[\alpha W(t,T)]^n}{n!} \exp\left[-\alpha W(t,T)\right] P(W) dW, \tag{3.1}$$

with

$$W(t,T) = \int_t^{t+T} I^{'}(t^\prime)dt^\prime, \tag{3.2}$$

where n denotes the number of photons, $I^{'}$ the instantaneous intensity, α the quantum efficiency of the detector. The measurement is carried out in the time interval $[t, t+T]$. With $P(W)$ is indicated the intensity distribution of the ensemble. One could interpret formula (3.1) in the following way: if we consider one single realization for the sequence of photons measured within time T we would achieve a Poissonian photocount statistics. However, in general, different sequences would yield different results because $W(t,T)$ is not a deterministic variable but a random one. Therefore what is significant is the photocount distribution calculated over an ensemble of different realizations of the photon number sequences. Eq. (3.1) expresses then the Poissonian distribution weighted by the intensity distribution $P(W)$ of the ensemble.

In a true thermal source, like a discharge lamp or a light bulb, the radiating system is externally excited and subsequently generates light by means of spontaneous emission. Hence, all the elementary sources (atoms, molecules) emit light independently from one another.

A thermal source is characterized by a Rayleigh distribution for the intensity $P_R(W)$ whereas, the photocount distribution P_M becomes of type Bose-Einstein, indicated with $P_{BE}(n)$, and we have the expressions

$$P_R\left(W\right) = \frac{1}{\overline{\overline{W}}} \exp\left(-\frac{W}{\overline{\overline{W}}}\right) \tag{3.3}$$

and

$$P_M = P_{BE}(n) = \frac{1}{\overline{n}} \left(\frac{\overline{n}}{\overline{n}+1}\right)^n , \tag{3.4}$$

where with $\overline{n} \equiv \alpha\overline{W(t,T)}$ we indicate the mean number of photocounts, also known as the occupation number.

By contrast, laser light is produced by stimulated emission, whereby all the elementary sources radiate in unison and the intensity distribution $P_L(W)$ is given by

$$P_L(W) = \delta(\overline{W} - W), \tag{3.5}$$

while the photocount distribution P_M is Poissonian, indicated with $P_P(n)$, and results in

$$P_M = P_P(n) = \frac{\overline{n}^n \exp\left(-\overline{n}\right)}{n!}. \tag{3.6}$$

The variance of $P_P(n)$ has the expression

$$\overline{(\Delta n)^2_P} = \overline{n}. \tag{3.7}$$

Eqs. (3.4) and (3.6) can be obtained by inserting eqs. (3.3) and (3.5) in Mandel's formula respectively, provided that the integration time T is much smaller than the coherence time τ_c of the light. Eqs. (3.5) and (3.6) show that, in spite of the fact that all the different members of the intensity ensemble relative to W are exactly the same, we end up with a probability distribution for the photocounts. This situation highlights the particle nature of light: even the most stable source has intensity fluctuations. These fluctuations are proportional to the mean number of the emitted photons.

For a true thermal source, like a blackbody, Planck's law predicts an average photon number given by [93]

$$\overline{n} = \frac{1}{\exp\left(\frac{h\omega}{kT_K}\right) - 1}, \tag{3.8}$$

with T_K being the temperature in Kelvin, h Planck's constant, K Boltzmann's constant and ω the frequency of the light of concern. Eq. (3.8) shows that, at optical frequencies, a temperature above the one of the surface of the sun (6000 K) is needed to achieve an occupation number bigger than one. The variance of the Bose-Einstein distribution is

$$\overline{(\Delta n)^2_{BE}} = \overline{n} + \overline{n}^2. \tag{3.9}$$

An occupation number much smaller than one, like the one exhibited by true thermal sources in experimentally feasible configurations, depresses the classical fluctuations that are given by the $\overline{n}^2$ term in eq. (3.9). An additional complication carried by thermal sources is that their signature, a Bose-Einstein probability distribution, shows up only when the measurements are performed within the coherence time τ_c of the source, as can be proved by using Mandel's formula. Typical thermal sources have coherence times of the order of $10^{-10}s$. Performing measurements within this time interval is extremely demanding from an experimental perspective. Measuring over many coherence times of the sources implies averaging out the interesting fluctuations that give rise to the quadratic term in eq. (3.9); in this case the measured photocount distribution of thermal light becomes indistinguishable from a Poissonian one.

If we want to investigate and use the classical properties of light it is then crucial to find a way to optimize the quadratic term of expression (3.9). Pseudothermal light is a solution to the complications displayed by true thermal sources as it mimics the same physics as the one responsible for thermal light but on a experimentally accessible scale. As it is explained in the next section pseudothermal light can be generated by illuminating a rotating ground glass diffuser with laser light. The analogy between the intensity statistics of a thermal source and the one generated by a rotating diffuser is at the base of the name pseudothermal source.

3.3 Diffuser as a pseudothermal source

In this section we calculate the intensity fluctuations and the intensity probability distribution of a thermal source, composed by an ensemble of radiating elements (atoms, molecules). Furthermore, we show the analogy with the statistical properties of the radiation produced by a ground glass diffuser illuminated by coherent light.

A ground glass diffuser, see fig. (3.1), is schematized as a collection of random glass defects that we call microareas. An incoming laser radiation that impinges on the diffuser is randomly scattered by the microareas. The diffuser rotates, therefore the incoming beam illuminates different microareas, that in turn act like independent sources. By independent we mean that there is no phase relationship among fields produced by different microareas. This is the key property that makes a ground glass diffuser a pseudothermal source: the microareas mimic the behaviour of the emitting atoms of molecules in a true thermal source.

To calculate the fluctuations induced by a large number of radiating scatterers we follow the approach presented in [22]. The scatterers in this model are the microareas of the diffuser.

Let us consider the field produced by a large number of scatterers ν. The complex amplitude of the resulting field is given by

$$E(t) = E_0 \exp(-i\omega t) \sum_{j=1}^{\nu} \exp[i\phi_j], \qquad (3.10)$$

cases	$\overline{I^2}$
$i=j=k=l$	$\left(\frac{\varepsilon_0 c}{2}\right)^2 E_0^4\nu$
$i=j$ and $k=l$ with $i\neq k$	$\left(\frac{\varepsilon_0 c}{2}\right)^2 E_0^4\nu\left(\nu-1\right)$
$i=l$ and $j=k$ with $i\neq j$	$\left(\frac{\varepsilon_0 c}{2}\right)^2 E_0^4\nu\left(\nu-1\right)$
remaining cases	0

Table 3.1: Contributions to $\overline{I^2}$

with ϕ_j being the phase of the $j-th$ field and E_0 and ω the amplitude and frequency of each radiating field, respectively. Our interest lies in calculating the intensity fluctuations, therefore we have to compute the quantity

$$\Delta I^2 = \overline{I^2} - \overline{I}^2, \tag{3.11}$$

where the overbar denotes ensemble averaging. To calculate ΔI^2 we proceed by separately calculating $\overline{I}$ and $\overline{I^2}$. The cycle averaged intensity I is given by

$$I \equiv \frac{\varepsilon_0 c}{T}\int_0^T Re\{E(t)\}Re\{E(t)^*\}dt = \frac{\varepsilon_0 c}{2}E_0^2\sum_{ij}^{\nu}\exp i\left(\phi_i-\phi_j\right), \tag{3.12}$$

with $T=\frac{2\pi}{\omega}$, c the speed of light, ε_0 the dielectric constant and where we have used eq. (3.10).

In order to calculate $\overline{I}$ we recall that the phases ϕ_i are random variables with uniform probability distribution that assumes values in $[0-2\pi]$. The only cases in which $\overline{I}\neq 0$ are then those for which $\phi_i=\phi_j$. In all other cases we have $\overline{\exp i\left(\phi_i-\phi_j\right)}=0$. Therefore we get

$$\overline{I} = \frac{\varepsilon_0 c}{2}E_0^2\nu. \tag{3.13}$$

Next we calculate $\overline{I^2}$. By using eq. (3.12) we obtain

$$I^2 = \left(\frac{\varepsilon_0 c}{2}\right)^2 E_0^4\sum_{ijkl}\exp i\left(\phi_i-\phi_j+\phi_k-\phi_l\right). \tag{3.14}$$

To compute $\overline{I^2}$ we use the same arguments as above and we end up with the situation presented in table (3.1). By adding all of the contributions in table (3.1) we have

$$\overline{I^2} = \left(\frac{\varepsilon_0 c}{2}\right)^2 E_0^4\left(\nu+2\nu\left(\nu-1\right)\right). \tag{3.15}$$

We now have everything we need to calculate ΔI^2. By means of eqs. (3.13) and (3.15) we obtain

$$\Delta I^2 = \overline{I^2}-\overline{I}^2 = \left(\frac{\varepsilon_0 c}{2}\right)^2 E_0^4\left[\left(\nu+2\nu\left(\nu-1\right)\right)-\nu^2\right] = \left(\frac{\varepsilon_0 c}{2}\right)^2 E_0^4\left[\nu^2-\nu\right]. \tag{3.16}$$

If the number of radiating scatterers is large ($\nu \gg 1$) ΔI^2 becomes

$$\Delta I^2 = \left(\frac{\varepsilon_0 c}{2}\right)^2 E_0^4 \nu^2 = \overline{I}^2. \tag{3.17}$$

The intensity fluctuations ΔI^2 scale quadratically with the average intensity.

Having calculated ΔI^2 we can also recover the full probability distribution $P(I)$. A way to calculate the probability distribution is to compute its higher order moments $\overline{I^n}$. In general, computing the higher moments is a difficult task but, if the number of radiating scatterers ν is large the following relationship holds

$$\overline{I^n} = n!\overline{I}^n. \tag{3.18}$$

Eq. (3.18) can be deduced, following [42], by writing down the expression for $\overline{I^n}$, given by

$$\overline{I^n} = \sum_{\nu_1 ... \nu_n, \beta_1 ... \beta_n} \overline{E_{\nu_1} ... E_{\nu_n} E_{\beta_1} ... E_{\beta_n}}. \tag{3.19}$$

If there is a random phase relationship between the fields, e.g. the fields are independent from one another in accordance with the reasoning that leads to table (3.1), the only contributions different from zero are of the type

$$\overline{E_\nu E_\beta} = \delta_{\nu\beta}\overline{I}. \tag{3.20}$$

Since there are $n!$ ways to combine the fields in eq. (3.19) so that eq. (3.20) holds true, eq. (3.18) is recovered for the moments.
From the expression for the moments we can extract the total probability distribution $P_R\left(I\right)$, given by

$$P_R\left(I\right) = \frac{1}{\overline{\overline{I}}} \exp\left(-\frac{I}{\overline{\overline{I}}}\right). \tag{3.21}$$

Eq. (3.21) represents the Rayleigh distribution, which is a milestone in statistical optics. The Rayleigh distribution occurs often in physics and is a consequence of the central limit theorem that applies because of the independency of the sources.

3.4 Intensity spectrum of a pseudothermal source

In this section we follow the theory presented in [94] to calculate the noise power spectrum $S(\Omega)$ generated by a rotating diffuser. The schematics is presented in fig. (3.1).

The formula for the power spectrum is given by

$$S(\Omega) = \int_{-\infty}^{+\infty} \left\langle \hat{j}(t)\hat{j}(t+\tau) \right\rangle \exp\left(-i\Omega\tau\right) d\tau, \tag{3.22}$$

where Ω denotes the noise frequency, $\hat{j}(t)$ the photocurrent operator and with $\langle\rangle$ we indicate quantum averaging.

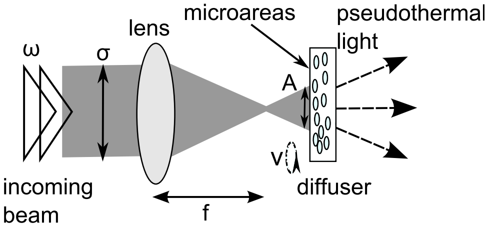

Figure 3.1: Setup consisting of a lens and a diffuser used to generate pseudothermal light. A laser beam of frequency ω and diameter σ is focussed by a lens of focal lens f and impinges on a ground glass diffuser rotating at speed v. With A is indicated the cross section of the beam on the diffuser. The ground glass diffuser is modelled as a collection of random microareas. The rotation of the microareas gives rise to pseudothermal light.

Our goal is to evaluate the term $\left\langle \hat{j}(t)\hat{j}(t+\tau)\right\rangle$ and Fourier transform it according to eq. (3.22). In order to fully account for the wave and particle nature of light we resort to the quantum derivation outlined in [94]. We have

$$\left\langle \hat{I}(t)\hat{I}(t+\tau)\right\rangle = \left\langle : \hat{I}(t)\hat{I}(t+\tau) : \right\rangle - \hbar 2\epsilon_0 i\delta'(\tau)\left\langle \hat{E}^{(-)}(t)\hat{E}^{(+)}(t+\tau)\right\rangle \tag{3.23}$$

where $\hat{I}(t)$ denotes the intensity operator and the :: notation indicates normal ordering of the field operators $\hat{E}^{(-)}(t)$ and $\hat{E}^{(+)}$, that are given respectively by

$$\hat{E}^{(-)}(t) = \left(\frac{1}{2\pi}\right)^2 \int d\omega \left(\frac{\hbar\omega}{2\epsilon_0}\right)^{1/2} \hat{a}^\dagger(\omega)e^{i\omega t} \tag{3.24}$$

and

$$\hat{E}^{(+)}(t) = \left(\frac{1}{2\pi}\right)^2 \int d\omega \left(\frac{\hbar\omega}{2\epsilon_0}\right)^{1/2} \hat{a}(\omega)e^{-i\omega t}. \tag{3.25}$$

In eqs. (3.24) and (3.25) $\hbar = \frac{h}{2\pi}$ with h being Planck's constant and ϵ_0 is the dielectric constant. By using the relationship

$$g^{(2)}(\tau) = \frac{\left\langle : \hat{I}(t)\hat{I}(t+\tau) : \right\rangle}{\left\langle \hat{I}(t)\right\rangle \left\langle \hat{I}(t+\tau)\right\rangle}, \tag{3.26}$$

where $g^{(2)}(\tau)$ denotes the second order correlation function, we can rewrite eq. (3.23) as follows

$$\left\langle \hat{I}(t)\hat{I}(t+\tau)\right\rangle = g^{(2)}(\tau)\left\langle \hat{I}(t)\right\rangle \left\langle \hat{I}(t+\tau)\right\rangle - \hbar 2\epsilon_0 i\delta'(\tau)\left\langle \hat{E}^{(-)}(t)\hat{E}^{(+)}(t+\tau)\right\rangle . \tag{3.27}$$

The term $\left\langle \hat{E}^{(-)}(t)\hat{E}^{(+)}(t+\tau)\right\rangle$ is related to the first order correlation function $g^{(1)}(\tau)$ and we have

$$\left\langle \hat{E}^{(-)}(t)\hat{E}^{(+)}(t+\tau)\right\rangle = \frac{g^{(1)}(\tau)\left\langle \hat{I}(t)\right\rangle}{2\epsilon_0} = \left(\frac{e}{\hbar\omega}\right)\left(\frac{1}{2\epsilon_0}\right)\left\langle \hat{j}(t)\right\rangle g^{(1)}(\tau). \tag{3.28}$$

The relationship between the intensity $\hat{I}(t)$ and the photocurrent $\langle\hat{j}(t)\rangle$ is given by

$$\left\langle \hat{j}(t) \right\rangle = \frac{e}{\hbar\omega} \left\langle \hat{I}(t) \right\rangle . \tag{3.29}$$

Therefore, by exploiting eq. (3.29) we have

$$\left\langle \hat{j}(t)\hat{j}(t+\tau) \right\rangle = g^{(2)}(\tau) \left\langle \hat{j}(t) \right\rangle \left\langle \hat{j}(t+\tau) \right\rangle - \left(\frac{e}{\hbar\omega} \right) \hbar i \delta'(\tau) \left\langle \hat{j}(t) \right\rangle g^{(1)}(\tau). \tag{3.30}$$

For chaotic light we can use the Siegert relationship, [95]

$$g^{(2)}(\tau) = 1 + \left| g^{(1)}(\tau) \right|^2 . \tag{3.31}$$

What we need to calculate now is $g^{(1)}(\tau)$. Up to now we have not made use of the properties of the rotating diffuser that generates pseudothermal light. We use the result provided by [96] where $g^{(1)}(\tau)$ is calculated for a rotating ground glass diffuser and that yields

$$g^{(1)}(\tau) = \frac{2\pi\sigma^2}{A} \nu \overline{s^2} \exp\left(i\omega\tau - \frac{v^2\tau^2}{2} \left(\frac{k^2\sigma^2}{f^2} + \frac{1}{4\sigma^2} \right) \right) . \tag{3.32}$$

In eq. (3.32), and with reference to fig. (3.1), σ^2 is the cross section of the incident beam, ν is the number of independent microareas we divide the diffuser into, A is the illuminated area on the surface of the diffuser and s is a term that takes into account diffraction from the microareas. By looking at eq. (3.32) we define the coherence time τ_c of the pseudothermal source as

$$\frac{1}{\tau_c^2} \equiv \frac{v^2}{2} \left(\frac{k^2\sigma^2}{f^2} + \frac{1}{4\sigma^2} \right) . \tag{3.33}$$

It is instructive to consider eq. (3.33) for a series of realistic experimental conditions. As it is clear from fig. (3.2) to introduce excess fluctuations in the MHz regime we need to spin the diffuser with a linear velocity of a few ms^{-1} and a focal length of $2 - 3$ cm.

We now have all the ingredients to calculate eq. (3.22). On inserting eq. (3.30) in eq. (3.22), and making use of eq. (3.32), we obtain

$$\begin{aligned} S(\Omega) &= \int_{-\infty}^{+\infty} \left\langle \hat{j}(t)\hat{j}(t+\tau) \right\rangle \exp(-i\Omega\tau) d\tau \\ &= \left\langle \hat{j}(t) \right\rangle^2 \delta(\Omega) \\ &+ \left\langle \hat{j}(t) \right\rangle^2 \frac{\tau_c}{2} \exp\left\{ -\frac{\Omega^2\tau_c^2}{8} \right\} \\ &+ \left\langle \hat{j}(t) \right\rangle \left(\frac{\omega - \Omega}{\omega} \right) \zeta, \end{aligned} \tag{3.34}$$

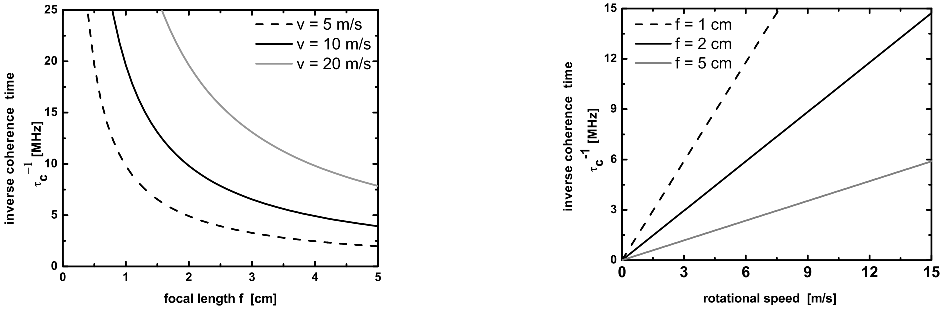

Figure 3.2: (left) Calculation of the inverse coherence time τ_c^{-1} as function of the focal length of the lens for three different rotational speed of the ground glass diffuser. (right) Calculation of the inverse coherence time τ_c^{-1} as function of the rotational speed of the ground glass diffuser for three different focal lengths.

with

$$\zeta = e\frac{2\pi\sigma^2\nu\overline{s^2}}{A}. \tag{3.35}$$

The first part of eq. (3.34) contains a delta function that represents the dc component of the spectrum. The second part of eq. (3.34) contains a frequency-dependent gaussian spectrum, whose amplitude scales quadratically with the intensity. This term is the classical noise contribution. Finally the third part of eq. (3.34) displays a flat, frequency independent term because, given the experimental conditions, the frequencies ratio yields one. This term is the shot noise contribution. The shot noise term is a consequence of the quantum nature of light, of its intrinsic granular nature.

The noise barrier in any optical system is given by the shot noise. A shot noise limited source, like some lasers, is thus the quietest possible source. It is feasible to beat this limit only by resorting to quantum optics tricks, like for example squeezing. Also in that case though, we are not eliminating noise, but only transferring noise from one quadrature to the other, so that one quadrature displays shot and excess noise while the other one exhibits a noise contribution which is below the shot noise level.

In the next section we will describe experiments that make use of the system composed by two lenses and a diffuser to generate pseudothermal light.

3.5 Weak localization of photon noise

Here, we present the first experimental investigation of weak localization of photon shot and pseudothermal noise from scattering media. The basic setup to induce and measure photon noise is depicted in fig. (3.3). It consists of a Ti:Sapphire laser (Spectra Physics-Tsunami) and a set of two lenses to focus light on the diffuser and collimate the exit beam respectively. The collimated exit beam is collected by an APD detector and the noise content of the signal is analyzed by the electronic

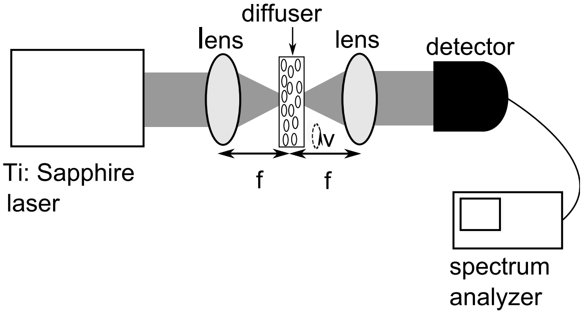

Figure 3.3: Basic setup to measure photon noise. A Ti:Sapphire laser is a photon shot noise source. The rotating ground glass diffuser produces pseudothermal light and the two lenses generate a collimated beam. The spectrum analyzer investigates the noise content of the signal.

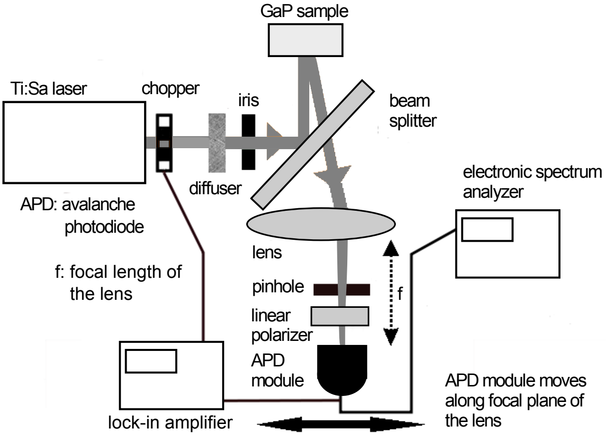

Figure 3.4: Schematic overview of the experimental setup for measurement of noise and intensity coherent backscattering.

spectrum analyzer. By tuning the angular speed of the diffuser it is possible to push the transition frequency up to the MHz regime. We integrated these components into a coherent backscattering setup.

Coherent backscattering of both intensity and noise is measured in a beamsplitter configuration [97], as outlined in fig. (3.4). We used the 1.6 W output of a shot noise limited Ti:Sapphire oscillator operating in cw mode and at a wavelength of 780 nm. Light scattered from the sample was collected by a lens (f = 8 cm) and detected by an avalanche photodiode (APD) module (Hamamatsu C4777) that moves along the focal plane of the lens. An electronic spectrum analyzer (Agilent) was used to measure the noise power spectrum. The angular resolution amounts to 1.2 mrad and is determined by a 100 μm pinhole placed in front of the detector.

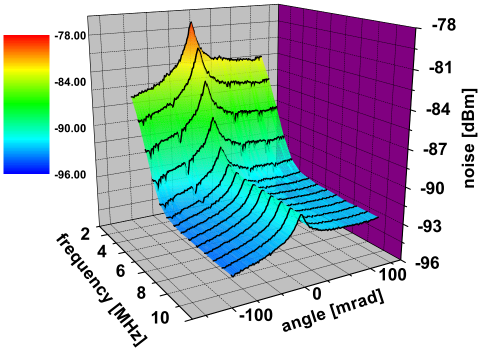

Figure 3.5: Noise spectrum of light scattered from a gallium phosphide sample as function of backscattering angle and frequency. The CBS noise cones are clearly visible over the entire frequency range.

The sample was slightly tilted to prevent light which was specularly reflected from the sample to be detected. Speckle averaging was obtained by rotating the sample around its azimuthal axis using a spinning motor. We performed detection in the polarization conserving channel. Lock-in detection minimizes the influence of stray light. Pseudothermal light was generated by focusing the laser beam onto a rotating diffuser [98, 99]. By spinning the diffuser it was possible to introduce excess noise up to the MHz regime.

Our sample consists of a slab of porous GaP fabricated via an electrochemical etching technique, and showing negligible absorption at 780 nm [100]. The sample has thickness $L \simeq 70\ \mu$m and $k_0 \simeq 17.7$, where with k_0 we indicate the incoming wavevector outside the medium.

Noise spectra were acquired with a resolution bandwidth (RBW) of 30 kHz and a video bandwidth (VBW) of 10 kHz over a frequency segment that spans 8.85 MHz, from 0.15 MHz to 10 MHz . Each point in the noise traces has been obtained by computing the average of 50 consecutive points in the spectrum. Intensity and noise cones were acquired in the polarization conserving channel and normalized to the intensity and noise power measured in the polarization nonconserving channel. The cones were further normalized to the value assumed on the left most angle. Noise spectra are shown in fig. (3.5) as function of angle and frequency. Cross sections at different frequencies are shown in fig. (3.6), along with the intensity CBS cone data and its square. The data highlight how the CBS shape changes from the shot noise regime at high frequencies to the pseudothermal noise regime at low frequencies. Furthermore, the comparison to the intensity data shows how the shot noise cone, obtained from the high frequency data, follows closely the intensity cone whereas the intensity CBS cone squared is an upper bound for the pseudothermal cones, obtained from the low frequency data. The enhancement produced by pseudothermal light exceeds the ordinary maximum value of 2 obtainable for the intensity cone.

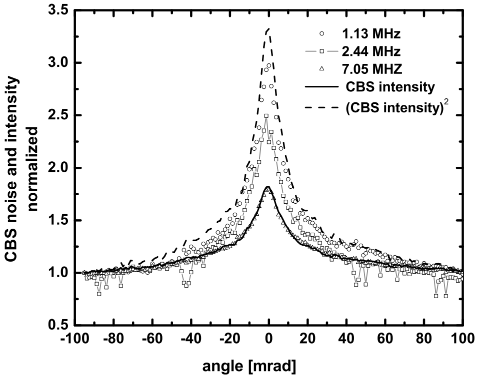

Figure 3.6: Comparison between the measured CBS intensity and CBS noise signals. At high frequency the shot noise cones match the intensity cone. As the noise frequency is lowered the noise cones exceed the intensity cone and approach the maximum value given by the squared intensity.

3.6 Analysis

We start modelling our experiment by using eq. (3.34). The first term indicates the dc intensity and is filtered out in our experiments, therefore it will be discarded from the analisys. The second term in eq. (3.34) represents the wave fluctuations and quantifies the excess noise, while the third term accounts for the shot noise or particle fluctuations.

The measured photocurrent is related to the light intensity by $\langle j \rangle = \gamma \langle I \rangle$ where $\langle I \rangle$ is the intensity and γ a constant proportional to the responsivity of the APD detector. We can explicitly introduce the sample parameters by writing

$$\overline{\langle I_{ab} \rangle} = \overline{R}_{ab} \langle I_a \rangle , \tag{3.36}$$

$$\overline{\langle I_{ab} \rangle^2} = \overline{R^2}_{ab} \langle I_a \rangle^2 , \tag{3.37}$$

where $\overline{R}_{ab}$ indicates the classical reflection coefficient from incoming channel a to outgoing channel b, averaged over different realizations of the disorder (ensemble average). On inserting eqs. (3.36) and (3.37) in eq. (3.34) and performing ensemble average we obtain

$$\overline{\langle S(\Omega)_{ab} \rangle} = \phi \overline{R}_{ab} \langle I_a \rangle + \gamma^2 \overline{R^2}_{ab} \langle I_a \rangle^2 \left(\frac{\tau_c}{2} \right) \exp \left(- \frac{\Omega^2 \tau_c^2}{8} \right) , \tag{3.38}$$

where we have highlighted the dependence of the photocurrent spectrum on the outgoing channel b, and $\phi = \gamma \zeta$. The frequency-dependent noise spectrum can be used to calculate a frequency-dependent Fano factor F defined as the ratio of the photocurrent fluctuation to the average photocurrent,

$$F(\Omega)_{ab} \equiv \frac{\overline{\langle S(\Omega)_{ab} \rangle}}{\phi \overline{R}_{ab} \langle I_a \rangle} . \tag{3.39}$$

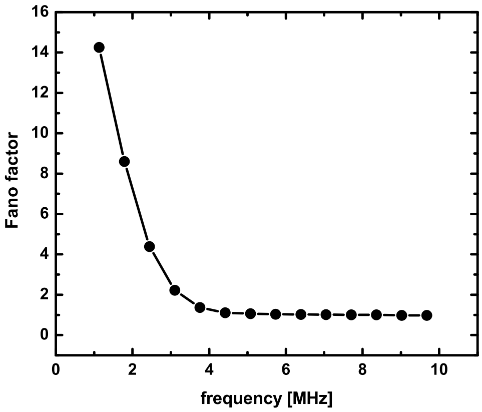

Figure 3.7: Observed Fano factor as function of frequency obtained from the noise trace collected exactly at backscattering. A gallium phosphide sample with $k_0\ell \simeq 17.7$ has been used. The Fano factor has been extracted by dividing the full noise spectrum by the constant value obtained by fitting the high frequency noise data to a line. The solid line is a guide to the eye.

Fig. (3.7) shows the Fano factor as a function of noise frequency. In order to analyze the effect of coherent backscattering on the Fano factor, we analyze the Fano factor as a function of scattering angle and frequency. The instrumental response is divided out by normalizing both the average intensity and the noise spectra to those acquired in the polarization nonconserving channel, in which the CBS effect is absent. We define a Fano factor CBS enhancement $\eta_{ab}(\Omega)$ as the ratio of the normalized noise spectra to the normalized intensity

$$\eta_{ab}(\Omega) \equiv \frac{\overline{\langle S(\Omega)^{pc}_{ab} \rangle}}{\overline{\langle S(\Omega)^{pnc}_{ab} \rangle}} \left(\frac{I^{pc}_{ab}}{I^{pnc}_{ab}} \right)^{-1}, \tag{3.40}$$

where the subscript pc and pnc stand for polarization conserving and polarization nonconserving, respectively. By expanding eq. (3.40) we obtain

$$\eta_{ab}(\Omega) = \frac{\phi + \overline{R^2_{ab}}^{pc} \left(\overline{R}^{pc}_{ab} \right)^{-1} \langle I_a \rangle \gamma^2 \left(\frac{\tau_c}{2} \right) \exp\left(-\frac{\Omega^2 \tau_c^2}{8} \right)}{\phi + \overline{R^2_{ab}}^{pnc} \left(\overline{R}^{pnc}_{ab} \right)^{-1} \langle I_a \rangle \gamma^2 \left(\frac{\tau_c}{2} \right) \exp\left(-\frac{\Omega^2 \tau_c^2}{8} \right)}. \tag{3.41}$$

A 3D plot of $\eta_{ab}(\Omega)$ is shown in fig. (3.8). Cross sections of the 3D plot are produced in fig. (3.10) for three representative noise frequencies as function of the scattering angle. The Fano factor enhancement $\eta_{ab}(\Omega)$ is 1 away from the CBS cone, as here the polarization conserving and nonconserving channels yield the same noise and intensity.

It is interesting to consider the situation on backscattering, by calculating $\eta_{aa}(\Omega)$. In order to do that we need to evaluate $\overline{R^2_{aa}}^{pc} \left(\overline{R}^{pc}_{aa} \right)^{-1}$ and $\overline{R^2_{aa}}^{pnc} \left(\overline{R}^{pnc}_{aa} \right)^{-1}$.

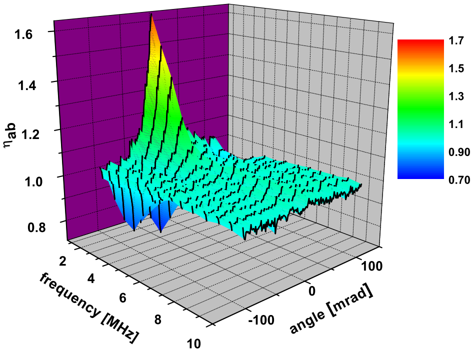

Figure 3.8: 3D plot for the measured Fano factor CBS enhancement $\eta_{ab}(\Omega)$ as function of frequency and angle. A gallium phosphide sample with $k_0\ell \simeq 17.7$ has been used. The plotted data have been obtained from the raw data by binning 50 consecutive data points along the frequency axis. $\eta_{ab}(\Omega)$ varies from 1 at high frequencies in the shot noise regime to a maximum value which is always lower than the intensity CBS enhancement. Values of $\eta_{ab}(\Omega)$ below 1 are due to spurious fluctuations.

The coherent backscattering effect due to interference is present in the polarization conserving channel [1]. Since in the polarization nonconserving case the coherent backscattering effect is absent we assume

$$\frac{\overline{R^2_{aa}}^{pnc}}{\overline{R_{aa}}^{pnc}} = \frac{\overline{R^2_{ab}}}{\overline{R_{ab}}}. \tag{3.42}$$

From now on we drop the subscripts pc and pnc, as the term R_{aa} will always be referred to the polarization conserving case. In order to assess the effect of mesoscopic interference in the coherent backscattering of noise, we consider the first order mesoscopic contribution in the reflectivity as obtained in [102]. By exploiting eq. (15) in [102] we have

$$\overline{R^2_{ab}} = \overline{R}^2_{ab}\left(2 - \frac{2}{N(1-\frac{\ell}{L})}\right), \tag{3.43}$$

and

$$\overline{R^2_{aa}} = \overline{R}^2_{aa}\left(2 - \frac{3}{N(1-\frac{\ell}{L})}\right). \tag{3.44}$$

As we have seen in chapter 2, the total conductance g, defined in transmission, is given by

$$g = \frac{N\ell}{L}. \tag{3.45}$$

---

[1] While the polarization conserving channel contains the interference effect that gives rise to the coherent backscattering phenomenon, it does not reject single scattering events. Single scattering events do not have a reverse path and contribute to lowering the enhancement factor [101].

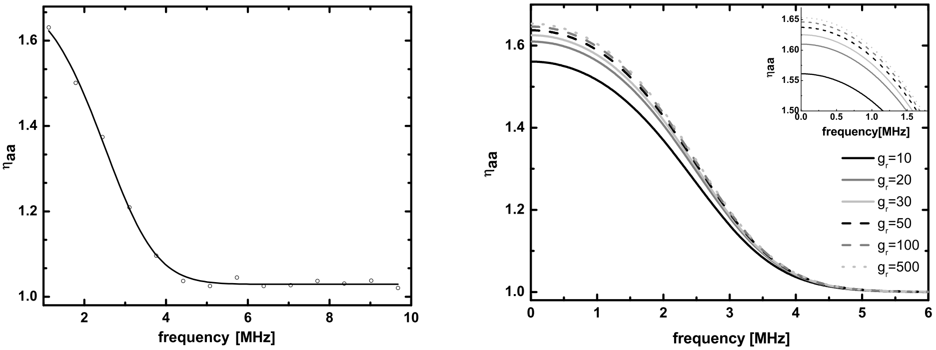

Figure 3.9: (left) Observed noise CBS enhancement factor on backscattering η_{aa} as function of frequency. The enhancement factor $\eta_{aa}(\Omega)$ has been obtained by taking the maximum of $\eta_{ab}(\Omega)$ at each frequency. The solid line is a fit of the theoretical line shape for η_{aa} to the data. (right) Calculations that illustrate the effect of the conductance g_r on the Fano factor CBS enhancement on backscattering $\eta_{aa}\,(\Omega)$. Low g_r values induce stronger variations, especially at low frequencies. As g_r increases η_{aa} quickly converges towards the limit function in eq. (3.50), and deviations caused by high g_r values become difficult to be discerned. The inset highlights the different values reached by η_{aa} at $\Omega = 0$. The parameters ϕ, β and τ_c are fixed according to the values obtained in experiments.

In reflection, following the same procedure as the one adopted for g we define

$$g_r \equiv \sum_{a,b} \overline{R}_{ab}, \tag{3.46}$$

and, using the fact that $\overline{R}_{ab} = \left(1 - \frac{\ell}{L}\right)$ we find

$$g_r = N\left(1 - \frac{\ell}{L}\right). \tag{3.47}$$

Formulas (3.43) and (3.44) express the fact that when g_r^{-1} contributions are negligible the reflected intensity follows a Rayleigh distribution. Deviations from Rayleigh statistics arise when interferences effect between multiple scattering paths start to play a role.

By using eqs. (3.41), (3.43) and (3.44) we obtain the following expression for the Fano factor enhancement on backscattering

$$\eta_{aa}(\Omega) = \frac{\phi + \overline{R}_{aa}\left(2 - \frac{3}{g_r}\right)\langle I_a\rangle\,\gamma^2\left(\frac{\tau_c}{2}\right)\exp\left(-\frac{\Omega^2\tau_c^2}{8}\right)}{\phi + \overline{R}_{ab}\left(2 - \frac{2}{g_r}\right)\langle I_a\rangle\,\gamma^2\left(\frac{\tau_c}{2}\right)\exp\left(-\frac{\Omega^2\tau_c^2}{8}\right)}. \tag{3.48}$$

According to random matrix theory, $\overline{R}_{aa} = 2\overline{R}_{ab}$. To take into account a real experimental situation, where the enhancement on backscattering is usually lower

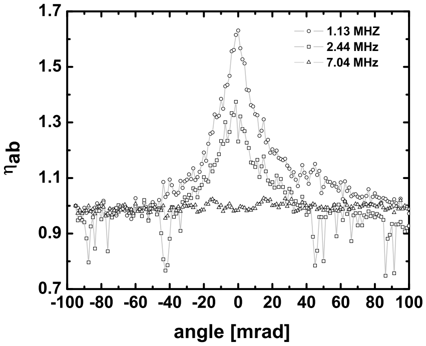

Figure 3.10: Noise CBS enhancement factor η_{ab} as function of the scattering angle around the backscattering direction at three different frequencies.

than 2, we will assume $\overline{R}_{aa} = (2-\beta)\,\overline{R}_{ab}$. After rearranging eq. (3.48) we find

$$\eta_{aa}\left(\Omega\right) = 1 + \frac{\left[2\left(1-\beta\right)\left(1-g_r^{-1}\right) - \left(2-\beta\right)g_r^{-1}\right]\left(\frac{\tau_c}{2}\right)\exp\left(-\frac{\Omega^2\tau_c^2}{8}\right)}{\psi + 2\left(1-g_r^{-1}\right)\left(\frac{\tau_c}{2}\right)\exp\left(-\frac{\Omega^2\tau_c^2}{8}\right)}, \tag{3.49}$$

with $\psi = \phi\left(\left\langle I_a\right\rangle \overline{R}_{ab}\gamma^2\right)^{-1}$. It is evident the sensitivity of η_{aa} to a broad range of g_r values. In our case, being the magnitude of g_r^{-1} negligible, we can simplify eq. (3.49) and obtain

$$\eta_{aa}(\Omega)_{g_r^{-1}\longrightarrow 0} = 1 + \frac{2\left(1-\beta\right)\left(\frac{\tau_c}{2}\right)\exp\left(-\frac{\Omega^2\tau_c^2}{8}\right)}{\psi + 2\left(\frac{\tau_c}{2}\right)\exp\left(-\frac{\Omega^2\tau_c^2}{8}\right)}. \tag{3.50}$$

In fig. (3.9, left panel), we show the measured Fano factor CBS enhancement on backscattering η_{aa} in our experimental configuration as well as, in fig. (3.9, right panel), the calculated effect of a selection of values for the conductance g_r on η_{aa}. The factor $\eta_{aa}\left(\Omega\right)$ is plotted as function of noise frequency and is fitted by using eq. (3.50). A good agreement is recovered.

The enhancement η_{aa} depends on the balance of quantum and classical noise, respectively given by ψ and the exponential term in the denominator of eq. (3.50). The behaviour of η_{aa} at low and high frequency, in the classical and shot noise regimes, is given respectively by

$$\eta_{aa}(\Omega)_{\Omega\longrightarrow 0} = 1 + \frac{2(1-\beta)\frac{\tau_c}{2}}{2\frac{\tau_c}{2}+\psi} \tag{3.51}$$

and

$$\eta_{aa}(\Omega)_{\Omega\longrightarrow\infty} = 1. \tag{3.52}$$

In the low-frequency limit, $\eta_{aa}(\Omega)$ approaches the coherent backscattering enhancement for the intensity, $2-\beta$. The Fano factor at high frequencies, i.e. for the coherent state, is not modified by coherent backscattering.

In general, $\eta_{aa}(\Omega)$ contains both the shot noise and the pseudothermal contributions, as shown in eq. (3.50), with the frequency Ω gauging the two regimes as highlighted by eqs. (3.51) and (3.52).

In fig. (3.10) $\eta_{ab}(\Omega)$, the Fano factor CBS enhancement of the outgoing radiation, is plotted as function of the backscattering angle. The factor $\eta_{ab}(\Omega)$ displays no angular dependence in the full shot noise regime at high frequencies, whereas the interference effect responsible for the CBS cone, as the low frequency regime is approached, reflects itself on the development of an angular dependent Fano factor. A gradual transition as function of frequency between the full shot and pseudothermal noise case is also evident.

3.7 Conclusions

In this chapter we have studied for the first time photon noise measurements in the weak localization regime and shown that the transition from the full shot noise regime at high frequency to the full pseudothermal domain at low frequency can be investigated. We have experimentally demonstrated the enhancement of the Fano factor around the backscattering direction due to the CBS effect. Furthermore, we were able to extract the Fano factor CBS enhancement of the reflected radiation as function of both frequency and angle. It is remarkable that the enhancement of the Fano factor CBS depends on g_r^{-1}. The standard intensity coherent backscattering cone does not have such a contribution, whereas measuring photon noise gives access to $\overline{R^2}_{ab}$, from which the magnitude of g_r^{-1} effects can be extracted.

We have shown that measurements that span the full noise spectrum, from the shot to the excess noise regime, have the advantage to provide simultaneously information about the first and second moment of the probability distribution of the intensity of the reflected radiation. More specifically, our theory indicates that the enhancement displayed by the noise cone reveals information about the mesoscopic correlations that give rise to deviations from Rayleigh statistics in the strongly scattering regime.

The use of the CBS technique has in addition the potential to study the first and second moment of the probability distribution as function of the path length.

Sensitive photon noise experiments can be combined with coherent backscattering experiments, opening up new avenues for studying quantum optical aspects of diffuse wave transport. Future experiments on photon noise in the strong scattering regime may be performed to explore mesoscopic quantum corrections and localization. Furthermore, noise measurements could prove themselves useful also in systems that display gain, random lasing and absorption [67, 72, 75].

CHAPTER 4

Correlations in the mesoscopic regime

In this chapter we introduce an experimental technique optimized to investigate the intensity statistics of light transmitted through strongly scattering systems. We describe the steps taken in designing and building up an optical setup to induce and measure correlations caused by crossings of multiple scattering paths. These correlations are revealed in the intensity statistics. Although we find that the sought for effect remains difficult to observe with our current setup, we suggest improvements that may lead to an enhancement of the correlations for an easier detection.

4.1 Introduction

In mesoscopic electronics the conductance G of a system is given by [60, 103]

$$G = \frac{e^2}{h} \sum_{a,b} T_{ab}, \tag{4.1}$$

where T_{ab} is the transmission coefficient from channel a to channel b, e is the electron charge and h is Planck's constant. An important role is played by the fluctuations of G, mainly because of their universal character, after which they are named universal conductance fluctuations [104] (UCF).

In mesoscopic optics the relevant parameter is g, already seen in chapter 1, defined as $g \equiv \sum_{ab} \overline{T_{ab}}$, known also as the dimensionless conductance. It is found that

$$g = \frac{N\ell}{L}, \tag{4.2}$$

where N is the number of channels, ℓ the mean free path and L the sample length.

The parameter g plays an important role in determining the magnitude of the correlations that arise in transmission and reflection as multiple scattering paths propagate through a random medium. In a transmission configuration the correlations are defined as

$$C_{aba'b'} \equiv \overline{T_{ab}T_{a'b'}} - \overline{T}_{ab}\overline{T}_{a'b'}. \tag{4.3}$$

Feng et al. demonstrated [105] that

$$C_{aba'b'}(\Delta x) = C_1(\Delta x) + g^{-1}C_2(\Delta x) + g^{-2}C_3(\Delta x), \tag{4.4}$$

where Δx can be a generic variable that denotes for example frequency or time shift. In electronics, only the total conductance can be measured, while in optics more information can be obtained, for it is feasible to measure also T_{ab} and $T_a = \sum_b T_{ab}$ directly. Such a difference is crucial, because it means that in optics all of the terms in eq. (4.4) can be addressed singularly. The three contributions have in fact a precise physical meaning, as $C_1(\Delta x)$ is dominant when $a = a'$ and $b = b'$ and describes the fluctuation of the intensity in channel b induced by a field in mode a that illuminates the system, thus fluctuations of T_{ab}. The contribution of $C_2(\Delta x)$ is dominant when either $a = a'$ or $b = b'$. In the case $a = a'$, the term $C_2(\Delta x)$ accounts for the fluctuations of intensity over the entire spectrum of the outgoing modes induced by a field in single mode a impinging on the system, that is fluctuations of T_a. The last term $C_3(\Delta x)$ is the optical analogue of the UCF in electronics, and describes fluctuations due to correlations of all incoming modes with all outgoing ones, thus fluctuations of $\sum_{ab} T_{ab}$. It can be shown [106] that C_1, C_2, and C_3 correspond to contributions to the correlations due respectively to zero, one and two crossings between the scattering paths, and g^{-1} and g^{-2} provide us with a measure of the probability for the aforementioned crossings to take place.

Measuring mesoscopic correlations has been the goal of a number of experiments in the optical as well as the microwave regime. These correlations are determined by the magnitude of the total conductance g. Furthermore, the role of g has been central in investigating statistical signatures of localization with ultrasound and microwaves [107, 108]. Experiments in the microwave regime are considerably easier than those in the optical regime as the samples often consist of long closed tubes filled with scatterers [109–112] and the conductance g of the system is then well defined. The reason why a sample with a tube-like configuration allows for a clear definition of g is illustrated in fig. (4.1) and can be seen by recalling the expression for the number of modes N given by

$$N = \frac{2\pi A}{\lambda^2}. \tag{4.5}$$

As it is shown in eq. (4.5), N, the number of channels, is determined also by the area A of the illumination spot. The surface A is always well defined at both ends of a tube of fixed aperture. The effects we are looking for scale like g^{-1}, therefore, to have sizeable effects, it is important to be able to make g relatively small. By using closed tubes, g can be tuned by manipulating the size of the area A. On the other hand, in the optical regime the most common sample is a slab. Having a slab as sample complicates the estimate of g. The additional difficulty that arises in this case consists in the fact that, because of diffusion broadening, the incoming laser spot is not the same as the exit spot, given by the area of the illuminated spot at the back of the sample. The exit area is always bigger than the size of the incident spot. Diffusion broadening makes thus difficult the univocal definition of A and in turn the one of g [81].

Measurements of sample and transport of light properties in the multiple scattering regime rely on several techniques that can be divided into methods that measure average properties, like for instance total reflection and transmission, coherent backscattering, and techniques apt to measure fluctuations and correlations like speckle statistics [113] and frequency correlations [114]. Pioneering experiments in the optical regime have been performed to unveil correlations induced by g via intensity correlations and total transmission measurements [115–118].

The parameter g^{-1} can also be seen as the probability for two multiple scattering paths to intersect once, [119], [106] and that implies that long paths enhance this probability. Long paths are dominant in a transmission configuration.

Therefore we have decided to design a setup and perform experiments aimed at estimating g in a transmission configuration. As explained in chapter 1 the crossing of scattering paths inside the random system leads to deviations from Rayleigh statistics in the intensity distribution displayed by the speckle pattern. Our goal is to extract the magnitude of the C_2 type of correlations in strongly scattering samples by inducing and measuring deviations from Rayleigh statistics in the speckle pattern, in a transmission configuration. These measurements would be also of crucial importance to support or criticize claims of localization in the optical regime, expected when $g \leq 1$.

4.2 Sample

The samples that we used for our series of experiments are GaP nanowires. The used nanowires were grown epitaxially. To tune the length and the diameter of the nanowires a vapour-liquid-solid and lateral growth processes were used. The nanowires were grown on a GaP substrate with orientation (100). The majority of the wires forms angle of ~ 35 deg with the substrate. This alignment is due to the preferential growth of the nanowires in the direction set by the orientation of the substrate. The fabrication technique is detailed in [120]. The sample we used has a scattering strength $k_0\ell \simeq 1.6$, the thickness of the nanowires layer is $L = 1.6 \pm 0.2$ μm, and the mean free path is $\ell = 0.16 \pm 0.02$ μm at $\lambda = 633$ nm. Furthermore, the diameter of the nanowires amounts to 118 ± 19 μm. The used nanowires are among the strongest light scattering material [121].

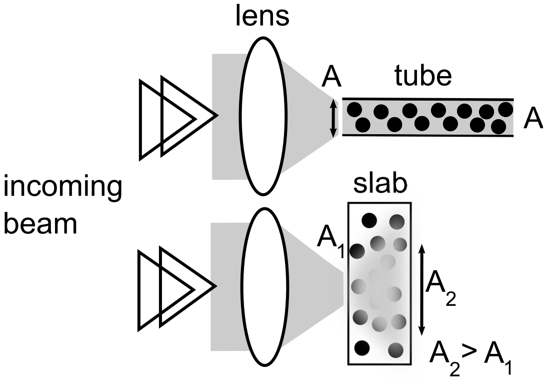

Figure 4.1: Difference between the closed-tube (top) and the slab (bottom) sample configurations for measurements performed in transmission. A lens focusses laser light on the samples to induce g^{-1} effects. Random scatterers (black circles) are embedded in both samples. The advantage offered by a closed-tube type of sample is that the number of incoming modes, related to the illumination area A, is well defined as A stays constant. For the case of the slab, diffusion broadening complicates the estimate of the number of modes as the illuminated area at the back (A_2) is bigger than the one at the front facet (A_1) of the sample.

4.3 Setup to measure spatial correlations

In this section we introduce the optical setup used to measure correlations in the mesoscopic regime. The setup, shown in fig. (4.2), has been optimized to perform many speckle averages by rotating and translating the sample to collect independent speckle patterns. A He-Ne laser has been chosen as light source for this experiment, as the small magnitude of the effect that we intend to measure requires having a source that is reliable and stable to a very high degree for a long time (few hours). A pinhole of size 100 μm is used in the confocal part of the setup to filter out unwanted reflections between the sample and the substrate. The size of this aperture is more than enough not to distort the image of the surface of the sample that we intend to project on the pinhole, as the illuminated area at the back of the sample is of the order of 10 μm.

4.3.1 Alignment procedure

The procedure used to perform the alignment of the setup is the following. First the sample is mounted. Then the front of the sample is illuminated with the focused He-Ne beam while the back of the sample is illuminated with white light. The pinhole is temporarily taken off the setup. The surface of the sample as well as the He-Ne spot coming in transmission through the sample are then imaged on the chip of the camera via two lenses. Subsequently, the pinhole is placed at distance 2f from the first lens and nudged with translation stages till the camera shows that the red He-Ne spot and the image of the surface of the sample looks sharp and aligned on

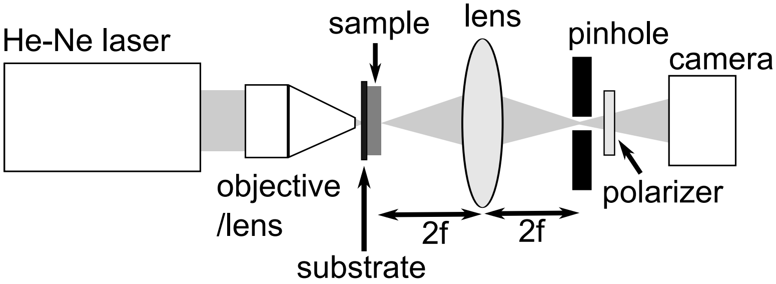

Figure 4.2: Setup used to measure mesoscopic correlations. The correlations are induced by focusing the beam on the sample so that the number of incoming channels can be tuned. The sample is mounted on a translation and rotation stage to perform speckle averaging. The rotation and translation of the sample occurs on the plane perpendicular to the propagation direction of the beam. The polarizer selects the polarization perpendicular to the incoming one, in order to make sure that only multiply scattered light enters the detection part of the setup. The confocal system placed after the sample is arranged in a 2f-2f configuration so that, when illuminated with white light, an image of the surface of the sample is formed on the pinhole plane. This strategy allows for filtering out spurious interferences effects due to multiple reflections that occur between the sample and the substrate.

the center of the pinhole. The perfect alignment is achieved when in addition also the sides of the pinhole are sharply imaged on the camera. Following this procedure the additional lens is removed and the camera moved closer to the pinhole till the chip is fully filled by the image. To double check the alignment, an objective can be placed behind the pinhole in order to collect a magnified image of the He-Ne spot and the sample surface, making sure that they are well centered within the pinhole. Furthermore, the sample is translated and rotated multiple times to check that the alignment stays stable. In the next subsection we show how the thin glass substrate on which the sample is mounted can influence the measurements.

4.3.2 Effect of sample substrate

In order to illustrate the influence of the sample substrate on the measurements we compare the configuration where the pinhole is mounted to the situation where the pinhole is taken off the setup. The effect of the pinhole is to produce a complex image which is composed of two parts: the speckle pattern that we are interested in, that is generated by the sample, and a different one, produced by the substrate, that is caused by the multiple reflections that occur between the sample and the substrate. This effect is illustrated in fig. (4.3). On inserting the pinhole, the disturbance due to the substrate disappears, and only the speckle produced by the sample remains.

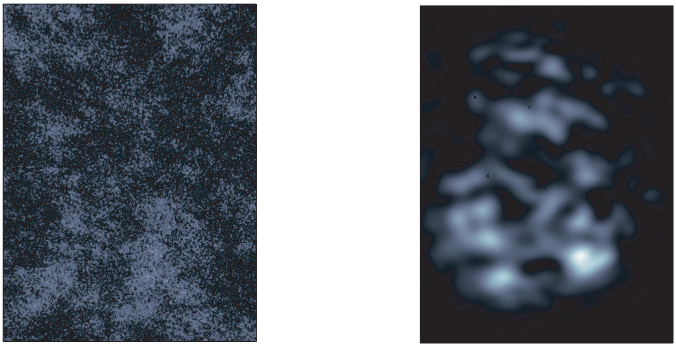

Figure 4.3: (left) Speckle pattern observed when there is no filtering pinhole. (right) Speckle pattern generated when the 100 μm pinhole is in place. The pinhole prevents the formation of an additional speckle pattern, due to the sample substrate, superimposed onto the speckle pattern produced by the sample.

4.3.3 Estimation of the beam spot size

In our experiments, aimed at highlighting interference effects among scattering paths propagating through a random medium, it is important to have an estimate of the size of the beam spot that impinges on the sample. As it is evident from eqs. (4.5) and (4.2) the number of incoming channels is proportional to the area occupied by the incoming beam on the sample. That means that the smaller the focus the bigger are the g^{-1} effects that we are able to induce.

The relay lens in fig. (4.2) has an effective numerical aperture NA = 0.25, while the objective used to produce fig. (4.4) has NA = 0.55. The relay lens sets the resolution of the imaging system to $\sim 3\ \mu m$. To measure the size of the beam spot we collected the image formed on the plane of the pinhole shown in fig. (4.4). Subsequently, given the circular symmetry, we performed radial averaging on the image and a gaussian fit to estimate the size of the beam spot to be 14 μm.

Using the estimated beam spot size and formulas (4.2) and (4.5) we can calculate g to be of the order of 200. Observing correlations induced by such a relatively big g with our setup will turn out to be very challenging.

4.3.4 Estimation of the position of the beam spot

In order to estimate the position of the focus we calculated the speckle autocorrelation functions using the data collected at different sample-lens distances. Per each distance we extracted the autocorrelation function from the 400 speckle patterns collected at each position. The 2D autocorrelation is calculated according to

$$C_A(\Delta\mathbf{x}) = \overline{\left(I\left(\mathbf{x}\right) - \overline{I}\right)\left(I\left(\mathbf{x}+\Delta\mathbf{x}\right) - \overline{I}\right)} \tag{4.6}$$

where the ensemble average, indicated as usual with an overline, is calculated over each dataset. With I we indicate the single intensity speckle pattern and with $\mathbf{x}$

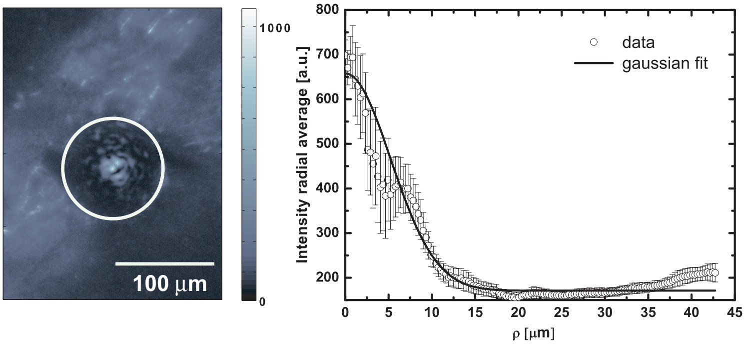

Figure 4.4: (left) Image of the 100 μm pinhole taken in order to check the alignment of the setup. The bright spot in the center is the image of the focused He-Ne spot collected at the back of the sample. This image shows that the pinhole does not distort the speckle pattern produced by the sample. (right) The radial average of the central part of the image on the left is shown. The diameter of the focused spot on the back of the sample can be estimated to be on the order of 14 μm. In order to collect the image we illuminate the pinhole with white light, as it is clear from the illuminated spot and that gives an intensity background higher than zero.

the 2D position vector.
The autocorrelation function is calculated by using the following formula

$$C_A\left(i,j\right) = \sum_{m=0}^{P-1} \sum_{n=0}^{Q-1} I(m,n) \bullet I(m+i,n+j), \tag{4.7}$$

implemented in Matlab, where $P \times Q$ represents the dimensions of the intensity matrix. Furthermore $0 \leq i, j \geq M + N - 1$.

The width of the autocorrelation function is related to the beam spot size; the smaller the incoming spot the bigger the width of the autocorrelation. In other words as we approach the position that corresponds to the smallest incoming beam spot the average speckle size increases. This property allows for an easy visual method to find the speckle patterns generated by the smallest incoming spot.

The measurements were performed by advancing the lens, mounted on the translation stage, towards the sample. Thus, if we start from an out of focus position we expect to observe an increase of the beam spot size up to the focus position, followed by a decrease of the spot size. In fig. (4.5) we show a set of three representative autocorrelation functions along with the estimated position of the position of the focus. The wider the autocorrelation function the bigger the corresponding spot.
It is instructive, using formula (4.2), to plot g as function of the incoming beam radius. The parabolic behaviour of g, shown in fig. (4.6), highlights the necessity of having a relatively small incoming beam to be able to readily observe g^{-1} effects.

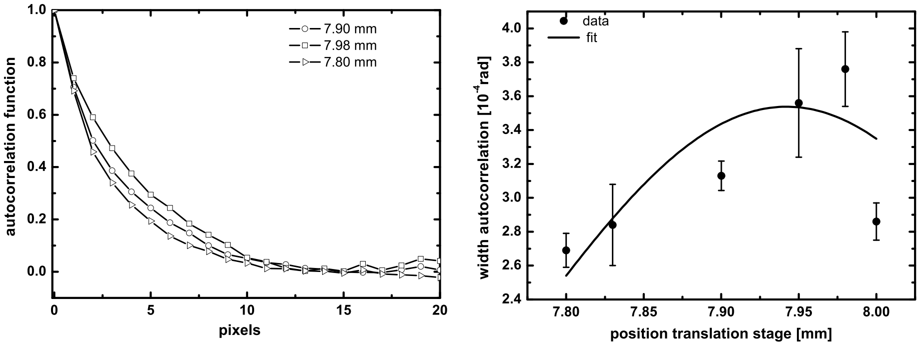

Figure 4.5: (left) Average autocorrelation functions for three representative distances lens-sample. Per each speckle pattern the radial averaged autocorrelation function has been calculated. The average has been computed by averaging the autocorrelation functions of the 400 images acquired at each sample-lens distance. The autocorrelation functions have been normalized by dividing them by their value at $\Delta x = 0$ displacement. (right) Average width of the autocorrelation functions versus the position of the translation stage on which is mounted the focusing lens. The black line is a gaussian fit to the data and evidences the focus around position 7.95 mm.

4.4 Data analysis

In this section we show different types of data analysis applied to the the acquired speckle patterns at different sample-lens distances, in search of mesoscopic correlations.

4.4.1 Data treatment

In this section we describe the properties of the collected speckle patterns and detail the normalization procedure. Our dataset consists of six sets of speckle patterns collected in correspondence of six different spot sizes. Each set comprises 400 speckle patterns. Prior to using the data for the different analyses presented in the following sections each speckle pattern has been divided by the average image, obtained by using all speckle patterns collected at a specific position.

4.4.2 Correlation between consecutive speckle patterns

In this section we estimate the correlation coefficients between subsequent acquisition steps and verify that the patterns acquired in this fashion show no correlation with one another.
Checking the absence of correlations between patterns acquired over consecutive steps allows for excluding residual correlations that are not due to g^{-1} effects. Since our measurements are performed over a series of sample rotation and translation steps, if a degree of correlation manifest itself it means that the translation and/or rotation steps are too closely spaced and there is some overlap between the

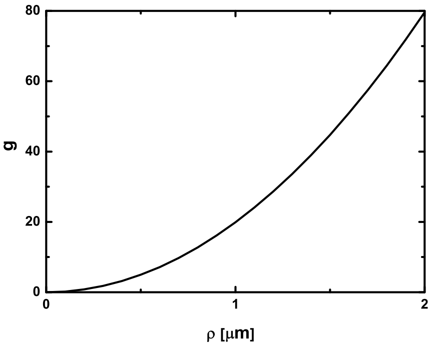

Figure 4.6: Calculation of the magnitude of g as function of the incoming beam radius. The calculation assumes a sample thickness $L = 10\ \mu m$ and a mean free path $\ell = 2\ \mu m$

sampling areas. More specifically, the speckle patterns are collected according to the following protocol.

1. The sample is rotated.
2. A series of twenty sample translations is performed.
3. At the end of the translation session the sample is translated back to the origin of the translation session.
4. The sample is rotated and a new translation session takes place.
5. The sample is rotated twenty times and each rotation is followed by twenty translation steps.

   In order to investigate the presence of residual correlations among the acquired speckle patterns we calculate the correlation coefficient between

1. The first translation step and all the following ones that belong to the same translation session
2. Consecutive rotation steps

The correlation coefficient relative to consecutive rotation steps is investigated because, since at the end of each translation session the sample is moved back to its original position , if the rotation angle is not big enough spurious correlations could arise.

The cross correlation coefficient C_X, used to estimate correlations between images is given by

$$C_X = \frac{\sum_{i,j} \left[I\left(i,j\right) - \overline{I}\right] \left[I_1\left(i,j\right) - \overline{I_1}\right]}{\sqrt{\left[\sum_{i,j} \left(I\left(i,j\right) - \overline{I}\right)^2\right] \left[\sum_{i,j} \left(I_1\left(i,j\right) - \overline{I_1}\right)^2\right]}}, \tag{4.8}$$

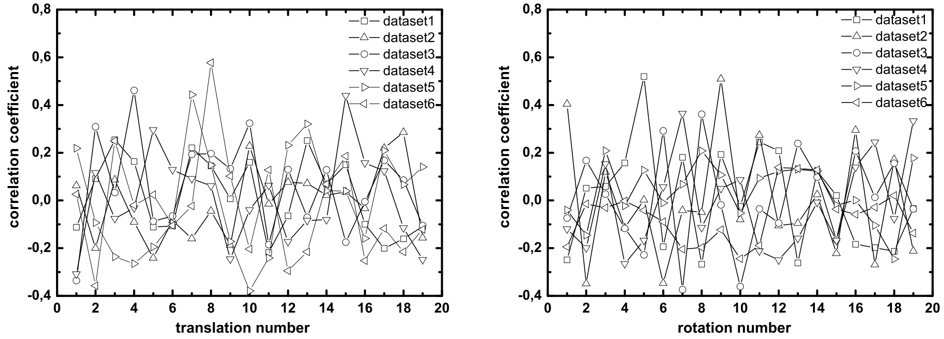

Figure 4.7: (left) Correlation coefficients between subsequent images acquired at the beginning of each translation session, i.e. each image corresponds to a different rotation angle for the sample. (right) Correlation coefficient between the first image of the translation session and all the following images belonging to the same translation session. In both cases the obtained correlation coefficients are well below one indicating lack of correlation among the images.

where $I(i,j)$ and $I_1(i,j)$ represent the intensity matrices related to two different images, i and j are the pixel coordinates and $\overline{I}$ and $\overline{I}_1$denote the average intensities. The values acquired by the correlation coefficient span between -1, meaning perfect anti-correlation, and 1, meaning that two images are perfectly correlated.The correlation coefficient can also acquire the value 0, meaning no correlation between two images. In fig. (4.7) we present typical correlation coefficients for our datasets. It is clear looking at fig. (4.7) that no measurable correlation trend arises from the data, as the correlation coefficient fluctuates between -0.4 and 0.6.

4.4.3 Intensity probability distribution

In order to detect deviations from Rayleigh statistics we resort to the model introduced by Nieuwenhuizen and van Rossum [41]. Their model is given by

$$P\left(\frac{I}{\overline{I}}\right) = \exp\left(-\frac{I}{\overline{I}}\right)\left\{1+\frac{1}{3g}\left[\left(\frac{I}{\overline{I}}\right)^2 - 4\left(\frac{I}{\overline{I}}\right)+2\right]\right\}, \tag{4.9}$$

where with I we denote the intensity. The influence of g^{-1} effects is explicit in eq. (4.9). An exponential distribution is recovered, as expected, when $g \longrightarrow \infty$.

In fig. (4.8) the calculated intensity probability distribution is shown for different g values and compared to the Rayleigh distribution. This probability distribution introduced by Nieuwenhuizen and van Rossum highlights the central role played by the high intensity values. The deviations induced by non-Rayleigh statistics at low intensities are almost indistinguishable from a simple exponential distribution, especially for high g values. The fact that departure from Rayleigh statistics is mostly present in the tail of the distribution poses strict constraints on experiments aimed at measuring these deviations. The experimental difficulties stem from the

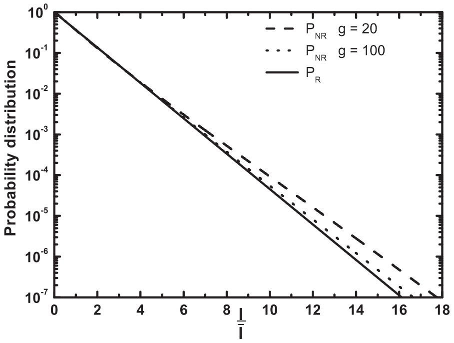

Figure 4.8: Calculation that shows a comparison between Rayleigh statistics and non Rayleigh statistics with $g = 100$ and $g = 20$. P_R and P_{NR} denote Rayleigh distribution and non Rayleigh distribution respectively. P_{NR} is calculated using the model of Nieuwenhuizen and van Rossum.

high intensity values being also the ones that occur the least often, therefore very long and intensive measurement sessions are required to reduce the statistical error and acquire reliable datasets.

A different way to look at deviations from gaussian statistics is given by the second moment of the intensity probability distribution. Using eq. (4.9) it is possible to calculate the second moment of the distribution, given by

$$\frac{\overline{I^2}}{\overline{I}^2} = 2 + \frac{4}{3g}. \tag{4.10}$$

From eq. (4.10) it becomes clear that the presence of interference effects due to correlations reflects on the second moment of the probability distribution becoming greater than two. In case of absence of correlations, perfect gaussian statistics is recovered, and the second moment equals two. Therefore an alternative approach to assess experimentally deviations from gaussian statistics consists in measuring the values of the second moments of the distribution. Moreover, extracting the second moment from the data is easier and more straightforward than building up the entire probability distribution. However, the analysis of the full probability distribution provides us with a major degree of control over the experiment. For example, by investigating the distribution we could decide whether the high intensity values or the low ones deviate from a perfect Rayleigh statistics. The measurements of the intensity probability distributions and second moments are presented in the following sections.

4.4.4 Measurement of the second moment of the intensity probability distribution

In this section we report on measurements of the intensity probability distribution and the second moment of the speckle patterns acquired in our experiments. The

$\frac{\overline{I^2}}{\overline{I}^2}$	distance sample lens
1.7813 ± 0.26	7.85 mm
1.7643 ± 0.24	7.89 mm
1.7973 ± 0.28	7.95 mm
1.8134 ± 0.28	7.97 mm
1.8056 ± 0.26	7.985 mm
1.8188 ± 0.28	8.00 mm

Table 4.2: Calculation of the ratio $\frac{\overline{I^2}}{\overline{I}^2}$ relative to the intensity probability distribution at different distances sample-lens. The displayed error is the standard deviation calculated over 400 realizations at each position.

entire dataset of 400 images per fixed distance lens-sample is used.

The second moment is defined as

$$r \equiv \frac{\overline{I^2}}{\overline{I}^2}. \tag{4.11}$$

The formula used to infer the second moment from the experiment is given by

$$\frac{\overline{I^2}}{\overline{I}^2} = N_1 N_2 N_s \frac{\sum\limits_{i,j,s} \left[I_s\left(i,j\right)\right]^2}{\left[\sum\limits_{i,j,s} I_s\left(i,j\right)\right]^2}, \tag{4.12}$$

where I_s denotes the s-th speckle pattern, i and j run over the pixels coordinates of the $2D$ images, with $i = 1..N_1$; $j = 1..N_2$; $s = 1..N_s$. The product $N_1 N_2$ indicates the number of used pixels per image and N_s the total number of employed images. The results from the analysis of the second moments are shown in table (4.2).

In all analysed cases the value of the second moment is, within experimental accuracy, compatible with two, but systematically lower, perhaps for a degradation of the speckle contrast. That signifies that, at present, the effect of the mesoscopic correlations remains out of reach. This is probably due to the fact that our incoming beam spot is still not small enough to induce g^{-1} effects.

4.4.5 Measurement of the intensity probability distribution

The intensity probability distributions derived from the data are presented in figs. (4.9-4.11). In order to better investigate the behaviour of the probability distributions we show, along with the intensity probability distribution data, also the ratio of the measured distributions to a Rayleigh distribution. Our analysis shows that the generated g^{-1} effects are below our detection sensitivity. This is compatible with

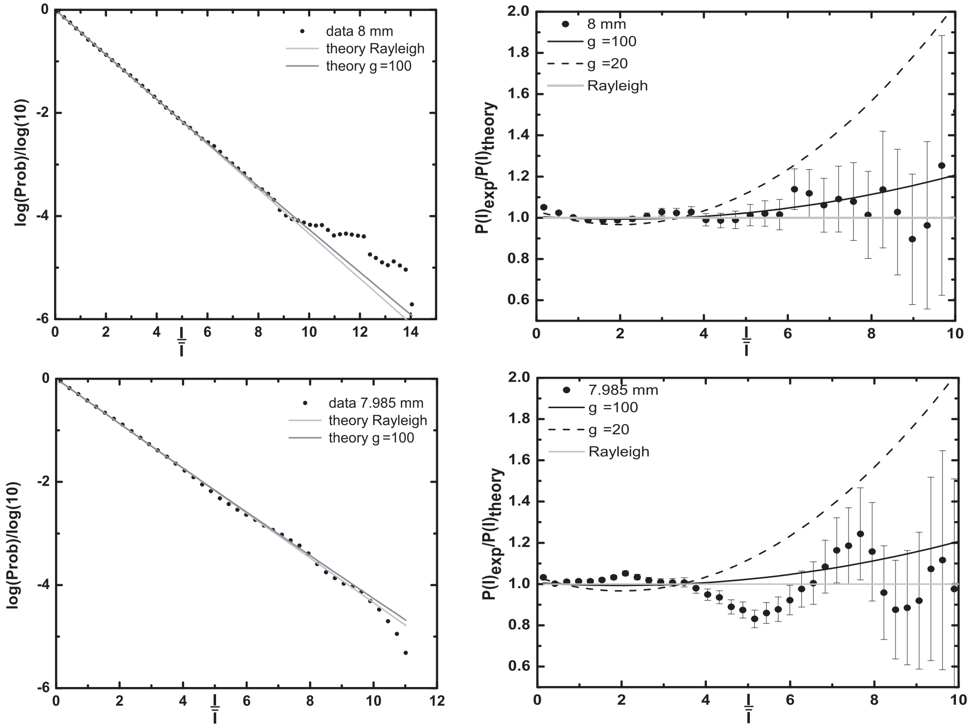

Figure 4.9: (left) Intensity probability distributions extracted from two datasets corresponding to two different incoming beam spots. (right) Along with the intensity probability distributions also the ratio of the experimental distributions to the Rayleigh distributions is shown. The relative error bars are calculated by using formula (4.14) for the relative error. For comparison we also show deviation expected for $g = 20$, dashed line, and $g = 100$, solid black line. The horizontal line intersecting the probability axis at 1 marks the case of perfect Rayleigh statistics.

an estimated $g \approx 200$. The most probable reason for the lack of observable effects is caused by the size of our incoming spot size, which is too big to be able to observe deviations from Rayleigh statistics. This analysis shows that the measured probability distributions do not exhibit a clear deviation from a Rayleigh distribution, and that confirms the results from the second moment analysis. In all the analysed cases there is no clear sign of deviations due to g^{-1} effects.

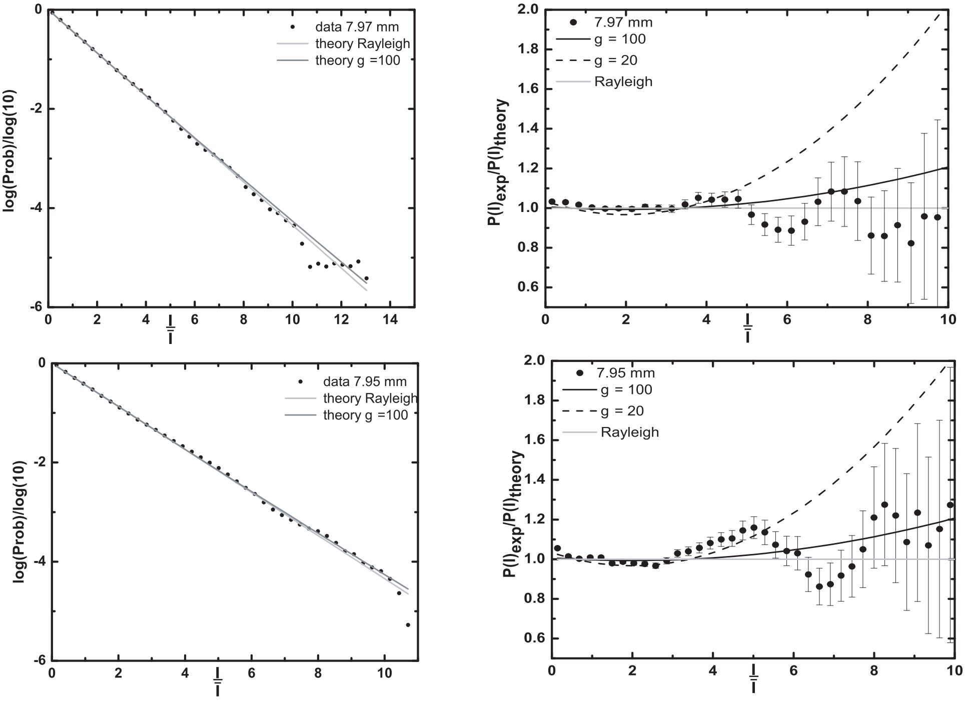

Figure 4.10: (left) Intensity probability distributions extracted from two datasets corresponding to positions 7.97 mm and 7.95 mm. The remaining details of the figure are explained in fig. (4.9).

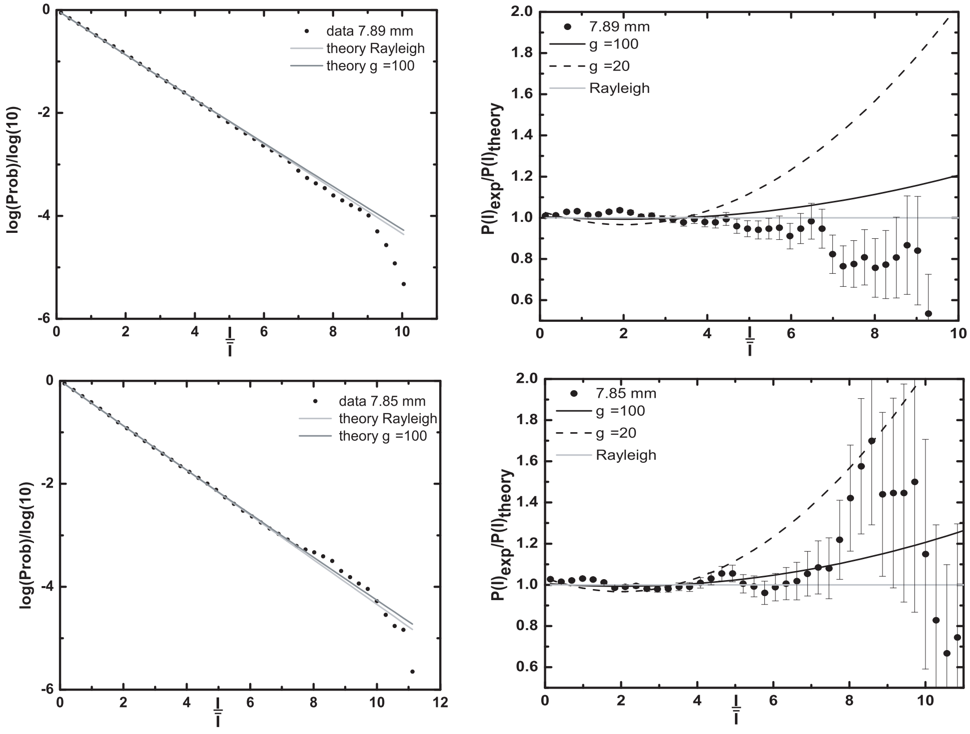

Figure 4.11: (left) Intensity probability distributions extracted from two datasets corresponding to positions 7.85 mm and 7.89 mm. The remaining details of the figure are explained in fig. (4.9).

4.5 Conclusions

In this chapter we have shown how to design and build a setup to induce and detect g^{-1} correlations in strongly scattering samples. Such a setup would be of great aid to fully establish strong localization features of solid samples.

We have used a confocal technique to eliminate spurious reflections between the sample and the sample substrate, fully characterized our setup and showed that we were able to acquire speckle patterns corresponding to independent realization of the disorder.

However, at present, the correlations that we are able to induce are below the detection sensitivity of our setup and no clear trend or transition is individuated in our analysed data as we scan our focussing system, advancing it gradually from out-of-focus to in-focus configurations. This result can be due to the fact that our incoming beam spot is not small enough, therefore the number of excited modes becomes bigger than expected, and so does g, that than increases out of our setup's sensitivity range.

To overcome this experimental obstacle the setup could be improved by replacing our lens with a powerful objective to decrease the number of excited modes and thus decreasing g. An objective with an NA of 0.90 could be the key to observe a sizeable effect. Replacing the objective in the current setup would increase the magnitude of the g^{-1} effects. The realization of such a setup is not free of major technical difficulties, such as the high stability required over the extremely long time needed to acquire enough measurements to have statistically significant data at high intensities. An additional challenge consists in avoiding the sample to wobble over the thousands of speckle measurements needed to reduce the statistical error. Wobbling of the sample can cause a variation of the distance objective-sample, producing a change of the the size of beam spot on the sample and in turn introducing supplementary uncertainty in the determination of g. Although requiring extensive testing and calibration measurements, we estimate that the use of such an improved setup will produce a g of the order of 20.

It would also be interesting to experimentally study the influence of absorption and gain on the transmitted intensity distribution. Numerical simulations that take into account both effects have been performed on quasi 1D systems [43].

4.6 Appendix

4.6.1 Error on the probability distribution

To evaluate the error on the intensity probability distribution retrieved experimentally, we proceed as follows. The intensity data extracted from the speckle patterns are sorted in intensity bins to build up the probability distributions. The normalized discrete probability P_i is given by

$$P_i = \frac{N_i}{N_{tot}}, \tag{4.13}$$

where N_i indicates the number of collected intensity events in the i-th bin. With N_{tot} we indicate the total number of intensity events. We argue that in this case the relevant quantity that determines N_{tot} is the total number of independent speckle spots collected in each experimental run at a given distance sample-lens. Assuming Poisson statistics for the distribution of the number of intensity events in each bin we have that the error on the counts δN_i is given by $\delta N_i = \sqrt{N_i}$. Then the relative error $\frac{\delta P_i}{P_i}$ is

$$\frac{\delta P_i}{P_i} = \frac{1}{\sqrt{P_i N_{tot}}}. \tag{4.14}$$

The number of independent speckles spots can be calculated once the average width of the speckle autocorrelation function per each dataset has been calculated. By dividing the size of the single speckle image to the extracted average speckle size N_{tot} can be obtained. Using eq. (4.14) we calculated the error bars presented in figs. (4.9-4.11).

Summary

In this thesis we have investigated the propagation of optical noise through multiple scattering media.The general idea is depicted in fig. (E-I). Multiple scattering systems are characterized by a strong light-matter interaction that manifests itself by the many scattering events that light undergoes in the medium. The scattering strength of the system is determined by the mean free path ℓ, defined as the mean distance between consecutive scattering events. Given a fixed system size, the shorter the mean free path the more strongly scattering the medium is. Milk and clouds are examples of multiple scattering systems. We can not easily see an object embedded in these media, and that means that the mean free path is in these cases very small compared to the size of the systems.

Drawing inspiration from the study of noise in disordered electronic systems, we exploited the inherent noise characteristics of laser systems to extract valuable information from multiple scattering media, such as the mean free path and the modalities of light transport.

Noise is not regarded as something that spoils the measured signals and needs to be discarded and minimized. On the contrary, noise is employed as an investigation tool. In order to use noise as a probe it is necessary to characterize the noise sources, in our case laser systems. Lasers have two main types of noise whose signature is the different scaling as function of intensity. High frequency noise scales linearly with the intensity, and is termed quantum noise, while low frequency noise scales quadratically with the intensity and is termed excess (or classical) noise.

As a first step, in chapter 2, we measure the total reflection of quantum and classical optical noise from a collection of samples and show that reflection of quantum and classical noise follow different theories. Furthermore, the mean free path can be recovered from the noise measurements and the obtained values are in agreement with the ones extracted from intensity measurements. Moreover, we find a linear scaling of the fluctuations as function of the incoming noise allowing thus for a unified representation of classical and quantum noise. The results presented in

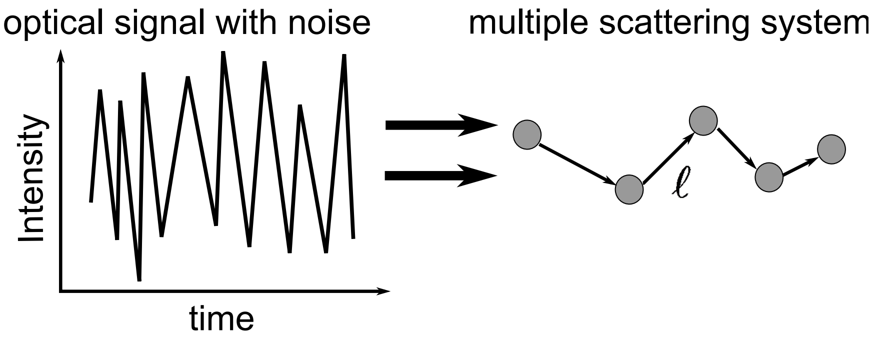

Figure E-I: Incoming optical signal with noise propagates through a multiple scattering system (the scatterers are depicted by grey circles). The goal of the research presented in this thesis is to study the transport of light fluctuations through strongly scattering media. The scattering strength of the system is determined by the mean free path ℓ. The shorter the mean free path the more strongly scattering the medium is.

chapter 2 are not sensitive to the direction of the beam exiting the sample as the collected signal is averaged, by means of an integrating sphere, over all directions.

In chapter 3, we extend our investigations of optical noise by making use of coherent backscattering. Coherent backscattering is classically used to study the transport of light through random media and demonstrates that interference effects survive the ensemble averaging process. The measured intensity signal in the backscattering direction, plotted as intensity as function of the backscattering angle, acquires the shape of a cone, termed the backscattering cone. In chapter 3, we show that coherent backscattering can be used to investigate the transport of optical noise through disordered media. By using an electronic spectrum analyser we investigate the noise content of the signal and show that quantum noise and excess noise exhibit a coherent backscattering effect. Moreover, we theoretically show that the excess noise backscattering cone gives access to the second moment of the intensity probability distribution. In turn, from the second moment it is possible to extract information about the conductance g that conveys information about to what extent light propagates along independent scattering paths. The importance of the parameter g in the study of mesoscopic systems resides in the fact that the value acquired by this parameter signals the approach to the Anderson localization transition. In the Anderson localization regime light stays confined in the medium because strong light scattering causes a breakdown of light diffusion due to interference.

Finally, in chapter 4, we extend our work on the parameter g. The conductance g depends on the mean free path and the sample size as well as on the cross section of the beam impinging on the sample. While the mean free path and the sample size are fixed once the sample is chosen, we can still play with the beam size to vary g. In order to achieve that we built a setup that allows to change g by displacing the optics that focusses the light onto the sample. Our setup allows also to record the speckle patterns produced by the transmitted light. Speckle patterns produced by independent scattering paths generate a Rayleigh intensity probability distribution. From the speckle patterns we were able to extract the probability distribution of the transmitted intensity. Furthermore, we discuss how interference effects, quantified by the values assumed by g, give rise to deviations from the Rayleigh distribution.

Samenvatting

In dit proefschrift doen we verslag van onderzoek naar de voortplanting van optische ruis in meervoudig verstrooiende media. Het algemene idee is weergegeven in figuur (N-I). Meervoudig verstrooiende systemen worden gekenmerkt door een sterke interactie tussen licht en materie en zich manifesteert door de vele verstrooiingsevenementen die plaats vinden in het medium. De verstrooiingskracht van het systeem wordt bepaald door de gemiddelde vrije weglengte ℓ, gedefinieerd als de gemiddelde afstand tussen de opeenvolgende verstrooiingsevenementen. Hoe korter de gemiddelde vrije weglengte hoe sterker de verstrooiing in het medium is. Melk en wolken zijn voorbeelden van meervoudige verstrooiende systemen.In deze media kunnen voorwerpen worden verborgen. Dat betekent dat de gemiddelde vrije weglengte in deze gevallen zeer klein is in vergelijking met de grootte van het systeem. Genspireerd door de studie van ruis in wanordelijke elektronische systemen, hebben we gebruik gemaakt van de inherente ruis eigenschappen van lasersystemen om waardevolle informatie uit meervoudig verstrooiende media te halen, zoals de gemiddelde vrije weglengte en de modaliteiten van het lichttransport.

We laten zien dat ruis niet beschouwd hoeft te worden als iets dat de gemeten signalen beschadigt en minimaliseert. Integendeel, ruisanalyse blijkt een uitstekende methode om onderzoek mee te verrichten. Om de ruis te gebruiken als een probe is het noodzakelijk om de ruisbronnen te karakteriseren, in ons geval lasersystemen. Lasers vertonen twee belangrijke soorten ruis die zich kenmerken door verschillende gedragingen als functie van de intensiteit. Hoog frequentie ruis schaalt lineair met de intensiteit, en wordt quantum ruis genoemd, terwijl de lage frequentie kwadratisch schaalt met de intensiteit en exces (of klassieke) ruis wordt genoemd.

Allereerst, in hoofdstuk 2, meten we de totale reflectie van de quantum en klassieke optische ruis uit een verzameling van monsters en laten we zien dat de reflectie van quantum en klassieke ruis worden geregeerd door verschillende theorien. Bovendien kan de vrije weglengte worden bepaald door de ruismetingen en blijken de verkregen waarden in overeenstemming te zijn met die uit intensiteits

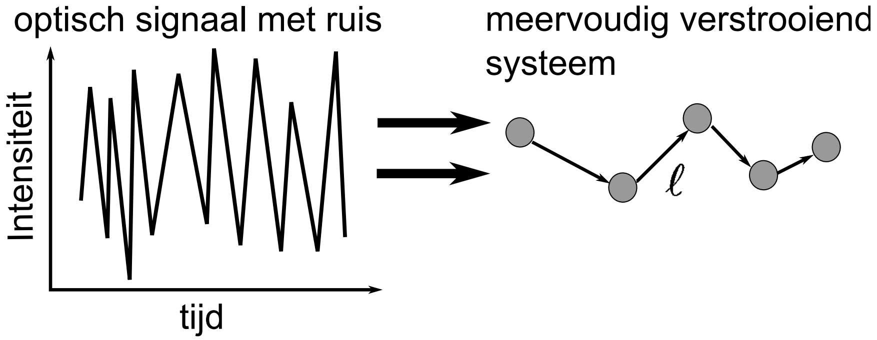

Figure N-I: Een inkomend optisch signaal met ruis plant zich voort door een systeem dat meervoudig verstrooit. (de verstrooiers worden weergegeven door grijze cirkels). Het doel van het onderzoek gepresenteerd in dit proefschrift is om het transport van intensiteitsfluctuaties van licht door sterk verstrooiende systemen te bestuderen. De verstrooiingskracht van het systeem wordt bepaald door de gemiddelde vrije weglengte ℓ. Hoe korter de gemiddelde vrije weglengte van het medium hoe sterker de verstrooiing.

metingen. Verder, vinden we een lineair verband tussen de uitgaande fluctuaties en de inkomende ruis waardoor een gezamenlijk beeld van klassieke en quantum ruis is bepaald. De resultaten van de experimenten gepresenteerd in hoofdstuk 2 zijn niet gevoelig voor de richting van de bundel omdat het gemeten signaal gemiddeld wordt over alle richtingen, door middel van een integrerende bol.

In hoofdstuk 3, breiden we ons onderzoek naar optische ruis uit door gebruik te maken van coherente terugverstrooiing. Coherente terugverstrooiing wordt normaal gesproken gebruikt om het transport van licht door wanordelijke media te bestuderen en toont aan dat interferentie-effecten ensemble middeling overleven. De gemeten intensiteit van het signaal in de terugverstrooingsrichting, uitgezet als functie van de terugverstrooiingshoek,neemt de vorm aan van een kegel, de zogenoemde terugstrooikegel. In hoofdstuk 3 laten we zien dat coherente terugverstrooiing kan worden gebruikt om de voortplanting van optische ruis door middel van wanordelijke media te onderzoeken. Door gebruik te maken van een elektronische spectrum analyser onderzoeken we de ruisinhoud van het signaal en laten we zien dat quantum ruis en klassieke ruis coherente terugstroiing vertonen. Bovendien hebben we theoretisch laten zien dat de terugstrooikegel voor klassieke ruis toegang geeft tot het tweede moment van de intensiteitskansverdeling. Vanaf het tweede moment is het mogelijk om informatie te halen over de parameter g die informatie verschaft over in hoeverre het licht zich voortplant langs onafhankelijke verstrooiingspaden. Het belang van de parameter g in de studie van mesoscopische systemen wordt weergegeven door het feit dat de waarde van deze parameter de nabijheid van de overgang naar Anderson lokalisatie aangeeft. In het Anderson lokalisatie regime blijft het licht opgesloten in het medium, want sterke lichtverstrooiing veroorzaakt een afbraak van lichtdiffusie als gevolg van interferentie.

In hoofdstuk 4 tenslotte, breiden we ons werk op de parameter g uit. De parameter g hangt af van de gemiddelde vrije weglengte, de grootte van het systeem en de diameter van de lichtbundel op het monster. Terwijl de gemiddelde vrije weglengte en de grootte van het systeem vastliggen zodra het monster wordt gekozen, kunnen we nog steeds spelen met de bundelgrootte om g te variren. Om dat te bereiken hebben we een opstelling gebouwd die het mogelijk maakt om g te veranderen door het verplaatsen van de optica die het licht op het monster focusseert. Door middel van onze opstelling kunnen wij spikkelpatronen opnemen die door het uitgezonden licht zijn gegenereerd. Spikkelpatronen geproduceerd door onafhankelijke verstrooiingspaden genereren een Rayleigh intensiteitsdistributie. Uit de spikkelpatronen kunnen we de kansverdeling berekenen van de overgedragen intensiteit. Verder bespreken we hoe interferentie-effecten, gekwantificeerd door de waarden aangenomen door g, aanleiding geven tot afwijkingen in de Rayleigh distributie.

Acknowledgements

The past years have been very intense and I feel like I have learnt much about physics as well as about less technical subjects. A number of people have contributed to the successful completion of this thesis. First of all I would like to thank my promotor for having given me the opportunity to work on such an original and multifaceted topic. Ad, thank you for making always time in your busy schedule to discuss my project. Your unconventional view on physics, scientists, people, politics, and many other subjects can be very motivating and inspiring. Otto, my daily supervisor and copromotor, has often intervened to keep my attention focussed by offering useful suggestions and showing interest in my progress, even after he started up his own group in Southampton. Otto, I am very impressed by your experimental ability and the determination with which you obtain results from your experiments.

Patrick, once Otto moved to England, helped me to stay on course through the intricate jungle of the final turns and rushes that led me to finishing my thesis. Furthermore, he introduced me to the magical world of the Alexander technique, instrumental to help me stay calm and balanced in many situations. Patrick, I also thank you for accepting to be my paranimf. Bergin, who also kindly accepted to be my paranimf, has many times reminded me to highlight my victories and often suggested alternative scenarios by coming up with smart and surprising interpretations of many facts of life.

Our group, the Photon Scattering group, has always attracted original and sparkling people. That made each day never boring. Sanli, Bernard, Tom, Timmo, Ramy, Bergin, Jochen, Iwert, Dmitry, Patrick, Otto, Ronald thank you for the exciting discussions about physics as well as some memorable lunch discussions. Thank you Rob and Wouter for assisting me with many administrative issues. Over the years many guests collaborated with our group, and in particular I would like to thank Stephan for his contributions to the experiments presented in chapter 4. The Photonic Bandgap group, led by Willem, has always had a fruitful interaction with our group. Thank you Willem for your suggestions and comments at the group discussions, at the COPS-AMOLF meetings, and for accepting to be on my thesis committee. Thank you to all the members of the Photonic Bandgap group and COPS in Twente for the interest they showed in my work and the inspiring physics discussions; thank you Allard, Elbert, Ivo, Ivan, Jacopo, Donang, Rajesh, Willem T., Philip, Cock, Tijmen, Bart, Merel, Steven, Leon, Karen M., Karen vdM, Hannie, Alex, Georgios, Emre, Duygu, Simon, Elahe.

Data analysis can be quite stressful and it is important to have room mates at work that ease the pain with their positive and cheerful attitude; thank you Alex, Patrick, Ramy, Ernst Jan, Rob and Ivana. I would like to thank the group leaders of the Center for Nanophotonics at AMOLF, Albert, Kobus, Jaime, Willem, Femius and Ad for setting up and maintaining alive the weekly nanophotonics colloquium, where I have learnt how to present science to a demanding, witty and sometimes aggressive audience.

At AMOLF I would like to thank the IT department and in particular Wiebe and Rutger for their help with many issues, and the skilled technicians from the machine shop, guided by Wim and Iliya, who designed and realized the pieces I needed.

I also want to thank all the people who helped me improve my dutch by patiently correcting my mistakes and making the effort of not talking in english to me: thank you Willem, Tijmen, Ramy, Timmo.

’All work and no play makes Jack a dull boy’......I want to thank Maarten, Loreto, Kramer, Ana, Tijmen, Sergio, Laura, Lara, Michael (Branko), Patrick, Gianluca, Rosalie, Bianca and Berta for gracing much of my time with many cheerful, fun, eat, laugh, holiday, sport, dance and unique moments.

Infine ringrazio i miei genitori e mia sorella per il continuo supporto e incoraggiamento incondizionati di tutti questi anni, e anche per avermi fatto osservare molte cose e situazioni da angoli diversi dal mio.

Paolo

Bibliography

[1] R. Landauer, “Condensed-matter physics: The noise is the signal,” *Nature*, vol. 392, pp. 658–659, Apr. 1998. — p.13.

[2] R. Brown, “A brief account of microscopical observations made in the months of june, july and august, 1827, on the particles contained in the pollen of plants; and on the general existence of active molecules in organic and inorganic bodies,” *Phil. Mag.*, vol. 4, pp. 161–173, 1828. — p.14.

[3] P. Reimann, “Brownian motors: noisy transport far from equilibrium,” *Physics Reports*, vol. 361, pp. 57–265, Apr. 2002. — p.14.

[4] R. Di Leonardo, L. Angelani, D. Dell’Arciprete, G. Ruocco, V. Iebba, S. Schippa, M. P. Conte, F. Mecarini, F. De Angelis, and E. Di Fabrizio, “Bacterial ratchet motors,” *Proceedings of the National Academy of Sciences*, vol. 107, pp. 9541–9545, May 2010. — p.14.

[5] S. Perkins, “Dashing rogues: freak ocean waves pose threat to ships, deep-sea oil platforms,” *Science News*, vol. 170, pp. 328–329, 2006. — p.14.

[6] D. Solli, C. Ropers, and B. Jalali, “Active control of rogue waves for stimulated supercontinuum generation,” *Physical Review Letters*, vol. 101, no. 23, pp. –, 2008. — p.14.

[7] D. Solli, B. Jalali, and C. Ropers, “Seeded supercontinuum generation with optical parametric down-conversion,” *Physical Review Letters*, vol. 105, no. 23, pp. –, 2010. — p.14.

[8] D. R. Solli, C. Ropers, P. Koonath, and B. Jalali, “Optical rogue waves,” *Nature*, vol. 450, pp. 1054–1057, Dec. 2007. — p.14.

[9] M. Shats, H. Punzmann, and H. Xia, “Capillary rogue waves,” *Physical Review Letters*, vol. 104, no. 10, pp. –, 2010. — p.14.

[10] J. Kasparian, P. Bjot, J.-P. Wolf, and J. Dudley, “Optical rogue wave statistics in laser filamentation,” *Optics Express*, vol. 17, no. 14, pp. 12070–12075, 2009. — p.14.

[11] K. Nishida, J.-P. Montagner, and H. Kawakatsu, “Global surface wave tomog-

raphy using seismic hum," *Science*, vol. 326, pp. 112–112, Oct. 2009. — p.14.

[12] N. Shapiro, M. Campillo, L. Stehly, and M. H. Ritzwoller, "High-resolution surface-wave tomography from ambient seismic noise," *Science*, vol. 307, pp. 1615–1618, 2005. — p.14.

[13] F. Brenguier, N. M. Shapiro, M. Campillo, V. Ferrazzini, Z. Duputel, O. Coutant, and A. Nercessian, "Towards forecasting volcanic eruptions using seismic noise," *Nature Geosci*, vol. 1, pp. 126–130, Feb. 2008. — p.14.

[14] I. Reidler, Y. Aviad, M. Rosenbluh, and I. Kanter, "Ultrahigh-speed random number generation based on a chaotic semiconductor laser," *Physical Review Letters*, vol. 103, no. 2, p. 024102, 2009. — p.14.

[15] I. Reidler, Y. Aviad, M. Rosenbluh, and I. Kanter, "Ultrahigh-speed random number generation based on a chaotic semiconductor laser," 2009. — p.14.

[16] T. E. Murphy and R. Roy, "Chaotic lasers: the world's fastest dice," *Nature Photon.*, vol. 2, pp. 714–715, 2008. — p.14.

[17] M. Ren, E. Wu, Y. Liang, Y. Jian, G. Wu, and H. Zeng, "Quantum random-number generator based on a photon-number-resolving detector," *Phys. Rev. A*, vol. 83, pp. 023820–, Feb. 2011. — p.14.

[18] A. Uchida, "Fast physical random bit generation with chaotic semiconductor lasers," *Nature Photon.*, vol. 2, pp. 728–732, 2008. — p.14.

[19] S. Datta, *Electronic Transport in Mesoscopic Systems.* Cambridge University Press, 1995. — p.14.

[20] Y. Imry, *Introduction to Mesoscopic Systems.* Oxford University Press, 1997. — p.14.

[21] J. T. o, B. Trauzettel, M. Titov, A. Rycerz, and C. W. J. Beenakker, "Sub-poissonian shot noise in graphene," *Physical Review Letters*, vol. 96, no. 24, p. 246802, 2006. — p.14.

[22] R. Loudon, *The quantum theory of light.* Oxford University Press, 2000. — p.14, 36, and 52.

[23] R. J. Glauber, "The quantum theory of optical coherence," *Phys. Rev.*, vol. 130, pp. 2529–2539, Jun 1963. — p.14.

[24] H. J. Kimble, M. Dagenais, and L. Mandel, "Photon antibunching in resonance fluorescence," *Phys. Rev. Lett.*, vol. 39, pp. 691–, Sept. 1977. — p.14.

[25] D. F. Walls, "Squeezed states of light," *Nature*, vol. 306, pp. 141–146, 1983. — p.14 and 31.

[26] R. E. Slusher, L. W. Hollberg, B. Yurke, J. C. Mertz, and J. F. Valley, "Observation of squeezed states generated by four-wave mixing in an optical cavity," *Phys. Rev. Lett.*, vol. 55, pp. 2409–2412, 1985. — p.14.

[27] C. K. Hong and L. Mandel, "Experimental realization of a localized one-photon state," *Phys. Rev. Lett.*, vol. 56, pp. 58–, Jan. 1986. — p.14.

[28] R. M. Shelby, M. D. Levenson, S. H. Perlmutter, R. G. DeVoe, and D. F. Walls, "Broad-band parametric deamplification of quantum noise in an optical fiber," *Phys. Rev. Lett.*, vol. 57, pp. 691–, Aug. 1986. — p.14.

[29] P. G. et al, "Experimental evidence for a photon anticorrelation effect on a beam splitter: A new light on single-photon interferences," 1986. — p.14.

[30] H. Vahlbruch, M. Mehmet, S. Chelkowski, B. Hage, A. Franzen, N. Lastzka,

S. Goßler, K. Danzmann, and R. Schnabel, “Observation of squeezed light with 10-db quantum-noise reduction,” *Phys. Rev. Lett.*, vol. 100, p. 033602, Jan 2008. — p.15.

[31] R. Schnabel, “Gravitational wave detectors: Squeezing up the sensitivity,” *Nat Phys*, vol. 4, pp. 440–441, June 2008. — p.15.

[32] K. McKenzie, D. A. Shaddock, D. E. McClelland, B. C. Buchler, and P. K. Lam, “Experimental demonstration of a squeezing-enhanced power-recycled michelson interferometer for gravitational wave detection,” *Phys. Rev. Lett.*, vol. 88, pp. 231102–, 2002. — p.15.

[33] C. H. Henry and R. F. Kazarinov, “Quantum noise in photonics,” *Rev. Mod. Phys.*, vol. 68, pp. 801–, July 1996. — p.15.

[34] A. Lagendijk, B. Van Tiggelen, and D. Wiersma, “Fifty years of anderson localization,” *Physics Today*, vol. 62, no. 8, pp. 24–29, 2009. — p.16.

[35] P. W. Anderson, “Absence of diffusion in certain random lattices,” *Phys. Rev.*, vol. 109, pp. 1492–1505, 1958. — p.16.

[36] A. Lagendijk and B. A. van Tiggelen, “Resonant multiple scattering of light,” *Physics Reports*, vol. 270, pp. 143–215, May 1996. — p.16.

[37] C. W. J. Beenakker, “Random-matrix theory of quantum transport,” *Rev. Mod. Phys.*, vol. 69, pp. 731–808, Jul 1997. — p.19.

[38] J. W. Goodman, *Statistical optics*. 2000. — p.20 and 50.

[39] M. C. W. v. Rossum and T. M. Nieuwenhuizen, “Multiple scattering of classical waves,” *Rev. Mod. Phys.*, vol. 71, pp. 313–371, 1999. — p.20.

[40] M. C. W. van Rossum and T. M. Nieuwenhuizen, “Multiple scattering of classical waves: microscopy, mesoscopy, and diffusion,” *Rev. Mod. Phys.*, vol. 71, pp. 313–371, Jan 1999. — p.20.

[41] T. M. Nieuwenhuizen and M. C. W. Van Rossum, “Intensity distributions of waves transmitted through a multiple scattering medium,” *Phys. Rev. Lett.*, vol. 74, pp. 2674–2677, 1995. — p.20 and 76.

[42] N. Shnerb and M. Kaveh, “Non-rayleigh statistics of waves in random systems,” *Phys. Rev. B*, vol. 43, pp. 1279–1282, Jan 1991. — p.20 and 54.

[43] A. Yamilov and H. Cao, “Effects of localization and amplification on intensity distribution of light transmitted through random media,” *Phys. Rev. E*, vol. 70, p. 037603, Sep 2004. — p.21 and 82.

[44] V. Y. Fedorov and S. E. Skipetrov, “Photon noise in a random laser amplifier with fluctuating properties,” *Phys. Rev. A*, vol. 79, p. 063822, Jun 2009. — p.21.

[45] Y. Kuga and J. Ishimaru, “J. opt. soc. am. a,” pp. 831–835, 1984. — p.22.

[46] M. P. Albada and A. Lagendijk, “Phys. rev. lett.,” pp. 2692–2695, 1985. — p.22.

[47] M. Storzer, P. Gross, C. M. Aegerter, and G. Maret, “Observation of the critical regime near anderson localization of light,” *Physical Review Letters*, vol. 96, no. 6, p. 063904, 2006. — p.22.

[48] E. Akkermans, P. E. Wolf, and R. Maynard, “Coherent backscattering of light by disordered media: Analysis of the peak line shape,” *Phys. Rev. Lett.*, vol. 56, pp. 1471–1474, Apr 1986. — p.22.

[49] M. B. v. d. Mark, M. P. v. Albada, and A. Lagendijk, "Light scattering in strongly scattering media: Multiple scattering and weak localization," *Phys. Rev. B*, vol. 37, pp. 3575–3592, 1988. — p.22.
[50] E. Akkermans and G. Montambaux, *Mesoscopic Physics of Electrons and Photons.* Cambridge University Press, 2007. — p.22.
[51] D. Meschede, *Optics, Light and Lasers.* WILEY-VCH, 2004. — p.24.
[52] R. H. Brown and R. Q. Twiss, "Correlation between photons in two coherent beams of light," *Nature*, vol. 177, pp. 27–29, Jan. 1956. — p.26.
[53] M. Henny, "The fermionic hanbury brown and twiss experiment," *Science*, vol. 284, pp. 296–298, 1999. — p.28.
[54] W. D. Oliver, J. Kim, R. C. Liu, and Y. Yamamoto, "Hanbury brown and twiss-type experiment with electrons," *Science*, vol. 284, pp. 299–301, 1999. — p.28.
[55] R. Landauer *Phil. Mag.*, vol. 21, p. 863, 1970. — p.28.
[56] C. Beenakker and C. Schonenberger, "Quantum shot noise," *Phys. Today*, vol. 56, pp. 37–42, May 2003. — p.28.
[57] M. Büttiker, "Scattering theory of thermal and excess noise in open conductors," *Phys. Rev. Lett.*, vol. 65, pp. 2901–2904, Dec 1990. — p.28.
[58] G. B. Lesovik, "Excess quantum noise in 2d ballistic point contacts," *JETP Lett.*, vol. 49, pp. 592–594, 1989. — p.28.
[59] O. N. Dorokhov, "On the coexistence of localized and extended electronic states in the metallic phase," *Solid State Commun.*, vol. 51, pp. 381–384, 1984. — p.29.
[60] Y. Imry, "Active transmission channels and universal conductance fluctuations," *Europhys. Lett.*, vol. 1, pp. 249–256, 1986. — p.29 and 67.
[61] C. W. J. Beenakker and M. Büttiker, "Suppression of shot noise in metallic diffusive conductors," *Phys. Rev. B*, vol. 46, pp. 1889–1892, Jul 1992. — p.29.
[62] C. W. J. Beenakker and J. A. Melsen, "Conductance fluctuations, weak localization, and shot noise for a ballistic constriction in a disordered wire," *Phys. Rev. B*, vol. 50, pp. 2450–2457, Jul 1994. — p.29.
[63] Y. P. Li, A. Zaslavsky, D. C. Tsui, M. Santos, and M. Shayegan, "Noise characteristics of double-barrier resonant-tunneling structures below 10 khz," *Phys. Rev. B*, vol. 41, pp. 8388–8391, Apr 1990. — p.29.
[64] R. Jalabert, J.-L. Pichard, and C. Beenakker, "Universal quantum signatures of chaos in ballistic transport," *EPL (Europhysics Letters)*, vol. 27, p. 255, 1994. — p.29.
[65] S. Oberholzer, E. V. Sukhorukov, and C. Schonenberger, "Crossover between classical and quantum shot noise in chaotic cavities," *Nature*, vol. 415, pp. 765–767, Feb. 2002. — p.29.
[66] C. W. J. Beenakker, M. Patra, and P. W. Brouwer, "Photonic excess noise and wave localization," *Phys. Rev. A*, vol. 61, p. 051801, Mar 2000. — p.29.
[67] M. Patra and C. W. J. Beenakker, "Excess noise for coherent radiation propagating through amplifying random media," *Phys. Rev. A*, vol. 60, pp. 4059–4066, Nov 1999. — p.30 and 65.
[68] T. C. Ralph, C. C. Harb, and H.-A. Bachor, "Intensity noise of injection-

locked lasers: Quantum theory using a linearized input-output method," *Phys. Rev. A*, vol. 54, pp. 4359–, Nov. 1996. — p.30.

[69] H. A. Bachor and T. C. Ralph, "A guide to experiments in quantum optics," 2004. — p.30.

[70] B. C. Buchler, E. H. Huntington, C. C. Harb, and T. C. Ralph, "Feedback control of laser intensity noise," *Phys. Rev. A*, vol. 57, pp. 1286–, Feb. 1998. — p.30.

[71] J. Belfi, I. Galli, G. Giusfredi, and F. Marin, "Intensity noise of an injection-locked ti:sapphire laser: analysis of the phase-noise-to-amplitude-noise conversion," *J. Opt. Soc. Am. B*, vol. 23, pp. 1276–1286, July 2006. — p.30.

[72] M. Kindermann, Y. V. Nazarov, and C. W. J. Beenakker, "Manipulation of photon statistics of highly degenerate incoherent radiation," *Phys. Rev. Lett.*, vol. 88, p. 063601, Jan 2002. — p.32 and 65.

[73] C. Thompson, G. Vemuri, and G. S. Agarwal, "Anderson localization with second quantized fields in a coupled array of waveguides," *Phys. Rev. A*, vol. 82, pp. 053805–, Nov. 2010. — p.32.

[74] S. E. Skipetrov, "Quantum theory of dynamic multiple light scattering in fluctuating disordered media," *Physical Review A*, vol. 75, no. 5, p. 053808, 2007. — p.32.

[75] M. Patra and C. W. J. Beenakker, "Propagation of squeezed radiation through amplifying or absorbing random media," *Phys. Rev. A*, vol. 61, p. 063805, May 2000. — p.32 and 65.

[76] S. Balog, P. Zakharov, F. Scheffold, and S. Skipetrov, "Photocount statistics in mesoscopic optics," *Physical Review Letters*, vol. 97, no. 10, pp. –, 2006. — p.32.

[77] S. Smolka, A. Huck, U. L. Andersen, A. Lagendijk, and P. Lodahl, "Observation of spatial quantum correlations induced by multiple scattering of nonclassical light," *Phys. Rev. Lett.*, vol. 102, pp. 193901–, May 2009. — p.32.

[78] P. Lodahl and A. Lagendijk, "Transport of quantum noise through random media," *Physical Review Letters*, vol. 94, no. 15, p. 153905, 2005. — p.33 and 49.

[79] P. Lodahl, A. P. Mosk, and A. Lagendijk, "Spatial quantum correlations in multiple scattered light," *Physical Review Letters*, vol. 95, no. 17, p. 173901, 2005. — p.33 and 34.

[80] P. A. Mello, "Macroscopic approach to universal conductance fluctuations in disordered metals," *Phys. Rev. Lett.*, vol. 60, pp. 1089–1092, Mar 1988. — p.37.

[81] J. F. de Boer, *Optical fluctuations on the transmission and reflection of mesoscopic systems.* PhD thesis, 1995. — p.37 and 69.

[82] J. X. Zhu, D. J. Pine, and D. A. Weitz, "Internal reflection of diffusive light in random media," *Phys. Rev. A*, vol. 44, pp. 3948–3959, September 1991. — p.39.

[83] R. H. J. Kop, *Time-resolved interferometry on metals and disordered systems.* PhD thesis, 1998. — p.40.

[84] I. M. Vellekoop, “Time resolved measurements on diffusion of light,” Master’s thesis, 2001. — p.42.

[85] H. van de Hulst, *Multiple light scattering, Volume 1.* Academic Press, 1980. — p.42.

[86] A. F. Koenderink, M. Megens, G. van Soest, W. L. Vos, and A. Lagendijk, “Enhanced backscattering from photonic crystals,” *Phys. Lett. A*, vol. 268, p. 104, 2000. — p.50.

[87] Y. L. Kim, Y. Liu, V. M. Turzhitsky, H. K. Roy, R. K. Wali, and V. Backman, “Coherent backscattering spectroscopy,” *Opt. Lett.*, vol. 29, no. 16, pp. 1906–1908, 2004. — p.50.

[88] O. L. Muskens and A. Lagendijk, “Broadband enhanced backscattering spectroscopy of strongly scattering media,” *Opt. Express*, vol. 16, no. 2, pp. 1222–1231, 2008. — p.50.

[89] P. W. Anderson, “Absence of diffusion in certain random lattices,” *Phys. Rev.*, vol. 109, pp. 1492–1505, Mar 1958. — p.50.

[90] A. L. D.S. Wiersma, P. Bartolini and R. Righini, “Localization of light in a disordered medium,” *Nature*, vol. 390, pp. 671–673, 1997. — p.50.

[91] F. Scheffold, R. Lenke, R. Tweer, and G. Maret, “Localization or classical diffusion of light?,” *Nature*, vol. 398, pp. 206–207, Mar. 1999. — p.50.

[92] J. R. Ott, N. A. Mortensen, and P. Lodahl, “Quantum interference and entanglement induced by multiple scattering of light,” *Phys. Rev. Lett.*, vol. 105, p. 090501, Aug 2010. — p.50.

[93] L. Mandel and E. Wolf, *Optical Coherence and Quantum Optics.* Cambridge: Cambridge University Press, 1995. — p.50 and 51.

[94] B. Huttner and Y. Ben-Aryeh, “Influence of a beam splitter on photon statistics,” *Phys. Rev. A*, vol. 38, pp. 204–211, Jul 1988. — p.54 and 55.

[95] S. S. E. Van Tiggelen, Bart A., *Wave scattering in complex media: from theory to applications.* Springer, 2003. — p.56.

[96] L. E. Estes, L. M. Narducci, and R. A. Tuft, “Scattering of light from a rotating ground glass,” *J. Opt. Soc. Am.*, vol. 61, no. 10, pp. 1301–1306, 1971. — p.56.

[97] M. P. V. Albada and A. Lagendijk, “Observation of weak localization of light in a random medium,” *Phys. Rev. Lett.*, vol. 55, pp. 2692–2695, Dec 1985. — p.58.

[98] F. T. Arecchi, “Measurement of the statistical distribution of gaussian and laser sources,” *Phys. Rev. Lett.*, vol. 15, pp. 912–916, Dec 1965. — p.59.

[99] W. Martienssen and E. Spiller, “Coherence and fluctuations in light beams,” *American Journal of Physics*, vol. 32, no. 12, pp. 919–926, 1964. — p.59.

[100] F. Schuurmans, D. Vanmaekelbergh, J. Van De Lagemaat, and A. Lagendijk, “Strongly photonic macroporous gallium phosphide networks,” *Science*, vol. 284, no. 5411, pp. 141–143, 1999. — p.59.

[101] D. S. Wiersma, *Light in strongly scattering and amplifying random media.* PhD thesis, 1995. — p.62.

[102] P. A. Mello, E. Akkermans, and B. Shapiro, “Macroscopic approach to correlations in the electronic transmission and reflection from disordered conduc-

tors," *Phys. Rev. Lett.*, vol. 61, pp. 459–462, Jul 1988. — p.62.

[103] M. Büttiker, Y. Imry, R. Landauer, and S. Pinhas, "Generalized many-channel conductance formula with application to small rings," *Phys. Rev. B*, vol. 31, pp. 6207–6215, May 1985. — p.67.

[104] P. A. Lee and A. D. Stone, "Universal conductance fluctuations in metals," *Phys. Rev. Lett.*, vol. 55, pp. 1622–1625, Oct 1985. — p.67.

[105] S. Feng, C. Kane, P. Lee, and A. Stone, "Correlations and fluctuations of coherent wave transmission through disordered media," *Physical Review Letters*, vol. 61, no. 7, pp. 834–837, 1988. — p.68.

[106] R. Berkovits and S. Feng, "Correlations in coherent multiple scattering," *Physics Reports*, vol. 238, no. 3, pp. 135 – 172, 1994. — p.68 and 69.

[107] H. Hu, A. Strybulevych, J. Page, S. Skipetrov, and B. Van Tiggelen, "Localization of ultrasound in a three-dimensional elastic network," *Nature Physics*, vol. 4, no. 12, pp. 945–948, 2008. — p.68.

[108] A. A. Chabanov, M. Stoytchev, and A. Z. Genack, "Statistical signatures of photon localization," *Nature*, vol. 404, pp. 850–853, Apr. 2000. — p.68.

[109] M. Stoytchev and A. Z. Genack, "Observations of non-rayleigh statistics in the approach to photon localization," *Opt. Lett.*, vol. 24, no. 4, pp. 262–264, 1999. — p.68.

[110] M. Stoytchev and A. Z. Genack, "Measurement of the probability distribution of total transmission in random waveguides," *Phys. Rev. Lett.*, vol. 79, pp. 309–312, Jul 1997. — p.68.

[111] A. Z. Genack, N. Garcia, and W. Polkosnik, "Long-range intensity correlation in random media," *Phys. Rev. Lett.*, vol. 65, pp. 2129–2132, Oct 1990. — p.68.

[112] N. Garcia and A. Z. Genack, "Crossover to strong intensity correlation for microwave radiation in random media," *Phys. Rev. Lett.*, vol. 63, pp. 1678–1681, Oct 1989. — p.68.

[113] A. Z. Genack and N. Garcia, "Intensity statistics and correlation in absorbing random media," 1993. — p.69.

[114] O. L. Muskens and A. Lagendijk, "Method for broadband spectroscopy of light transport through opaque scattering media," *Opt. Lett.*, vol. 34, pp. 395–397, Feb. 2009. — p.69.

[115] J. F. d. Boer, M. P. v. Albada, and A. Lagendijk, "Transmission and intensity correlations in wave-propagation through random-media," *Phys. Rev. B*, vol. 45, pp. 658–666, 1992. — p.69.

[116] J. F. d. Boer, M. C. W. van, Rossum, M. P. van, Albada, T. M. Nieuwenhuizen, and A. Lagendijk, "Probability distribution of multiple scattered light measured in total transmission," *Phys. Rev. Lett.*, vol. 73, pp. 2567–2570, 1994. — p.69.

[117] F. Scheffold, W. Härtl, G. Maret, and E. Matijević, "Observation of long-range correlations in temporal intensity fluctuations of light," *Phys. Rev. B*, vol. 56, pp. 10942–10952, Nov 1997. — p.69.

[118] F. Scheffold and G. Maret, "Universal conductance fluctuations of light," *Phys. Rev. Lett.*, vol. 81, pp. 5800–5803, Dec 1998. — p.69.

[119] S. Feng, C. Kane, P. A. Lee, and A. D. Stone, "Correlations and fluctuations

of coherent wave transmission through disordered media," *Phys. Rev. Lett.*, vol. 61, pp. 834–837, 1988. — p.69.

[120] O. L. Muskens, S. L. Diedenhofen, M. H. M. van Weert, M. T. Borgstrm, E. P. A. M. Bakkers, and J. G. Rivas, "Epitaxial growth of aligned semiconductor nanowire metamaterials for photonic applications," *Adv. Funct. Mater.*, vol. 18, no. 7, pp. 1039–1046, 2008. — p.69.

[121] O. L. Muskens, S. L. Diedenhofen, B. C. Kaas, R. E. Algra, E. P. A. M. Bakkers, J. Gomez Rivas, and A. Lagendijk, "Large photonic strength of highly tunable resonant nanowire materials," *Nano Letters*, vol. 9, no. 3, pp. 930–934, 2009. — p.69.